

TUNNEL STABILITY ANALYSIS AND GEOLOGICAL MAPPING USING LIDAR AND RGB
SENSOR TECHNOLOGIES IN THE KRISTINEBERG UNDERGROUND MINE

A thesis submitted to the Delft University of Technology in partial fulfillment
of the requirements for the degree of

Master of Science in the European Mining Course

by

Fabian Roderick Kamp

May 6, 2022

ABSTRACT

Measuring and analyzing the tunnel deformation through convergence measurements and cross-correlation with geological mapping is essential for understanding and controlling tunnel stability, worker safety and predicting failure zones. In order to achieve this, a new device, the so-called GroundProbe GML is tested and analyzed in this study. Currently, the deformation in the Kristineberg mine is measured through conventional techniques, such as the tape extensometer, that are labor intensive and time-consuming. On top of that, the geological mapping is done by visual inspection by experienced geologists. There is no system in place that correlates the geological setting to the deformation of the tunnels. This research aims to explore the possibility to quantify tunnel wall convergence and correlate the movement to geological circumstances.

An accuracy analysis is performed, to identify the accuracy of the Light Detection and Ranging (LiDAR) technology in comparison to conventional techniques. This analysis is conducted in both a controlled (above-ground) and an uncontrolled (underground) environment and focuses on the use of different targets, i.e. prisms or reflectors, and the difference between continuous and periodic measurements. The fresh rock surfaces are also mapped by means of geological LiDAR data as well as Red-Green-Blue (RGB) image analysis and this is correlated with tunnel wall convergence. This is done to increase the understanding of the impact of the geological setting on the tunnel wall convergence.

The accuracy presented by GroundProbe of ± 3 mm for periodic measurements is difficult to achieve in an underground environment with mining activity. Especially the deformation of measurement points that are at a more oblique angle to the scanner prove to be difficult to assess. The geological LiDAR data can be used to distinguish different rock types and geological features with limited subjectivity. The transition zones from one rock type to the other become clearly visible from the geological LiDAR data. Additionally, geological features such as joints can be identified when combining LiDAR data with RGB image analysis. The primary promotor of tunnel wall convergence is the hanging wall that pushes down on the foot wall in combination with non-uniform waste rock areas, that are for example split into two sections by a joint.

In a tunneling environment where mining activities are conducted, such as the application of shotcrete, scaling, blasting and leveling of the floor, periodic measurements with a LiDAR set-up on a tripod are difficult. One of the main limitations is the absence of stable reference points that the LiDAR scanner uses to determine its XYZ-position. The oblique angle can also be a limiting factor, measurement points closer to the LiDAR scanner provide more reliable results. For continuous measurements however, this proves to be less relevant because the repositioning error can be omitted. The LiDAR scanning technology has the potential to be used as geological mapping tool based on the varying reflectivities of different rock types. By combining LiDAR technology with RGB image analysis, a more thorough understanding of the geological setting can be obtained. By relating this understanding to the quantification of the tunnel wall convergence, this technique can be used to correlate the geology to the movement of the rock mass.

ACKNOWLEDGEMENTS

I would like to thank Boliden for giving me the opportunity to work on this project at their Kristineberg mine in the North of Sweden. The three months I spent in Northern Sweden and the period afterwards have been a very valuable experience, in which I learnt a lot. My special gratitude goes out towards Alexander Bondarchuk and Dan-Ulf Näslund from Boliden, thank you for all the guidance throughout the project and the pleasant collaboration. I have learned a great deal about the mining industry and about the geotechnical aspects that come with underground mining, thank you for sharing your valuable experience and knowledge with me. Working with you in and after Sweden was a great and unforgettable experience. Thanks to everybody else at Boliden Kristineberg who shared their knowledge with me and provided their assistance during the completion of the research. I am very grateful for all the Kristineberg employees that accompanied me every hour of the day, if needed. I would also like to thank Feven Desta and Mike Buxton from Delft University of Technology for their guidance, patience and their feedback. Lastly, I would like to thank all of my friends of the large cauldron-like hollow that forms shortly after the emptying of a magma chamber in a volcanic eruption for remaining dormant during my thesis and of course my family for their support during this final stage of my master's degree.

Fabian Kamp

Den Haag, May 2022

CONTENTS

1	INTRODUCTION	1
1.1	Research Objectives	1
1.2	Research hypothesis	2
1.3	Research questions	2
1.4	Scope of this study	2
1.5	Thesis structure	2
2	LITERATURE REVIEW	3
2.1	Tunnel wall convergence studies	3
2.2	Convergence measurement techniques	4
2.2.1	Conventional Techniques	4
2.2.2	Latest Techniques	6
2.3	Application of LiDAR for Geological Mapping in Underground Mines	8
2.4	Application of LiDAR for displacement measurements	10
2.5	Application of RGB imaging for geological interpretations	11
2.6	Key outcomes	11
3	STUDY AREA AND INSTRUMENTATION	13
3.1	Geology	13
3.1.1	Regional Geology	13
3.1.2	Local Geology	15
3.1.3	Lithologies	16
3.1.4	Orebodies	17
3.1.5	Structural Geology	18
3.2	Mine background	19
3.3	Geotechnical conditions	20
4	SENSOR DATA ACQUISITION AND DATA PROCESSING	21
4.1	Sensor technologies	21
4.1.1	Instrumentation	22
4.2	Data Gathering Methods	22
4.2.1	LiDAR data gathering	22
4.2.2	RGB imaging	22
4.2.3	LiDAR Scan Settings	22
5	METHODOLOGY	25
5.1	Data Acquisition	25
5.1.1	Room L62-Höger	26
5.1.2	Room KK2	27
5.1.3	Room KK3	32
5.2	Data pre-processing	33
5.3	Data processing workflow	33
5.4	Data modeling techniques	34
5.5	Validation	37
5.5.1	Model validation	38
6	RESULTS	41
6.1	LiDAR Accuracy measurements	41
6.2	LiDAR versus conventional deformation measurements	45
6.2.1	Room L62-Höger	45
6.2.2	Room KK2	61
6.2.3	Room KK3	65
6.3	Continuous measurements: KK2	69
6.4	The influence of the geology on the deformation	71
6.4.1	Blast-Induced Deformation	74
6.4.2	Long-Term Deformation	76
6.4.3	LiDAR Geology Scans	79
6.4.4	RGB geology data	83
6.4.5	Strong deformation zones	84
7	DISCUSSION	89
7.1	Limitations	89
7.2	Significance of the results	89
7.3	Geological analysis	90

8	CONCLUSION AND RECOMMENDATIONS	91
8.1	Conclusion	91
8.1.1	Research Questions	91
8.2	Recommendations	92
A	RAW LIDAR DEFORMATION RESULTS	96
B	KK2 LONG-TERM DEFORMATION	97
C	RGB GEOLOGY IMAGES CLASSIFIED	103
D	LIDAR GEOLOGY SCANS	106

LIST OF FIGURES

Figure 1.1	The GroundProbe GML (Geotechnical Monitoring LiDAR) device (from GroundProbe [2021b]).	1
Figure 2.1	Tunnel wall convergence development over time.	3
Figure 2.2	Digital Tape extensometer (retrieved from: SoilInstruments [2021]).	4
Figure 2.3	Illustration of the total station measurement techniques and the results. a) shows the control points that are measured. b) shows the deformation results over a total of 75 days. c) shows the tunnel convergence over time. (modified from: Walton et al. [2014])	5
Figure 2.4	Typical Total Station measurement set-up (Cabrejo et al. [2017]).	5
Figure 2.5	Occlusion effect (Höfle et al. [2013])	7
Figure 2.6	Pulse Select (Boliden [2020]).	7
Figure 2.7	Lithological classification of airborne Lidar data, modified from Grebby et al. [2010]	9
Figure 2.8	Different scan locations used in U-shaped tunnels (Chen et al. [2018]).	10
Figure 3.1	Location of the Kristineberg Mine (modified from Google Maps)	13
Figure 3.2	Regional deposits in the Skellefte District (modified from: Schwarz et al. [2020])	14
Figure 3.3	Geology of the Skellefte District (modified from: Boliden [2019]).	14
Figure 3.4	Schematic sketch of the tectonic evolution of the Kristineberg area (not to scale). A) Illustration of the syn-extensional volcanism and mineralization sedimentation that occurred at 1.89 Ga. B) Illustration of subsequent crustal shortening leading to basin inversion and the transpositioning of mineralizations. (Weihed et al. [2011]).	15
Figure 3.5	Local geological setting (Arebäck et al. [2005]).	16
Figure 3.6	Illustration of the L-zone orebody. Chlorite schist is shown in green and massive sulphides in red (modified from: Boliden [2019]).	17
Figure 3.7	Illustration of the Kopparklumpen (KK) orebody. Cu-rich zones in green and Zn-rich zones in brown (modified from: Boliden [2019]).	18
Figure 3.8	Mine system layout along with the respective locations of the two orebodies of interest (modified from Boliden [2020]).	19
Figure 3.9	Figure illustrating the geological setting in the face of KK2 on the 28th of April.	20
Figure 4.1	Illustration of the Pulse Select parameter (from GroundProbe [2021b]).	23
Figure 5.1	Progression of scan and prism locations.	25
Figure 5.2	Illustration of how the LiDAR scans from the exposed rock surfaces were taken. (Lato and Diederichs [2014]).	26
Figure 5.3	Location of the measurements in room L62-HÖGER.	26
Figure 5.4	Location of the measurements in room KK2 (initial).	27
Figure 5.5	Location of the measurements in room KK2 (final).	28
Figure 5.6	Overview of the locations of the exposed rock surface scans taken in the left side of KK2.	28
Figure 5.7	Overview of the locations of the exposed rock surface scans taken in the right side of KK2.	29
Figure 5.8	LiDAR intensity data obtained from the fresh rock surface in KK2 on the 28th of April.	29
Figure 5.9	Figure illustrating the geological setting in the face of KK2 on the 28th of April.	30
Figure 5.10	Set-up of the continuous measurement experiment.	30
Figure 5.11	Sketch of the set-up of the continuous measurement experiment.	31
Figure 5.12	An RGB image of the face scanned during the continuous measurements.	31
Figure 5.13	KK3 layout LiDAR greyscale images.	32
Figure 5.14	The initial layout of KK3.	32
Figure 5.15	Sketch of general workflow.	33
Figure 5.16	Elbow plot of geological LiDAR data 28/04/2021.	34
Figure 5.17	RGB image captured from the exposed rock surface on the 28th of April in KK2.	35
Figure 5.18	Training the SVM classifier on the RGB image captured from the exposed rock surface on the 28th of April in KK2.	36
Figure 5.19	SVM Classification based on the RGB image captured from the exposed rock surface on the 28th of April in KK2.	36
Figure 5.20	Accuracy measurements set-up	37
Figure 5.21	Deformation data visualized in SSR-viewer	37
Figure 5.22	Snapshot of the scan correction window that shows the original deformation and a preview of the applied correction (in this case no correction so they are both the same). LW = Left wall, RW = Right wall.	38

Figure 5.23	Illustration of auto alignment of subsequent scans.	39
Figure 6.1	Accuracy measurement I absolute deformation results of the box with respect to the Leica Disto D2.	41
Figure 6.2	Accuracy measurement I percentual deformation results of the box with respect to the Leica Disto D2.	42
Figure 6.3	Accuracy measurement I absolute deformation results of the wall with respect to the Leica Disto D2.	42
Figure 6.4	Accuracy measurement II (uncorrected) absolute deformation results of the box with respect to the Leica Disto D2.	43
Figure 6.5	Accuracy measurement II: prisms corrected vs. uncorrected absolute deformation results of the box with respect to the Leica Disto D2.	43
Figure 6.6	Accuracy measurement II: reflectors corrected vs. uncorrected absolute deformation results of the box with respect to the Leica Disto D2.	44
Figure 6.7	Accuracy measurement II: prisms (corrected) vs. reflectors (corrected) absolute deformation results of the box with respect to the Leica Disto D2.	44
Figure 6.8	L62H-1 survey point 4 total deformation results comparison between the survey data results vs. the LiDAR scans with the use of different targets (uncorrected).	45
Figure 6.9	L62H-1 survey point 4 total deformation results comparison between the survey data results vs. the LiDAR scans with the use of different targets (corrected).	46
Figure 6.10	L62H-1 survey point 4 daily average deformation results comparison between the survey data results vs. the LiDAR scans with the use of different targets (uncorrected).	46
Figure 6.11	L62H-1 survey point 4 daily average deformation results comparison between the survey data results vs. the LiDAR scans with the use of different targets (corrected).	47
Figure 6.12	L62H-1 survey point 5 total deformation results comparison between the survey data results vs. the LiDAR scans with the use of different targets (uncorrected).	47
Figure 6.13	L62H-1 survey point 5 total deformation results comparison between the survey data results vs. the LiDAR scans with the use of different targets (corrected).	48
Figure 6.14	L62H-1 survey point 5 daily average deformation results comparison between the survey data results vs. the LiDAR scans with the use of different targets (uncorrected).	48
Figure 6.15	L62H-1 survey point 5 daily average results comparison between the survey data results vs. the LiDAR scans with the use of different targets (corrected).	49
Figure 6.16	L62H-1 survey point 6 total deformation results comparison between the survey data results vs. the LiDAR scans with the use of different targets (uncorrected).	49
Figure 6.17	L62H-1 survey point 6 total deformation results comparison between the survey data results vs. the LiDAR scans with the use of different targets (corrected).	50
Figure 6.18	L62H-1 survey point 6 daily average deformation results comparison between the survey data results vs. the LiDAR scans with the use of different targets (uncorrected).	50
Figure 6.19	L62H-1 survey point 6 daily average deformation results comparison between the survey data results vs. the LiDAR scans with the use of different targets (corrected).	51
Figure 6.20	L62H-2 survey point 5 total deformation results comparison between the survey data results vs. the LiDAR scans with the use of different targets (uncorrected).	51
Figure 6.21	L62H-2 survey point 5 total deformation results comparison between the survey data results vs. the scans with the use of different targets (corrected).	52
Figure 6.22	L62H-2 survey point 5 daily average deformation results comparison between the survey data results vs. the LiDAR scans with the use of different targets (uncorrected).	52
Figure 6.23	L62H-2 survey point 5 daily average deformation results comparison between the survey data results vs. the LiDAR scans with the use of different targets (corrected).	53
Figure 6.24	L62H-2 survey point 6 total deformation results comparison between the survey data results vs. the scans with the use of different targets (uncorrected).	53
Figure 6.25	Shotcrete damage as result of tunnel wall convergence.	54
Figure 6.26	L62H-2 survey point 6 total deformation results comparison between the survey data results vs. the scans with the use of different targets (corrected).	54
Figure 6.27	L62H-2 survey point 6 daily average deformation results comparison between the survey data results vs. the LiDAR scans with the use of different targets (uncorrected).	54
Figure 6.28	L62H-2 survey point 6 daily average deformation results comparison between the survey data results vs. the LiDAR scans with the use of different targets (corrected).	55
Figure 6.29	L62H-3 survey point 4 total deformation results comparison between the survey data results vs. the scans with the use of different targets (uncorrected).	55
Figure 6.30	L62H-3 survey point 4 total deformation results comparison between the survey data results vs. the scans with the use of different targets (corrected).	56
Figure 6.31	L62H-3 survey point 4 daily average deformation results comparison between the survey data results vs. the LiDAR scans with the use of different targets (uncorrected).	56

Figure 6.32	L62H-3 survey point 4 daily average deformation results comparison between the survey data results vs. the LiDAR scans with the use of different targets (corrected).	57
Figure 6.33	L62H-3 survey point 5 total deformation results comparison between the survey data results vs. the scans with the use of different targets (uncorrected).	57
Figure 6.34	L62H-3 survey point 5 total deformation results comparison between the survey data results vs. the scans with the use of different targets (corrected).	58
Figure 6.35	L62H-3 survey point 5 daily average deformation results comparison between the survey data results vs. the LiDAR scans with the use of different targets (uncorrected).	58
Figure 6.36	L62H-3 survey point 5 daily average deformation results comparison between the survey data results vs. the LiDAR scans with the use of different targets (corrected).	59
Figure 6.37	L62H-3 survey point 6 total deformation results comparison between the survey data results vs. the scans with the use of different targets (uncorrected).	59
Figure 6.38	L62H-3 survey point 6 total deformation results comparison between the survey data results vs. the scans with the use of different targets (corrected).	60
Figure 6.39	L62H-3 survey point 6 daily average deformation results comparison between the survey data results vs. the LiDAR scans with the use of different targets (uncorrected).	60
Figure 6.40	L62H-3 survey point 6 daily average deformation results comparison between the survey data results vs. the LiDAR scans with the use of different targets (corrected).	61
Figure 6.41	Illustration of the layout of the periodic measurements in KK2 on location 2. MP = measurement point, SP = survey point, LW = left wall, RW = right wall.	61
Figure 6.42	Comparison of LiDAR total deformation results vs tape extensometer results at KK2 location 2, measurement point 0.	62
Figure 6.43	Comparison of LiDAR daily average deformation vs tape extensometer results at KK2 location 2, measurement point 0.	63
Figure 6.44	Comparison of LiDAR total deformation results vs tape extensometer results at KK2 location 2, measurement point 1.	63
Figure 6.45	Comparison of LiDAR daily average deformation vs tape extensometer results at KK2 location 2, measurement point 1.	64
Figure 6.46	Comparison of LiDAR total deformation results vs tape extensometer results at KK2 location 2, measurement point 2.	64
Figure 6.47	Comparison of LiDAR daily average deformation vs tape extensometer results at KK2 location 2, measurement point 2.	65
Figure 6.48	Comparison of LiDAR total deformation results vs tape extensometer results at KK3 location 1, measurement point 1.	65
Figure 6.49	Comparison of LiDAR daily average deformation vs tape extensometer results at KK3 location 1, measurement point 1.	66
Figure 6.50	Comparison of LiDAR total deformation results vs tape extensometer results at KK3 location 1, measurement point 2.	66
Figure 6.51	Comparison of LiDAR daily average deformation vs tape extensometer results at KK3 location 1, measurement point 2.	67
Figure 6.52	Figure illustrating LiDAR deformation data in room KK3 before and after shotcrete application.	67
Figure 6.53	Figure illustrating shotcrete application with LiDAR data. a) RGB Image of the damage in the wall. b) LiDAR data of the damage in the wall. c) LiDAR data of the damage after shotcrete application.	68
Figure 6.54	Figure illustrating the LiDAR deformation data in the direction of the face during the continuous measurements (with prisms). Brown delineation shows where the shotcrete starts and the area covered within the black circle shows the greatest deformation.	69
Figure 6.55	Figure illustrating the LiDAR deformation data in the direction of the face during the continuous measurements (without prisms). Brown delineation shows where the shotcrete starts and the area covered within the black circle shows the greatest deformation.	69
Figure 6.56	LiDAR deformation scan result from continuous measurements in KK2 (positive and negative).	70
Figure 6.57	LiDAR deformation scan result from continuous measurements in KK2 (positive).	70
Figure 6.58	LiDAR deformation scan result from continuous measurements in KK2 versus tape extensometer measurement results.	71
Figure 6.59	The image classification result after applying a SVM deep learning algorithm to the RGB image of the face scanned during the continuous measurements.	71
Figure 6.60	Image showing the LiDAR data based on varying intensity levels in the face scanned during the continuous measurements.	72

Figure 6.61	The LiDAR scan result of the fresh rock at the face during the continuous measurements.	72
Figure 6.62	Analysis of the structural geology seen in the LiDAR scan result of the fresh rock at the face during the continuous measurements.	73
Figure 6.63	a) Left wall bottom left, b) Left wall bottom right c) Left wall top.	73
Figure 6.64	Analysis of the structural geology seen in the LiDAR scan result of the fresh rock at the face during the continuous measurements.	73
Figure 6.65	Blast-induced deformation in room KK2 from 23/04 until 30/04 including geology scans.	74
Figure 6.66	Blast-induced deformation in room KK2 from 30/04 until 04/05 including geology scans.	75
Figure 6.67	Blast-induced deformation in room KK2 from 04/05 until 11/05 including geology scans.	75
Figure 6.68	Blast-induced deformation in room KK2 from 11/05 until 18/05 including all geology scans.	76
Figure 6.69	Illustration of the geological setting in the face of KK2 on the 28th of April.	76
Figure 6.70	CloudCompare visualization of the LiDAR deformation data between 11/05 and 18/05 with geological LiDAR scans coloured in greyscale based on intensity levels.	77
Figure 6.71	LiDAR deformation data with greyscale geological LiDAR scans. Red circle to indicate strong deformation.	77
Figure 6.72	Long-term deformation in room KK2 from 30/04 until 18/05 including geology scans. a) Deformation from 30/04 until 04/05. b) Deformation from 30/04 until 11/05. c) Deformation from 30/04 until 18/05.	78
Figure 6.73	Long-term deformation in room KK2 from 01/06 until 18/06 including geology scans. a) Deformation from 01/06 until 05/06. b) Deformation from 01/06 until 16/06. c) Deformation from 01/06 until 18/06.	79
Figure 6.74	3D Intensity and density visualization using LiDAR geology scan 28/04/2021 [1/3].	80
Figure 6.75	3D intensity clustered data of LiDAR geology scan 28/04/2021 [2/3].	81
Figure 6.76	Intensity ranges per cluster for both clustering methods of LiDAR geology scan 28/04/2021 [3/3].	81
Figure 6.77	Result of k-means clustering with scaled intensity per cluster of LiDAR geology scan 28/04/2021.	82
Figure 6.78	Result of two-phased clustering with scaled intensity per cluster of LiDAR geology scan 28/04/2021.	82
Figure 6.79	Classified RGB image of the exposed rock surface on 28/04/2021.	83
Figure 6.80	Comparison of RGB image analysis to the LiDAR data of the exposed rock surface on 28/04/2021.	83
Figure 6.81	LiDAR blast-induced deformation data with red circle indicating strong deformation zone.	84
Figure 6.82	RGB images of exposed rock surfaces on set dates (edited to show geological setting).	84
Figure 6.83	Classified RGB images of exposed rock surfaces on set dates.	85
Figure 6.84	Geological LiDAR data of exposed rock surfaces on 22/04/2021 and 28/04/2021.	86
Figure 6.85	Geological LiDAR data of exposed rock surfaces on 04/05/2021 and 05/05/2021.	86
Figure B.1	KK2-1 long-term deformation from 23/04 until 18/05.	98
Figure B.2	KK2-1 long-term deformation from 04/05 until 18/05.	99
Figure B.3	KK2-2 long-term deformation from 22/04 until 11/05.	100
Figure B.4	KK2-2 long-term deformation from 22/04 until 05/06.	101
Figure B.5	KK2-2 long-term deformation from 22/04 until 18/06.	102
Figure C.1	RGB image geological classification 22/04/2021.	103
Figure C.2	RGB image geological classification 28/04/2021.	103
Figure C.3	RGB image geological classification 05/05/2021.	103
Figure C.4	RGB image geological classification 11/05/2021.	104
Figure C.5	RGB image geological classification 13/05/2021.	104
Figure C.6	RGB image geological classification 22/05/2021.	104
Figure C.7	RGB image geological classification 26/05/2021.	104
Figure C.8	RGB image geological classification 29/05/2021.	105
Figure C.9	RGB image geological classification 04/06/2021.	105
Figure D.1	LiDAR geology scan analysis 22/04/2021 [4/4].	107
Figure D.2	LiDAR geology scan analysis 28/04/2021 [4/4].	107
Figure D.3	LiDAR geology scan analysis 04/05/2021 [4/4].	108
Figure D.4	LiDAR geology scan analysis 05/05/2021 [4/4].	108
Figure D.5	LiDAR geology scan analysis 11/05/2021 [4/4].	109
Figure D.6	LiDAR geology scan analysis 13/05/2021 [4/4].	109

Figure D.7	LiDAR geology scan analysis 22/05/2021 [4/4].	110
Figure D.8	LiDAR geology scan analysis 26/05/2021 [4/4].	110
Figure D.9	LiDAR geology scan analysis 29/05/2021 [4/4].	111
Figure D.10	LiDAR geology scan analysis 01/06/2021 [4/4].	111
Figure D.11	LiDAR geology scan analysis 04/06/2021 [4/4].	112

LIST OF TABLES

Table 3.1	Production and corresponding grades at the Kristineberg Mine in 2020 (Boliden [2020]).	19
Table 4.1	GML scanner parameters.	22
Table 5.1	Size of the acquired dataset.	25
Table A.1	Accuracy Measurement I: prisms results of the absolute deformation of the box vs. the Leica Disto D2.	96
Table A.2	Accuracy Measurement I: prisms results of the absolute deformation of the box vs. the Leica Disto D2.	96
Table A.3	KK2 Measurement Point 0 (MP0) deformation results.	96
Table A.4	KK2 Measurement Point 1 (MP1) deformation results.	96
Table A.5	KK2 Measurement Point 2 (MP2) deformation results.	96

ACRONYMS

GML Geotechnical Monitoring LiDAR	1
KDE Kernel Density Estimate	35
KK₂ Kopparklumpen 2	28
KK₃ Kopparklumpen 3	32
LiDAR Light Detection and Ranging	iii
LDP Longitudinal Displacement Profile	3
MP₁ Measurement Point I	71
MP₃ Measurement Point III	71
PCD Point Cloud Data	8
RGB Red-Green-Blue	iii
SP₁ Survey Point I	61
SSR Slope Stability Radar	22
SVM Support Vector Machine	11
TOF LiDAR time-of-flight LiDAR	6
UAV Unmanned Aerial Vehicles	9
VHMS Volcanogenic Hosted Massive Sulphide	13
WCSS With-in Cluster Sum of Squares	34

1

INTRODUCTION

One of the biggest challenges involved in underground mining consists of stability analysis of the tunnel environment. As a result of increasing technological innovations, the extraction of minerals under more complex geological circumstances has become increasingly interesting. The orebodies that were out of reach several years ago, can have potential to be extracted safely nowadays. The stability of the underground environment is of paramount importance to ensure a safe and secure extraction of minerals. The development of the [LiDAR](#) scanner technology has great potential to realize this.

3D [LiDAR](#) scanning is a remote sensing method that uses light in the form of a pulsed laser to measure ranges and the intensity of the reflection. A laser beam is emitted towards an object and the then returning beam is collected by sensors within the [LiDAR](#) scanner. Differences in i.e. return times and wavelength provide information about the object of interest and provide the means for creating a 3D digital representation of the object.



Figure 1.1: The GroundProbe GML (Geotechnical Monitoring LiDAR) device (from [GroundProbe \[2021b\]](#)).

The [LiDAR](#) technology can map features of an object or environment as a point cloud that appear as solid physical objects on first sight ([Fekete and Diederichs \[2013\]](#) and [GroundProbe \[2021b\]](#)). The scanner that is used in this study is called the GroundProbe Geotechnical Monitoring LiDAR ([GML](#)) scanner, which is illustrated in [Figure 1.1](#).

1.1 RESEARCH OBJECTIVES

By combining [LiDAR](#) tunnel deformation measurements with geological mapping based on both [LiDAR](#) and [RGB](#) data, a more thorough understanding of the deformation of the tunnel can be achieved. As the Boliden Kristineberg mine progresses towards more and more automation in order to enhance productivity, ensure the safety of the workers and increase the stability of the tunnel, the use of [LiDAR](#) equipment is analyzed in this research. The use of [LiDAR](#) equipment in the underground mining environment has increased significantly over the last 10 years. [LiDAR](#) sensors have great potential to analyze the convergence of tunnels, both periodically as well as constantly. While conducting the measurements, the [LiDAR](#) sensors are able to transmit live-data to the surface, where it can be processed and analyzed in real-time. By applying such sensor technology in the underground environment, the safety of the workers can be secured, productivity can be increased and the stability of the tunnel can be more thoroughly understood according to [Fekete et al. \[2010\]](#), [Assali et al. \[2016\]](#) and [Chen et al. \[2018\]](#).

By means of this [LiDAR](#) scanner, the deformation of the tunnels was measured along with a scan of the fresh rock face that opens up after every blast. The data was then combined with [RGB](#) images, analyzed and the conclusions are presented in this work. The routine for how such [LiDAR](#) and [RGB](#) measurements should be performed in underground circumstances will be discussed in this study. The most relevant parameters for this routine are the settings on the scanner that have to be taken into account, such as the resolution, lighting and the leveling of the scanner. An important step for future research would be to have a more detailed look into the possibility of the automation of the [LiDAR](#) data acquisition. An other routine that will be discussed is the data acquisition and data handling process.

1.2 RESEARCH HYPOTHESIS

This study focuses on the analysis of the application of the LiDAR deformation combined with geological mapping. This leads to the following hypotheses of this study: 1) LiDAR technology provides valuable insight in the deformation of the underground tunneling environment and allows for a numerical analysis of the results and 2) LiDAR technology combined with RGB imaging offers new potential for geological mapping to gain a better understanding of tunnel deformation behaviour.

1.3 RESEARCH QUESTIONS

The research questions addressed in this study consist of:

1. Can a LiDAR scanner provide a reliable quantitative estimation of the movement of rock in an underground environment?
2. Is the LiDAR scanner used in this research accurate enough to replace conventional tunnel convergence measurement techniques?
3. Is it possible to distinguish different rock types and geological features from the LiDAR data and how does that correlate to RGB image analysis?
4. Is there a correlation between the features observed in the geological mapping data (from both RGB and LiDAR) and the deformational analysis from the LiDAR data?

1.4 SCOPE OF THIS STUDY

The scope of this study covers the assessment of the accuracy of the LiDAR equipment itself, but also with respect to the conventional tunnel wall convergence techniques that are currently used in the Kristineberg mine: the tape extensometer and the total station measurement. The quantification of the tunnel wall deformation is in the scope of this study. What is not in scope for this study is analyzing the shotcrete thickness by periodic measurements and are therefore not taken into account. The focus also lies on the assessment of the impact of different rock types and/or geological features on the deformation of the tunnel. This assessment is covered by visual inspection, not a quantification of which rock type or feature has more impact than the other. There were two main areas where deformation was measured, which will be elaborated in more detail later. These two areas have increased tectonic activity and/or a backfilled drift close to it. The areas of the mine where less movement was predicted based on experience are not studied in this research.

1.5 THESIS STRUCTURE

The structure of this thesis is as follows:

1. **Introduction:** This introduction highlights the main objectives and the research questions.
2. **Literature Review:** This chapter focuses on the importance of this study and the potential significance with respect to previously conducted studies and industry standards.
3. **Study Area and Instrumentation:** The study area is introduced here along with a description of the geological and geotechnical circumstances present.
4. **Sensor Technologies:** In this chapter, the different types of sensor technologies used in this study are explained.
5. **Methodology:** The data acquisition, (pre-)processing and the modelling of the data is discussed.
6. **Results:** The results of the acquired data are presented and the main findings are discussed.
7. **Discussion:** This chapter focuses on how the study was conducted, what the limitations were and the significance of the results.
8. **Conclusion and Recommendations:** The final chapter summarizes the major outcomes and consists of recommendations on how this study can be elaborated.

2 | LITERATURE REVIEW

2.1 TUNNEL WALL CONVERGENCE STUDIES

In the process of excavating material in the subsurface, the in-situ stresses are redistributed, causing the rock mass to deform. "The magnitude of this deformation depends on the rock mass conditions, the magnitude, orientation and anisotropy of the in-situ stresses, the excavation method and rate, and the type and location of installed support." (Walton et al. [2018]). Closely monitoring the 3D data that visualizes the displacement over time can thus be used in order to achieve a better understanding of the in-situ circumstances. Adequately analyzing this data can provide early indicators for potential failures.

The biggest potential for the LiDAR measurement technique therefore lies mostly in predicting the overall movement of the rock mass. By properly analyzing the data and recognizing the early indicators such as rapid acceleration in the rock mass deformation can enhance the safety standards in the underground environment. "Precise modeling of under-construction and operational structures can be used to evaluate the overall deformation and state of tunnel safety, compared to traditional techniques." (Yi et al. [2019]). Other than traditional techniques, the entire 360 area of the tunnel is measured by the LiDAR scanner. This has the potential to lead to a much better understanding of the total movement of the tunnel, rather than the relative movement between specific points. To get a more thorough total picture of the convergence of a tunnel, it is of paramount importance to measure at several locations in a tunnel. A good approach would be to have at least one measurement close to the face, one closer to the middle of the tunnel and one at the outer edge.

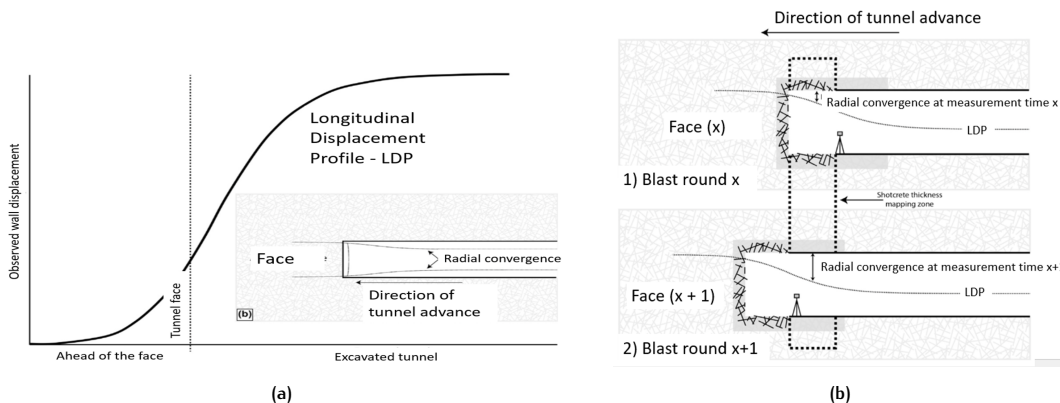


Figure 2.1: Tunnel convergence illustrations (Lato and Diederichs [2014]). (a) Tunnel convergence relative to distance from the face. (b) Radial tunnel convergence between two subsequent blasts.

As can be seen in Figure 2.1a, the convergence starts increasing as you move further away from the face. This is explained by the fact that once the tunnel progresses, material is removed and the in-situ stresses cause the rock mass to converge. However, as the absolute convergence increases when moving away from the face, the rate of convergence decreases and approaches zero. A Longitudinal Displacement Profile (LDP) is shown to illustrate how the displacement approaches a seemingly uniform value when moving away from the face, which means the tunnel displacement due to excavation will stop at a certain point in time. From Figure 2.1b can be seen that as soon as the face advances, the radial convergence progresses along with the face, until it becomes more uniform at a certain distance from the face. As mentioned before, it is important to recognize that the value of this distance is highly dependent on in-situ stresses, structural geology and lithology.

Based on this tunnel convergence development over time, it is possible to distinguish between blast-induced deformation and long-term deformation. The blast-induced deformation is the strongest of the two deformations and is observed within a timespan of at most 7 days after the blast. The long-term deformation is observed within a timespan of more than 7 days and can provide more insight in when the convergence stabilizes to an equilibrium, according to Lato and Diederichs [2014] and as the straight LDP line in Figure 2.1b illustrates.

2.2 CONVERGENCE MEASUREMENT TECHNIQUES

2.2.1 Conventional Techniques

When it comes down to analyzing the tunnel wall convergence, there are many techniques. Most commonly used in the mining industry are (Kavvadas [2003]): total station surveying equipment, tape extensometers, photogrammetric devices and laser profilers. The downside of tape extensometers is that it only provides the displacement between two specific points. The total stations allow for total distance measurements and can be linked to a coordinate system, but it also provides data only for specific points in the roof. Convergence measurements are typically conducted repeatedly until the displacement stabilizes. If the displacement does not stabilize, the measurements are continued in order to establish potential threats during operation.

Tape Extensometer

The tape extensometer is one of the most accurate tools used, with an accuracy of ± 0.01 mm (Walton et al. [2014]). However, as stated before, this tool only measures the displacement along a specific line between two points. This means that by using this tool, i.e. rigid body translation and rotation of the rock mass can not be detected.



Figure 2.2: Digital Tape extensometer (retrieved from: SoilInstruments [2021]).

An example of what such an extensometer looks like is shown in Figure 2.2. The hooks on the outer ends of the device needs to be attached to two points on both opposing walls of the tunnel. It then measures the distance along this line. That is also the downside of such measurements. Several extensometer measurements are required in an individual tunnel to get a better understanding of the actual displacement. The deformation is obtained by measuring the distance between these exact same points at a later moment in time and subtracting this distance from the first measurement.

Total Station

The total station is used by the Boliden surveyor team and makes use of optical reflectors that are installed throughout the tunnel profile as well as reference points that are installed at a stable location outside of the convergence zone to measure the deformations. The measurement is conducted by moving the station progressively forward from the location of the stable reference points towards the tunnel face. The accuracy of such total stations is typically ± 2.5 mm over 100 m in tunneling applications (Walton et al. [2014]).

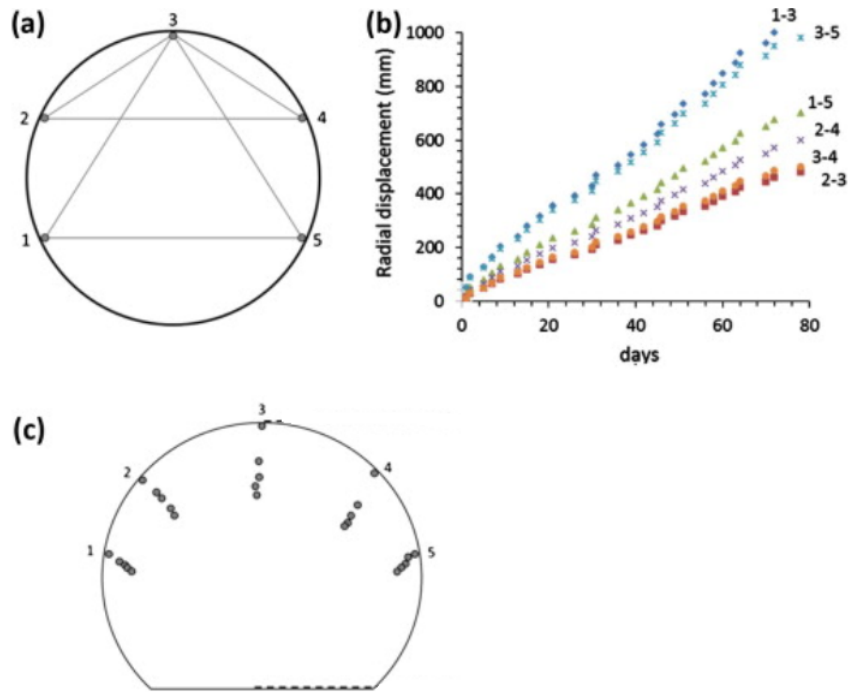


Figure 2.3: Illustration of the total station measurement techniques and the results. a) shows the control points that are measured. b) shows the deformation results over a total of 75 days. c) shows the tunnel convergence over time. (modified from: Walton et al. [2014])

Figure 2.3 illustrates how the conventional measurements are conducted by using a total station. Control points, as shown in part a of the figure, are used in order to properly analyse the convergence of the tunnel. Part b then shows the displacement overtime when looking at specific point combinations and part c visualizes the absolute displacement of the tunnel. By closely monitoring the displacement profile over a period of time, a better understanding of the development of the deformation can be obtained.

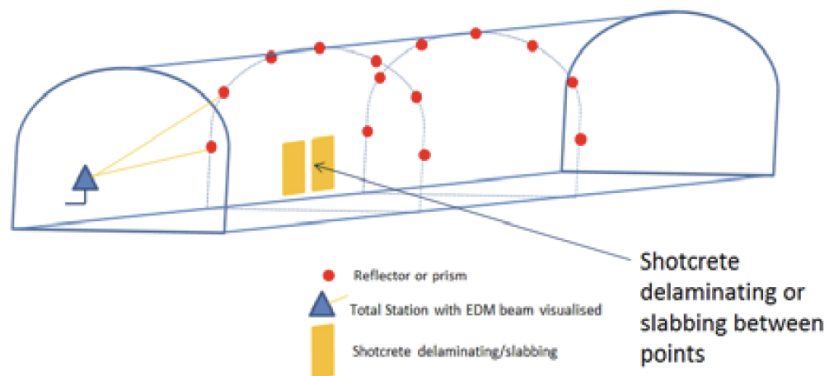


Figure 2.4: Typical Total Station measurement set-up (Cabrejo et al. [2017]).

Figure 2.4 is a sketch showing an event that would not be visible when conducting total station measurements. Between the targets that are used, the shotcrete starts to delaminate or slab by movement in the rockmass. This deformation would however not be detected by the total station, as there are no targets in this area of interest. Techniques such as LiDAR measurement technology can detect this movement in early stages because of the 360 degrees measurements.

2.2.2 Latest Techniques

GroundProbe GML

One of the latest innovative tunnel wall convergence measurement techniques is known as the GroundProbe GML scanner. GML stands for Geotechnical Monitoring LiDAR and is a new type of LiDAR equipment, of which an example is shown in Figure 1.1. This GML type of scanner has several advantages, such as real-time data acquisition, fast-paced data gathering and increased sizes of datasets. Collecting data with the GML is not only fast, but also allows for large scale data acquisition from a safe distance. According to Mah et al. [2011], the LiDAR scanners have great potential: "it also enables a large amount of data to be acquired efficiently at a safe distance from potentially hazardous rock faces or areas that otherwise would be inaccessible."

In conventional time-of-flight LiDAR (TOF LiDAR) systems, the distance measurement is conducted by measuring the time for the laser pulse to be projected onto a surface and then reflected back to the camera. However, the GML uses phase-shift principles, which leads to higher precision when compared to the conventional systems. The trade-off is the distance, which is generally lower than for TOF LiDAR scanners due to aliasing. For tunneling applications, this trade-off is not particularly relevant, according to Walton et al. [2014].

A study has shown that when the scanning was conducted approximately 5 minutes after mechanical scaling of a blasted room (so little time for dust dispersal), there was minimal apparent degradation of scan quality due to dust. However, "The rigorous mechanical scaling did cause damage to the blasted rock surface and it was noted in the field that some structural features were obscured by the scaling marks." (Fekete et al. [2010]). This implies that the ability to correctly identify the discontinuities in the area of interest would be highest if the measurement is performed before the mechanical scaling, which in turn however may underestimate the thickness of the shotcrete that is applied.

The LiDAR measurement technique is able to visualize outcrops and from that, generate 3D models. From these models, geologic and discontinuity data can be derived. This technique enables geologists to measure a tunnel or an outcrop fast and consistent. However, the terrestrial mapping of the discontinuities is limited by the exposure of their corresponding surfaces. To elaborate on this, points on a centimeter scale are grouped together in order to form a larger surface. This leads to the fact that the overall resolved discontinuity surface in such a LiDAR image could be at a too large scale. However, this measurement technique can prove to be very useful for visualizing large scale discrete features as they are more easily identified without any processing (Fisher et al. [2014]).

The analysis of discontinuities by LiDAR has many advantages. It allows for detailed mapping of structural features back at the office, allowing for the specialist to spend more time on analyzing other characteristics on-site, such as alteration, water inflow and discontinuity filling. On top of that, the scanning measurements allow for the documentation of the rock mass which can easily be reinterpreted by other specialists. This is useful for getting a second opinion in case of doubt. Finally, there is an option to automate the discontinuity extraction of the data, which would automatically identify groups of mesh triangles with similar normal vectors. This method is attractive in its ability to detect discontinuities objectively. However, studies have so far pointed out that current algorithms often provide too much noise in the results (i.e. due to rock damage) that can lead to the masking of significant structural information (Fekete et al. [2010]).

The data sets obtained through the measurements have shown to be highly advantageous regarding their ability to observe discrete features in the rock mass, along with their corresponding orientation and location. This obtained information can be used and analyzed when setting up the monitoring system in the identified zones of interest and to predict the conditions in nearby excavations. The alignment of several scans from successive blasts can prove to be advantageous in terms of identifying features that are only visible as lineations in the face. "Features that may have been overlooked or dismissed after one or two excavation rounds may reveal themselves as significant over multiple rounds." (Fekete et al. [2010]).

In a tunneling environment that is in production, it is not always possible or practical to have permanent survey markers (or targets) in place. In order to measure the tunnel convergence by means of a total station, prisms are often installed at specific sections around the perimeter of the tunnel. If one (or more) of those prisms is knocked out of place or comes loose, the measurements with the total station can no longer be conducted in that section. However, by using the GML, the processing software can detect and eliminate one or more prisms. The minimum required number of prisms for a scan is three, the other prisms can be eliminated if their location have changed too much with regards to the first scan.

The intensity of the LiDAR data can be used to get a better understanding of i.e. different lithological units in the exposed rock faces in the underground tunneling environment. As stated by Giglierano [2010]: "Because most lidar systems use a laser that emits light in the near-infrared portion of the spectrum, the intensity of lidar return is directly related to the near-infrared reflectance of the target material." This characteristic can be used when analyzing the intensity data obtained from the measurements performed during this study. The intensity of the different litho-types that will be discussed in later chapters can be analyzed and a distinction between different geological structures can be made. From the intensity data, two different images can be constructed: a first return and a last return image.

However, such innovative techniques also come with new challenges. A number of challenges are discussed in the following paragraphs. Occlusion (or ‘shadowing’) of a surface is one of the main issues in the laser scanning of a surface. This phenomenon limits the acquisition of the data due to the surface view of discontinuities being limited or even fully obstructed, and thus will not be registered as such by the measurement (Lato et al. [2010]). An example of this occlusion effect is shown in Figure 2.5.

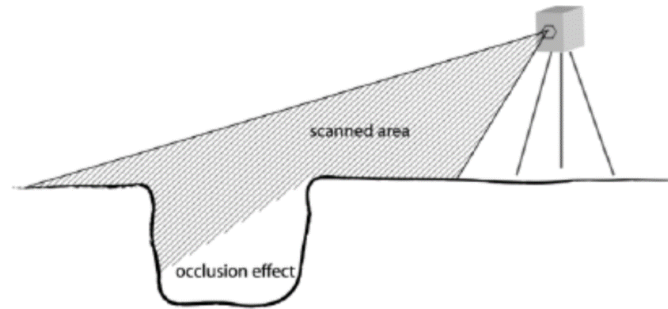


Figure 2.5: Occlusion effect (Höfle et al. [2013])

The limitations of regular LiDAR scanning that have to be kept in mind are that some measurements can lack part of the data by the multiple returns obtained through the laser beam hitting a sharp edge before returning to the sensor. On top of that, the frequencies of the laser can be amplified by metal such as bolts, equipment, machinery or even bolts. Finally, the laser can not see through i.e. a mesh or through cables. This has to be taken into account when processing and analysing the data.

An other downside of the LiDAR scanning method is for example the phenomenon where the beams are split in case the laser hits a sharp edge which leads to the device measuring multiple returns from what is supposed to be one measurement. The GML has the option to automatically select either the first or the last return of that beam, which is illustrated in Figure 2.6.

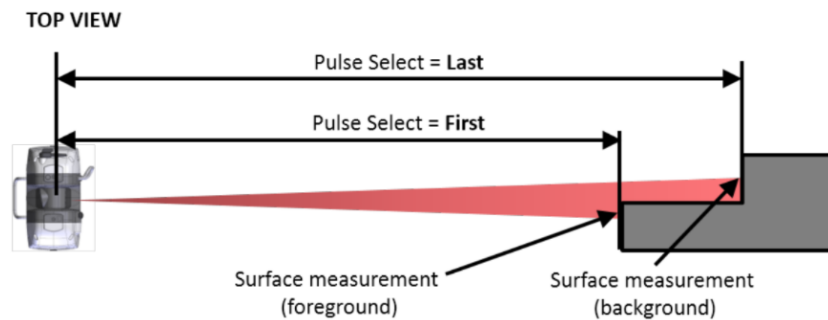


Figure 2.6: Pulse Select (Boliden [2020]).

“Compared with total station technology, 3D LiDAR technology also suffers from low position repeatability as scanning occurs very quickly and position repeatability is not required for single survey scans.” (Cabrejo et al. [2017]). It may be difficult to improve the accuracy compared to conventional techniques (i.e. the Leica Total Station and the extensometers). The biggest limiting factor is the repeatability of the scans. In order to get the most accurate results, it is recommended to mount the scanner on a (stable) wall and conduct continuous instead of periodic measurements.

When using a tripod, the positioning of the scanner is very likely to change, even by just a little, in between measurements. One of the reasons for this is the fact that the shape and position of the floor can change significantly from scan to scan due to mining activities, such as mucking, leveling or even simply the trucks driving around. This quickly leads to a positioning error when conducting the same scan at a later stage. Additional deviations can be caused by i.e. a slightly different positioning of the tripod (through either the absolute position of the legs or the respective angle of the legs to each other) or by setting a different height of the scanner. As this involves a lot of human interaction and gives room to human error, it is recommended to automate such measurements in the future and have a built-in automated leveling system along with a 3D positioning system that can provide real-time data of where the scanner is and how it is positioned (Walton et al. [2018]).

Another issue that can occur, when measuring in a tunnel environment that is in operation, is that time and space can be a limiting factor allowing for maybe only one scan per round. This issue may restrict the reliability in terms of ‘rushed’ measurements, leading to reduced or even wrong detection of

i.e. discrete structures. This wrong detection can be a result of unfavourable angles even though the tunnel environment provides for a wide range of viewing angles such that the occlusion could have been reduced for the characterization of the rock.

However, studies have shown that it is definitely possible to collect “good quality data with a tripod setup in an active tunnel environment without disruption of the construction workflow.” as stated by [Fekete et al. \[2010\]](#)). It is mentioned that the [LiDAR](#) data might not be as accurate as when using a continuous measurement setup, but that the general movement of the rock can be identified. On top of that, zones that show strong deformation can be identified in early stages as potential failure zones, thus improving safety and stability standards.

An additional limitation with respect to the required time of each measurement is due to the installation of prisms and/or reflectors to achieve optimal accuracy of each scan. In [Contogianni et al. \[2007\]](#) it is stated that the use of reflectors delivers lower accuracy than the usage of prisms, which was also found by [Cabrejo et al. \[2017\]](#). A downside of installing the prisms is that it is necessary to drill holes and install plugs before the prisms can be mounted, while the reflectors can commonly be used in already mounted and georeferenced bolts. This means the usage of reflectors can in some situations save time, but reduces measurement accuracy. This trade-off must be taken into account when developing a measurement plan, because it is always the highest priority to minimize the impact on the production cycle.

The conditions of an underground mine can be challenging for the usage of such measurement technologies. For example: the limited distances to the target sheets (in small tunnels), which can be problematic if the scanner is too close to the face. For some scanners, 5 – 10 m is considered too close. However, for the [GML](#) this is not a problem. The maximum range of the [GML](#) is limited to 40 m with the recommended settings, which should also be sufficient for most underground environments. Then there is the limitation of dusty and dirty working conditions in the underground mining environment. It becomes problematic if the lense of the laser is covered in dust. The particles that are floating in the air can disturb the laser intensity or even the angle, leading to wrong measurements and can eventually lead to wrong conclusions being drawn from the data ([Mah et al. \[2011\]](#) and [Fekete et al. \[2010\]](#)).

2.3 APPLICATION OF LIDAR FOR GEOLOGICAL MAPPING IN UNDERGROUND MINES

The usage of [LiDAR](#) equipment has become more and more common in geotechnical applications such as mining. One of the purposes can be the characterization and analysis of the fresh rock in a tunnel environment. “The geological engineering community utilizes laser imaging for landslide monitoring and more recently, rock outcrop characterization, rockfall hazard assessment and stratigraphy modeling.” ([Fekete et al. \[2010\]](#)).

Several studies focus on the use of geological mapping in underground mines. As mentioned in [Thiele et al. \[2021\]](#), enhanced digital outcrop models attributed with hyperspectral data, which is very complementary to [LiDAR](#), can provide for a data-driven mapping method with high detail levels. The mapping of such data allows for analysis of geological exposures, mine faces or cliffs. The approach of gathering digital outcrop models allows for more detailed collection of spatially contiguous information on the exposed mineralogy, which helps in the process of quantifying the mineralising process and thus allows for the optimization of mineral extraction ([Thiele et al. \[2021\]](#)).

In addition to being able to visualize the detailed geometry, these datasets commonly contain reflectivity or intensity information, which can be used to distinguish between different lithologies and geological structures. By analysing the rock in an underground environment, a better understanding of the structural geology can be achieved. By properly understanding the geology, it can become easier to predict for instance failure within the rock mass or the convergence of the tunnel. The analysis of such geological [LiDAR](#) data can be conducted on the intensity of the reflection of the light, range from the scanner and i.e. triangulated point clouds ([Rarity et al. \[2014\]](#)). For cross-referencing, conventional [RGB](#) images can be taken and analyzed along with the point cloud, which is discussed later.

Another aspect to take into account is that “outcrop datasets are typically very dense in some areas and have low to non-existent data density in other areas, depending on the geometry, extent and accessibility of the exposures.” ([Rarity et al. \[2014\]](#)). The irregular data distribution sometimes leads to misinterpretations or reprocessing of the data being required. Therefore, it is recommended to collect [RGB](#) images when performing a scan, so that the scan analyses can be verified.

As [Fekete et al. \[2010\]](#) describes, the [LiDAR](#) scanners are useful tools when analyzing fresh rock. The characterization of the outcrop can be done based on varying intensity levels. The subjectivity of the initial analysis is removed by using the scan data. There is still some subjectivity when it comes to interpreting the intensity differences, but it is less apparent.

As mentioned in [Chen et al. \[2021\]](#), “Searching for an efficient and reliable method to reduce manual intervention and subjective parameter selection during the discontinuity characterization process of rock tunnel faces is an important task.”. The analysis of 3D Point Cloud Data ([PCD](#)) provides a solution for that task. However, it must also be noted that, as mentioned by [Fekete and Diederichs \[2013\]](#), current automated

joint selection algorithms are not sophisticated enough to distinguish between i.e. blast damage or scaling, and have difficulties if they are applied to tunnel profiles that are not planar-based.

Gaining a thorough understanding of the discontinuities is important because they have a significant impact on the hydrological and mechanical characteristics of the rock mass (Goodman [1989]). The discontinuities control the complexity, heterogeneity and anisotropy of the rock mass. During the construction of a tunnel, dense and complex discontinuities are often encountered. Such discontinuities may lead to rock failure, or in worst-case scenarios even the collapse of the tunnel resulting in huge economic losses and safety issues. As mentioned by Assali et al. [2016]: "In order to ensure a smooth tunnel excavation process, there is a growing demand for rapidly-acquired tunnel face datasets containing key discontinuity features which can be automatically quantified." The LiDAR scanning technology allows for this rapid acquisition of large datasets with the potential to give more detailed insights into the discontinuities present in the rock mass.

Conventional measurement techniques include i.e. the geological compass or measuring tapes. They are commonly used to collect discontinuity sets and in order to get an understanding of the most unstable regions (Chen et al. [2018]). However, this collection of information is almost always incomplete, very inefficient and prone to human error. Therefore, techniques that do not require a direct contact with the rock mass have grown in popularity in recent years (Chen et al. [2018]). Those techniques include the LiDAR scanning technique and digital photogrammetry in order to obtain 3D point cloud datasets of tunnel faces.

The LiDAR sensors (or sometimes referred to as laser scanners) have the potential to acquire data of high resolution (with a density of 10^4 points per m^2) with high accuracy (standard deviation of less than 1 cm at 100 m distance, according to Riquelme et al. [2014]). "Such systems allow obtaining the coordinates (X, Y and Z) of the points of a surface at high speed (more than 222.000 measurements per second)." (Riquelme et al. [2014]). The GML allows for a rapid deployment of the equipment and a fast measurement method to acquire a lot of data about the fresh rock, without disturbing the mining activity too much.

The application of LiDAR technology and RGB sensors in complex (underground) geological environments can provide more detailed insight in the structural geology and the lithological composition of the fresh rock. The application of such technologies have become increasingly popular over the past 10 years. These type of experiments can be conducted by means of mounting a LiDAR scanner (containing an RGB camera as well) on a tripod and gathering the data close to the face, to ensure that the most of the exposed rock is captured by the scan.

Other studies suggest the use of Unmanned Aerial Vehicles (UAV), as it is common for underground tunnels to be prohibited from access for the engineering personnel due to mining activities, hazardous conditions or limited time before the next activity starts (Turner et al. [2020]). By using these technologies, it is possible to identify i.e. wedges found in open stopes, or even individual discontinuities if the data contains enough detail. Additionally, the geological setting and lithological composition of the exposed rock surfaces can be analyzed from this data.

On top of analyzing the varying intensity levels of an outcrop, the discontinuities can be distinguished (as described in section 2.2.2). The discontinuity extraction from the LiDAR data is mostly done by identifying groups of mesh triangles that have similar normal vectors (Fekete et al. [2010]). Therefore, this way of interpreting the discontinuity data is very objective compared to conventional methods. In this research, the MapTek PointStudio software has been used to analyze and group the different discontinuity structures present in the fresh rock, based on their normal vectors.

By making use of the varying intensity levels of the LiDAR data, a clear distinction between different rock types can be made. Typically, airborne LiDAR has been studied in order to analyze the potential of the discretization of different lithologies. An example of such a classification is shown in Figure 2.7.

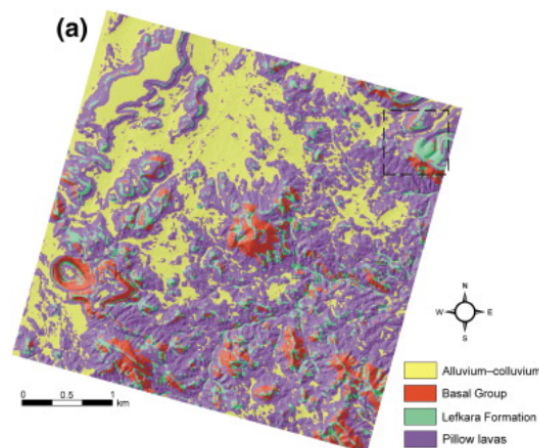


Figure 2.7: Lithological classification of airborne Lidar data, modified from Grebby et al. [2010].

2.4 APPLICATION OF LIDAR FOR DISPLACEMENT MEASUREMENTS

There remains a lot of (unexplored) potential for data collection regarding usage of a LiDAR scanner. With limited time allocation to engineering characterization because disruption to the excavation workflow must be minimized, it is important to explore what the possibilities are in this aspect. As the rate of LiDAR data collection has advanced recently (Chen et al. [2021]), equipment such as the GML can be a practical addition to the excavation cycle leading to increased safety and reduction in overall cycle time.

As stated by Fekete and Diederichs [2013], "As a drill-and-blast tunnel advances, LiDAR scanning allows for the documentation of the rock mass by collecting millions of rock surface point locations in space creating geometric scenes." Databases consisting of geological data can be created by a thorough interpretation of the virtually visualized rock mass. Such analyses can be much more extensive than what is traditionally obtained by hand-mapping as means of geotechnical data collection. On top of that, as Chen et al. [2018] stated, an other big advantage is the fact that it is much easier to store and share the interpretations and analyze the data together with colleagues.

Such databases containing geotechnical information can subsequently be used for discontinuum modeling to get a more thorough understanding of the structurally-controlled failures that occur in the rock mass. These models allow for far more representative block modelling than traditionally possible due to the excessive amount of information gathered.

By using the LiDAR rock mass models, rock mechanical engineers can confirm certain failure mechanisms that occurred, calibrate persistence, test rock mass performance and more importantly identify critical joint sets or patterns that lead to stability issues and hazardous situations. Fekete and Diederichs [2013] states that by integrating the LiDAR data into the stability analyses, the design of the tunnel support can be fine-tuned to the actual rock mass performance. By optimizing such designs, the costs of the projects can be minimized and the construction schedule can be shortened by removing unnecessary support structures from the design.

Figure 2.8 illustrates an example of the positioning of different scan locations in the same tunnel environment. In order to get the best understanding of the movement of the entire tunnel, the positioning of the scanner has to be chosen appropriately in order to capture as much data as possible. The positioning of the scanners shown in the figure allow for the most comprehensive data gathering, by having overlap in the data obtained from the different stations.

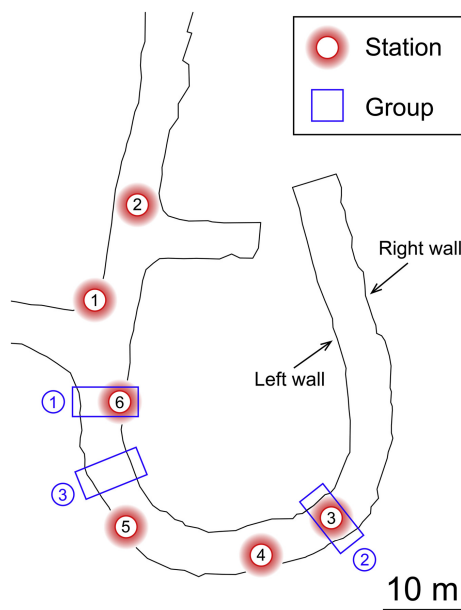


Figure 2.8: Different scan locations used in U-shaped tunnels (Chen et al. [2018]).

In this specific underground tunneling environment it was chosen to use 6 distinct LiDAR scanning stations (or locations) based on the line of sight and the requirement for overlapping datasets from those locations. Additionally, the author of this study has chosen to use different groups to analyze, where group 1 contained noisy data and the other two groups did not. The grouping method is not used in this study, but the use of different scan locations is. To get a more thorough understanding of the movement of the whole tunnel, it is important to analyze the movement from several locations.

An other application of the LiDAR deformation datasets is analysis of the shotcrete thickness. In order to get an understanding of the shotcrete thickness on the walls, it is possible to align 3D LiDAR measurements with photogrammetry data from several sequential blasts in a 3D environment and then analyze the spatial difference between the different models. This spatial difference provides an estimate for the thickness of

the shotcrete. However, convergence of the rock mass is not included in this analysis, which may lead to overestimating of the shotcrete thickness. This overestimation can be corrected based on rock mass convergence rates that were measured at an earlier stage or by numerical modelling (Lato and Diederichs [2014]). However, it must be noted that those convergence rates are not constantly the same, so this is only useful for an early estimation and not for a detailed analysis.

2.5 APPLICATION OF RGB IMAGING FOR GEOLOGICAL INTERPRETATIONS

As mentioned by Desta and Buxton [2018], "RGB imaging has a good potential for mapping of visually distinct minerals in underground mines". The combination of the use of both RGB and LiDAR technologies to classify the different lithologies present in the exposed rock surfaces allows for a rather detailed analysis of the (structural) geology.

In order to distinguish between different lithologies, one of the methods that were used as RGB image classification method in Desta and Buxton [2018] consists of the Support Vector Machine (SVM) algorithm. "For classification, SVM finds the optimal boundary (hyper-plane) that differentiate the two classes using kernel functions in many forms". Since it allows for the handling of non-linear classification cases, it is a very useful algorithm for heterogeneous rock masses. By combining an unsupervised distinction based on varying intensity levels along with supervised RGB image classification, a better understanding of the rock composition and its correlation to the rock movement can be obtained. These methods combined have the potential for geotechnical engineers to get a more thorough understanding of tunnel wall convergence.

2.6 KEY OUTCOMES

An important take-away from the literature study is that there may be a difference in deformation shortly after the blast and when looking at the deformation rate over a longer period of time. The convergence of the tunnel seems to be the highest shortly after the blast, and after that, the tunnel comes to an equilibrium state, as shown in Figure 2.1b. Therefore, the deformation cyclus is separated into blast-induced deformation (≤ 7 days) and long-term deformation.

When it comes to conventional measurement techniques, the most important limitation is that it only provides information about a very limited area of the tunnel. The LiDAR scanner has the potential to remove this limitation and provide the geotechnical engineer with plenty of information about the tunnel wall convergence.

Combining the GroundProbe GML LiDAR deformation data gathering method with geological mapping by means of both LiDAR scanning and RGB imaging, the tunnel deformation can be thoroughly understood. It is of paramount importance to understand why, when and how fast the rock mass in an underground environment moves to ensure tunnel stability and the safety of the workers.

3

STUDY AREA AND INSTRUMENTATION

This study focuses on measuring and analyzing the tunnel stability through 3D LiDAR scanning in the Boliden Kristineberg Mine, located approximately 100 km west of the Boliden Area in Sweden as shown in Figure 3.1. This underground mine produces material from polymetallic mineralizations of Volcanogenic Hosted Massive Sulphide (VHMS) (Boliden [2020]). Those mineralizations were explored until 1400 m depth along a plunge of 30 degrees and were found to be approximately 3 km with the mineralization thickness ranging from 1 to 7 m.

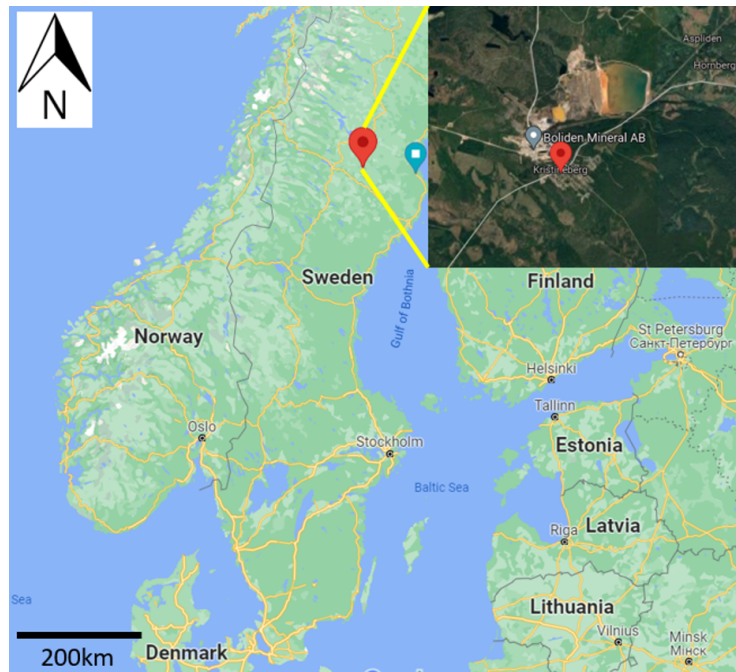


Figure 3.1: Location of the Kristineberg Mine (modified from Google Maps)

3.1 GEOLOGY

This section covers the geological setting of the study area. The regional geology will be covered, along with local geology, lithologies, orebodies of interest, structural geology and the mineralizations present. The mine lay-out and the scale of the mine will be addressed in section 3.2.

3.1.1 Regional Geology

The Kristineberg underground mine is located in the Skellefte District, which is an area that originates mainly from the Paleoproterozoic (2.6-1.6 Ga) era. The Skellefte District consists of a combination of volcanic and sedimentary rocks located in the Västerbotten region, Northern Sweden. In total, the District hosts more than 85 VHMS deposits, of which 31 are currently in operation or have been mined before (Boliden [2019]).

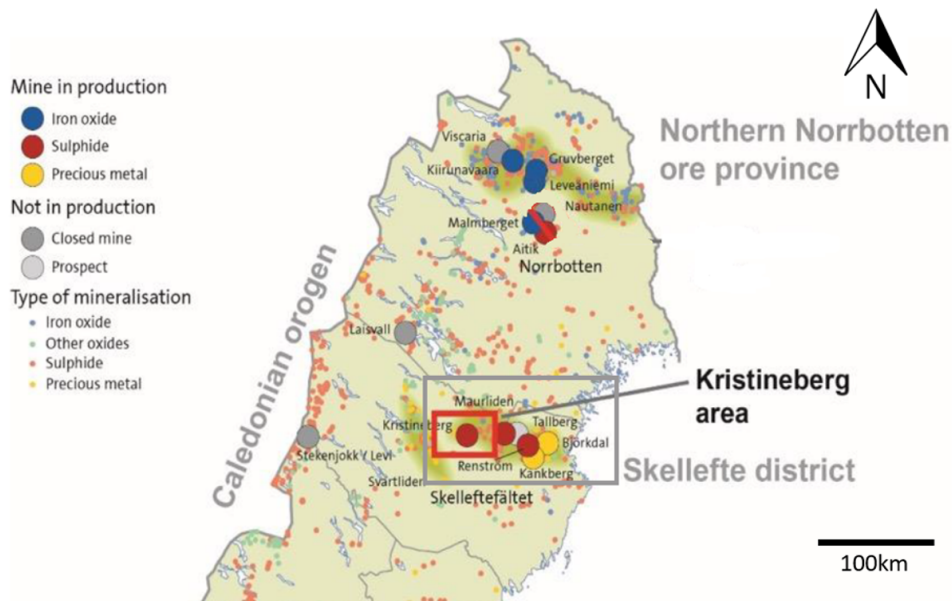


Figure 3.2: Regional deposits in the Skellefte District (modified from: Schwarz et al. [2020])

The VHMS deposits of the Skellefte District are primarily hosted by a volcano-sedimentary sequence. The upper part of the sequence consists of volcanic material while the part below consists of intermediate to juvenile, felsic volcanoclastic rocks and sub-volcanic intrusions (also known as the Skellefte Group rocks). The Skellefte Group rocks are overlain by the Vargfors group, which is composed of shales, turbiditic sedimentary rocks and conglomerates. The outer Northern and Southern regions of the area consist of syn-volcanic granitoids, while sedimentary Greenschist facies are found at the Eastern and the Western borders. More detail about the present rock formations is shown in Figure 3.3.

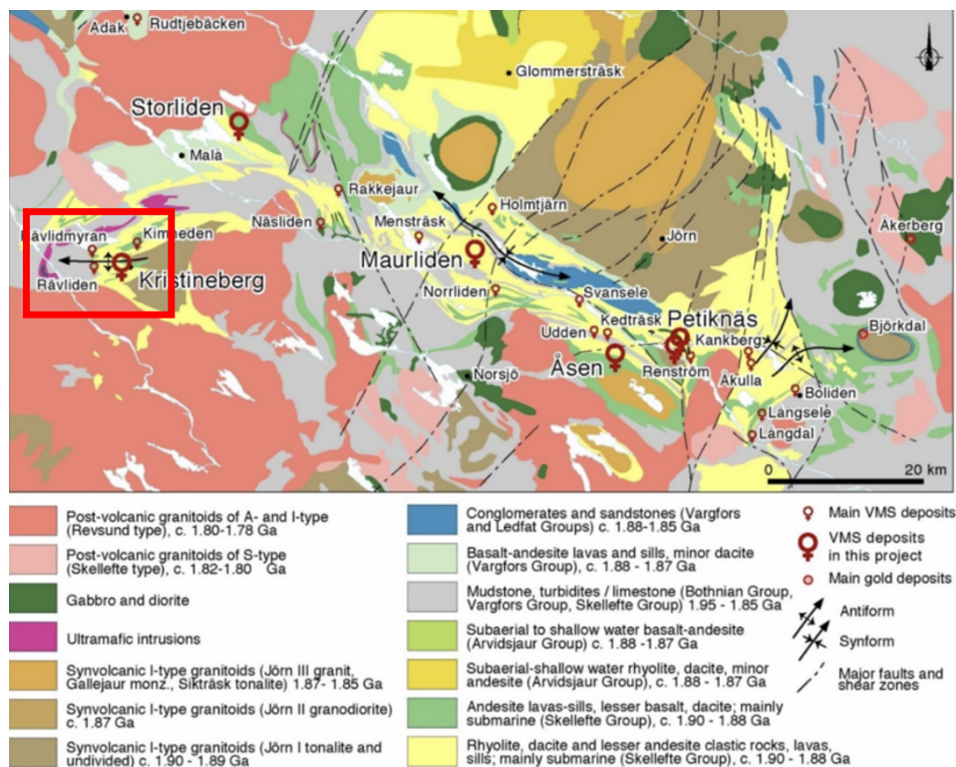


Figure 3.3: Geology of the Skellefte District (modified from: Boliden [2019]).

As marked in the red box on Figure 3.3, it becomes clear that the deposit which is extracted in the Kristineberg mine lies on an anticlinal structure and consists mainly of rocks that are approximately 1.90 Ga old.

The geometry and orientation of the VHMS is primarily controlled by an early stage of ductile deformation along with the large scale thrust-and-fault system of Kristineberg. The so-called Kristineberg Camp is

located in the westernmost part of the Skellefte District, as shown in Figure 3.2. The volcanic sequences are exposed in two large anticlinal structures in this area, of which one is in the Kristineberg Camp.

To the North of the mine lies the Viterliden intrusion, which is a sub-volcanic intrusion ranging from hornblende tonalite in the very centre to a plagioclase porphyritic trondjemite at the outer edges. The origin of the trondjemite is depicted in Figure 3.4 as 'mine porphyry', because it has intruded the altered rocks of the foot walls of some of the orebodies. The Kristineberg Camp is bordered by post-orogenic granites. The rocks within the deposit have been hydrothermally altered significantly and metamorphosed to upper greenschist or lower amphibolite facies.

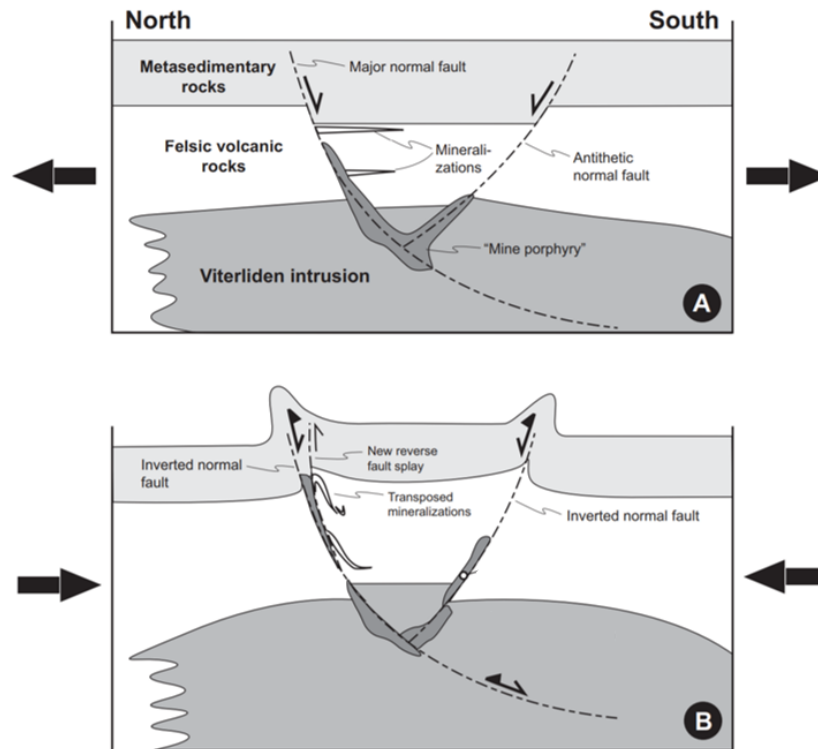


Figure 3.4: Schematic sketch of the tectonic evolution of the Kristineberg area (not to scale). A) Illustration of the syn-extensional volcanism and mineralization sedimentation that occurred at 1.89 Ga. B) Illustration of subsequent crustal shortening leading to basin inversion and the transpositioning of mineralizations. (Weihed et al. [2011]).

The intrusion that is in the centre of the anticlinal structure has been called the 'Kristineberg massive' and is dated to be 1.9 Ga old. According to Bergström et al. [1999], the Kristineberg massive was either a basement to the rocks found in the Skellefte Group, or stated that when both rock units are presumed to be from the same era, that they would be older than the volcanic rocks found in the Eastern and Central part of the Skellefte District. An other option is that the Kristineberg massive was the result of a magma chamber deep in the earth, which could be related to the Skellefte Group volcanism in the area. The age interval obtained by Weihed et al. [2011] for the intrusive and supracrustal rocks supports the theory that the Skellefte Group defines a laterally continuous volcanic belt throughout the entire Skellefte District. The local geological setting is discussed in more detail in the next subsection.

3.1.2 Local Geology

The local geology at the Kristineberg Mine is discussed in this section. The host rocks present are altered and metamorphosed to various assemblages of the present lithologies of i.e. chlorite, quartz, muscovite and biotite. The general trend in the Kristineberg area is broad-scale alteration of the minerals. The host rock deposit includes several rhyolite types next to the lesser dacite and andesite found.

The anticlinal structure in which the Kristineberg area lies plunges moderately to the West and is adjacent to a Vargfors syncline containing ultramafic sills. The anticline consists mainly of felsic lavas, subvolcanic intrusions and volcanoclastic rocks from the Skellefte Group.

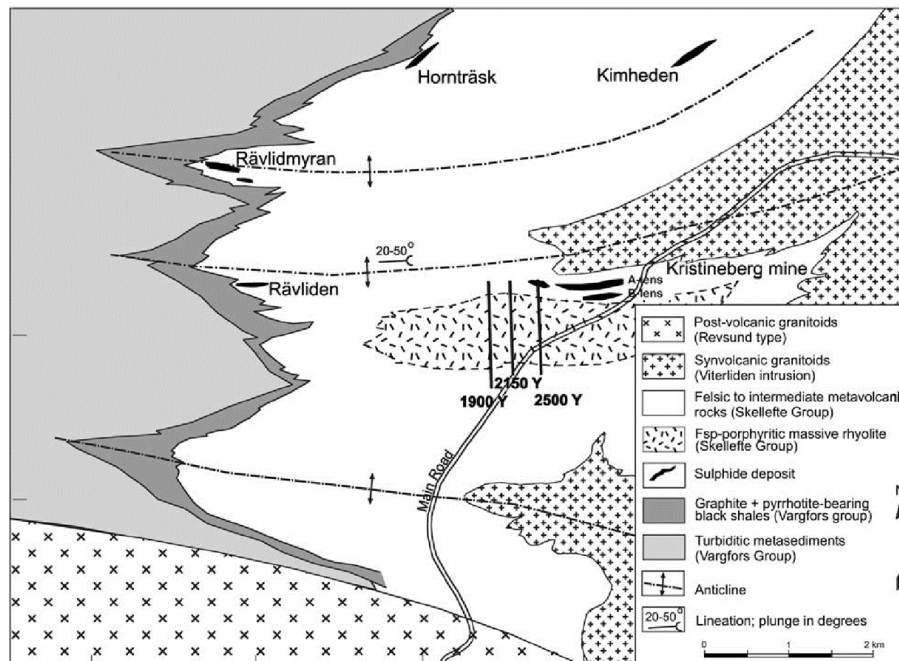


Figure 3.5: Local geological setting (Arebäck et al. [2005]).

As shown in Figure 3.5, the volcanic sequence is cored by the Viterliden intrusion. This subvolcanic intrusion is foliated and ranges in composition from hornblende tonalite towards a margin of plagioclase porphyritic trondhjemite. Mine exposures have indicated that the contacts of the Viterliden intrusion (or: mine porphyry) sometimes intrude the footwall rocks of the orebodies and therefore postdates the deposit (Boliden [2019]). As found by Arebäck et al. [2005], "Recognition of primary rock types and textures is difficult in much of the mine area.". Most of the altered and metamorphosed rocks in the Kristineberg deposit consist of a variety of quartz, chlorite, pyrite, muscovite and phlogopite. The large scale thrust-and-fault system as described earlier is also seen in the orebodies. The offsets of the lenses found in the mine are a sign of the thrustured deformations (Boliden [2019]).

3.1.3 Lithologies

The deposit in the Kristineberg area consists mainly of pyrite and zinc blende with the amount of chalcopyrite increasing towards the bottom of the mineralization. Chlorite schist is known to be the host rock for the mineralization. Several ore types are present in the Kristineberg area, of which the primary deposit consists of a massive pyrite orebody that contains gold, silver, copper and zinc, which has been deformed into numerous ore lenses. The chief ore-types have been distinguished based on the following local terminology based on Boliden [2019]:

- Copper-pyrite ore (wet ore)
- Zinc ore (ZnS-bearing pyritic ore with chalcopyrite and galena)
- Dry (quartzitic) ore
- Impregnation ores towards host rock

A chlorite-quartz schist alteration product of the granite present in the area is found towards the southern areas of the mine. In the mine it is also observed that sericite and greenstone dikes cut the granites as well as quartz-tourmaline veins. The hanging wall sometimes consists of extreme chlorite rock that transitions towards soapstone (Boliden [2019]).

3.1.4 Orebodies

This subsection covers the mineralization zones present in the Kristineberg underground mine. The first orezone of interest is called the L-zone and consists of quartzites that generally show strong hydrothermal alteration, with lenses of chlorite schist in the orezone as well. In the drill cores both metamorphic as well as hydrothermal andalusite have been found, mostly in the western part of the orezone, where the abundance varies strongly. The VHMS is associated with the chlorite schists present in this zone, but not limited to the schists. The geometry and orientation of the VHMS is controlled mainly by a period of early ductile deformation in addition to the larger scale thrust-and-fault system that is found in Kristineberg area. From the drill core analysis in Boliden [2019] it has become clear that the brittle structures and associated gold mineralisations are to some degree related to the occurrence of the chlorite schists.

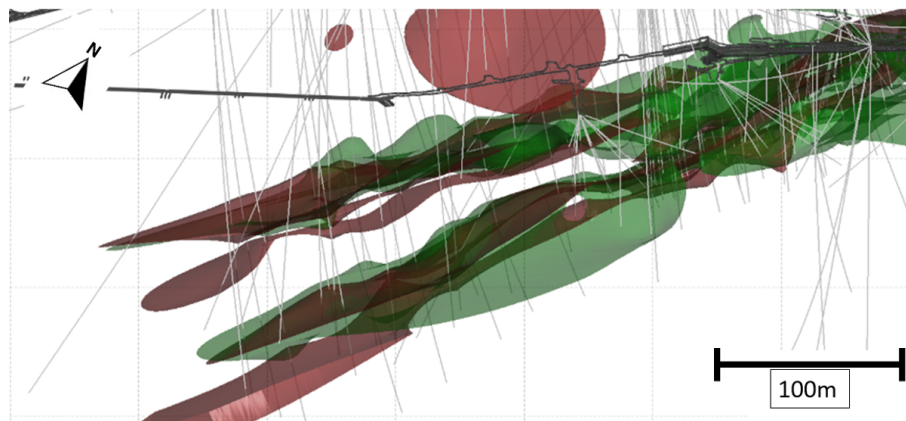


Figure 3.6: Illustration of the L-zone orebody. Chlorite schist is shown in green and massive sulphides in red (modified from: Boliden [2019]).

In Figure 3.6 the orebody of the L-zone is shown. The chlorite schist is visualized with the green color and the massive sulphides in red. The upper parts of the orezone generally contain more zinc while the deeper parts of this orezone contain more copper. Both mineralisation trends are associated with chlorite schists, and the albite silicification intensifies further down the ore. The primary ore minerals are sphalerite and chalcopyrite. Most of the ore is found in lenses that host the mineralisation and are primarily associated with chlorite schists.

According to the geological mapping and the drill cores, the L-orebody consists primarily of chlorite schist. The schist rock has been tested on its compressive strength and if stress levels exceed 80 MPa, the rock cracks severely, resulting in extensive reinforcement being necessary. The geometry of the L-orebody shows that it is approximately 300 m long and has widths ranging from 15 to 20 m. The height varies but is up to 25 m in the West and has a maximum of nearly 75 m in the Eastern center.

The second orezone of interest is called Kopparklumpen (or shortened: KK), referring to the copper content in this orebody. The mineralization that forms the Kopparklumpen is composed of strong chlorite altered rocks with moderate to strong schistosity and some primary features (hard, resistant to erosion).

The mineralization itself then consists of three Zn-rich zones and two Cu-rich zones and is a massive sulphide mineralization with massive blocks of pyrite, sphalerite and stringers (large number of small veins) of chalcopyrite. An illustration of the orebody is shown in Figure 3.7. The sphalerite consists of anhedral masses with alternating colors due to varying Fe-content. The pyrite occurs as euhedral crystals 2 – 5 mm in diameter.

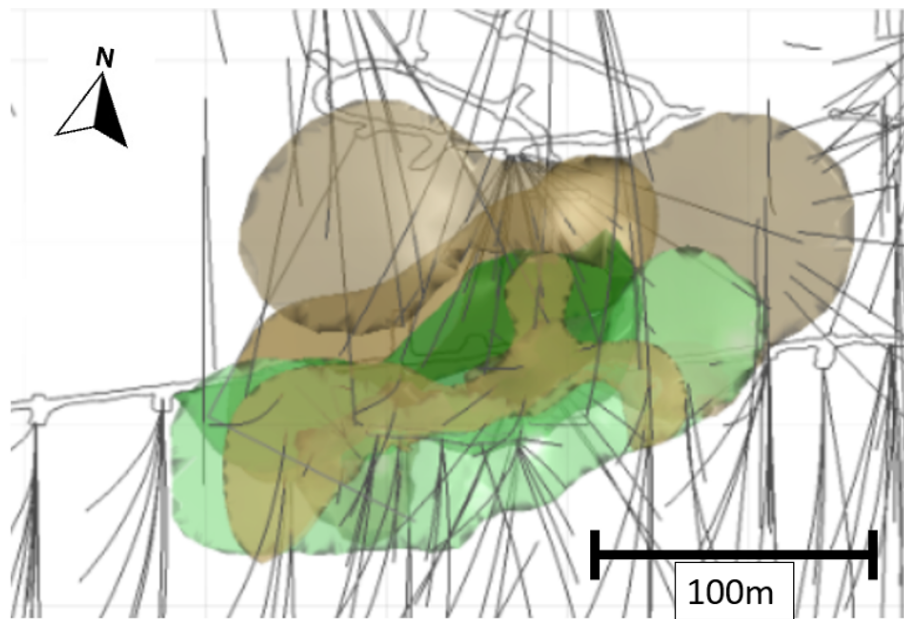


Figure 3.7: Illustration of the Kopperklumpen (KK) orebody. Cu-rich zones in green and Zn-rich zones in brown (modified from: [Boliden \[2019\]](#)).

The mineralization shown in [Figure 3.7](#) strikes approximately from East to West in the mine coordinate system. It consists mainly of pyrite and zinc blende with the amount of chalcopyrite increasing towards the bottom of the mineralization. Chlorite schist is known to be the host rock for the mineralization. Several ore types are present in the Kristineberg area, of which the primary deposit consists of a massive pyrite orebody that contains gold, silver, copper and zinc, which has been deformed into numerous ore lenses.

According to the geological mapping and the drill cores, this orebody and the rock in its vicinity consists primarily of chlorite schist. The rock has been tested on its compressive strength and if stress levels exceed 80 MPA, the rock cracks severely, resulting in extensive reinforcement being necessary. The geometry of the orebody shows that it is approximately 200 m long and has widths ranging from 5 to 8 m. The height varies but is minimally 40 m in the West, 22 m in the East and has a maximum of around 125 m in the centre.

3.1.5 Structural Geology

The Kristineberg Camp trends from NE-SW to E-W, which deviates from the WNW-ESE structural grain of the Central Skellefte District, according to [Jansson et al. \[2013\]](#). The model used in that article has shown that this alternative structure reflects the localisation of the Kristineberg Camp at the lateral termination of a significant transpressional high-strain zone, which transects most of the Central District.

“East of Kristineberg, the zone splays into several branches and defines zones of coaxial and non-coaxial deformation resulting in increasingly complex structures, including significant variations in the plunge of the large antiformal structure in which Kristineberg is located.” ([Jansson et al. \[2013\]](#)). As also described in [Boliden \[2019\]](#), those significant variations are found in the Kristineberg underground mine. There is no clear distinct geological structure and the setting is very complex.

Reflection seismic measurements in combination with geological cores obtained from drill holes near Kristineberg have found that there is a connection between the seismic discontinuities and the high-strain zones, indicating that there are ore lens geometries in the area. Those high-strain zones have led to the transpositioning of the primary strata and the individual ore lenses into moderately to steeply dipping orientations. According to [Jansson et al. \[2013\]](#) those high-strain zones most likely also controlled the localization of the deposits during the mineralization, even earlier. The reverse movements along the S-dipping high-strain zones has led to the most significant tectonic transposition.

3.2 MINE BACKGROUND

The Kristineberg Mine has been producing material over the past 80 years. It produces approximately 750,000 t per year and is therefore the largest contributor (in tonnage) to the Boliden Area process plant. The mining is currently conducted through drilling and blasting along with the cut-and-fill methodology at depth levels between 900 and 1250 m. The production of the mine of 2020 is visualized in [Table 3.1](#).

Table 3.1: Production and corresponding grades at the Kristineberg Mine in 2020 ([Boliden \[2020\]](#)).

Year	Material mined [kt]	Au [g/t]	Ag [g/t]	Cu [%]	Zn [%]	Pb [%]
2020	541	0.6	45	0.52	5.73	0.43

The deposit contains approximately 2.5 million tonnes of probable and proven reserves. Additionally, there is an estimated amount of 6.6 million tonnes of measured and indicated resources. The deposit consists of several individual orebodies. One of the currently mined orebodies is the so-called L-orebody that consists of many small lenses, which all have different strikes, dips and thicknesses. There is no well-defined geological form, which means that the orientation, composition and other parameters vary significantly. The L-orebody is divided into three areas:

- L-övre, starting at 1000m depth and progresses upwards.
- L-nedre, located at a depth of 1000-1200m
- L-väst, starting at 1200m depth and progresses downward.

Of those three areas, L-övre and L-nedre are considered stable parts of the orebody when analyzing the properties of the rock mass and stresses in the rock (according to [Boliden \[2020\]](#)). The L-väst area is however different and considered a high-risk area. The rock mass consists primarily of chlorite schist (chlorite schist is the host rock), which is weak and commonly shows higher stress levels due to the depth and a complex mine plan. The reason that L-väst is studied in this research is that there are many (structural) stability issues in this L-väst area during production, which may be due to an other (older) drift being present next to the current tunnel. The orebody is approximately 325 m in length. In the L-orebody, convergence measurements have been conducted on the shotcrete in room L62H on a regular basis by the author.

The second area of interest that was investigated in this study was the so-called Koppur Klumpen (from now on referred to as KK) deposit within the M-orebody. Displacement measurements and a geological interpretation are conducted in this orebody. The KK2 drift is of interest because measurements have shown that it is an active tectonic zone and there have been stability issues in the past. The orebody locations of the two areas of interest, L62H and KK2 (with KK3 on top), are shown in [Figure 3.8](#).

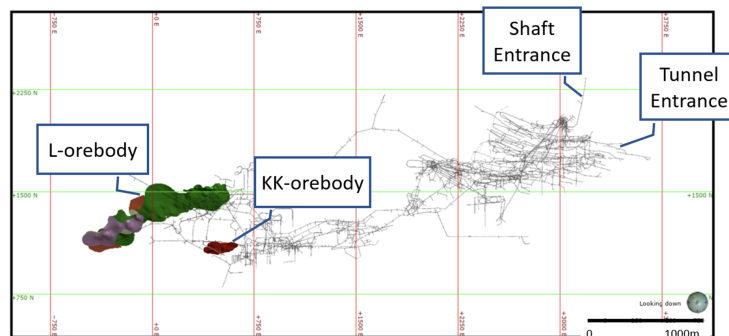


Figure 3.8: Mine system layout along with the respective locations of the two orebodies of interest (modified from [Boliden \[2020\]](#)).

As these orebodies are separated from each other spatially combined with the fact that the geological measurements show a very heterogeneous content of minerals in the mining area ([Boliden \[2019\]](#)), it is possible that different deformation results are obtained. Therefore, it is important to analyze the reliability of the results in different areas, as the underground tunneling environment at Kristineberg shows a complex geology throughout the entire mine.

3.3 GEOTECHNICAL CONDITIONS

The mine deposits that have been investigated in this study are composed of several ore lenses, as explained before. Those lenses are accessed through drill-and-blast and cut-and-fill methods. The geometry of a typical tunnel is shown in [Figure 3.9](#).

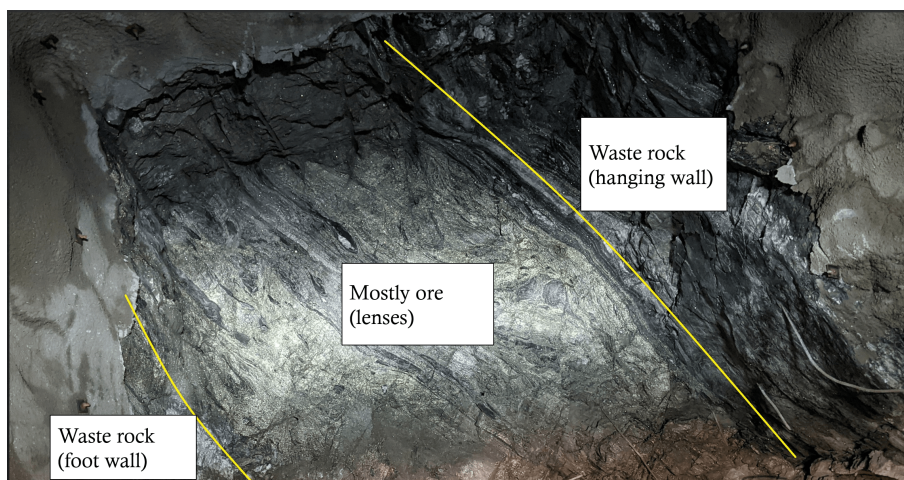


Figure 3.9: Figure illustrating the geological setting in the face of KK2 on the 28th of April.

The figure illustrates that for example in KK2, the hanging wall is located on the right side of the tunnel. As mentioned in section [Tunnel wall convergence studies](#), the hanging wall is pushing down on the foot wall, potentially leading to a stronger deformation in the right wall compared to the left wall, which is also found in earlier studies ([Boliden \[2019\]](#)). The deformation that has been observed before in the Kristineberg mine consists of two major types: blast-induced deformation and long-term deformation.

Additionally, the ore lenses vary in size from 1 to 7 m, as described earlier in this chapter. This variation in size leads to high heterogeneity of the rock mass when progressing in the tunnel. This high level of heterogeneity can and has led to stability issues in the past ([Boliden \[2020\]](#)), such as wedge failure of the rock mass and rock falling down.

The waste rock generally consists of relatively weak minerals, that are soft and easy to break. The minerals such as quartz or muscovite have shown to cause weak zones that are the first to break in case of tunnel wall deformation. This is especially the case if the quartz occurs as veins that dissect other waste rock structures ([Boliden \[2019\]](#)). Even the host rock, chlorite schist, cracks severely as results of blasting. This can lead to strong tunnel wall deformation and eventually stability issues.

The blast-induced deformation that has previously been observed in the Kristineberg mine consists of strong movement of the rock mass shortly after a blast, up to a maximum of 7 days. A possible explanation for this could be that the rock mass needs to find a new stable equilibrium position and the stresses acting within the rock have to be balanced out ([Fekete and Diederichs \[2013\]](#)). This phenomenon has been studied and will be elaborated on in section 6. The long-term deformation shows the deformational behavior of the rock over a longer period of time (> 7 days). By analyzing the movement of the rock mass over such a longer period of time, it becomes more clear whether a blast induced the deformation or if it is long-term deformation and if the rock reaches an equilibrium state again. Additionally, it is possible to study the behavior of the newly formed tunnel and predict potential failure zones, increasing worker safety and allows for faster response to secure tunnel stability ([Assali et al. \[2016\]](#)).

This chapter covers the types of sensor technologies used for this study. Then, the gathering of the data is described, followed by a description of the workflow for the data processing. In the last sections this chapter focuses on the data modelling and how the data has been analyzed.

4.1 SENSOR TECHNOLOGIES

3D **LiDAR** scanning is a remote sensing method that uses light in the form of a pulsed laser to measure ranges and the intensity of the reflection. A laser beam was emitted towards an object and the then returning beam was collected by sensors within the **LiDAR** scanner. Differences in i.e. return times and wavelength provide information about the object of interest and provide the means for creating a 3D digital representation of the object. The **LiDAR** technology can map features of an object or environment as a point cloud that appear as solid physical objects on first sight (Fekete and Diederichs [2013] and GroundProbe [2021b]).

The time of the flight of the laser in combination with the known speed was used to determine this distance. The **LiDAR** laser scanner combines millions of individual measurements in a relatively short period of time (generally several minutes) to obtain a 3D model of the target area. This type of scanner covers entire surfaces and does not necessarily require so-called targets to collect reliable data. The 'targets' mentioned in this thesis refer to either prisms or reflectors, or a combination of the two. This monitoring method is applied to ensure safety, long-term stability and quality control of the tunneling operation at hand. The use of high-definition laser scanning in the underground environment shows great potential. Scanners using the **LiDAR** technology use their own light signal, such that no external lighting is required to collect high quality data (Walton et al. [2018]). A number of advantages thus come with this new technology, namely:

1. Fast acquisition of high amounts of data
2. 3D modelling of detailed visualizations
3. Possibility for data acquisition from a distance (even from surface level), which leads to safer working conditions
4. No external lighting is required, this is a huge advantage in underground environments
5. It is easier to spot discontinuities on a **LiDAR** image compared to an **RGB** image

However, the technology also has its disadvantages, which are highlighted here:

1. Installation of targets was required to achieve high accuracy levels
2. Targets were used to position the scanner itself in 3D, but it is not always clear if the position of the targets varies over time
3. A zero-reading of a certain area of the tunnel can only be made as soon as the rock is exposed
4. Occlusion of the laser beam can lead to loss of data on the area behind the rock or mining equipment that causes the occlusion
5. Mining activities such as scaling or addition of shotcrete make the results hard to interpret if not known by the person
6. Occlusion or other reasons limiting the data can lead to misinterpretation of geological features

Additional to **LiDAR** technology, collection of **RGB** data was used in this study. This technology is based on the use of **RGB** cameras that provide images within the visible range of the electromagnetic spectra. The benefits of this technology are the wide availability, the absence of sample preparation requirement and the fact that it can be used in-situ fairly easily. A regular smartphone has the ability to capture such **RGB** images and to rapidly process the outcome.

The **RGB** images are stored in the 3 color bands: Red, Green and Blue with values that range from 0 to 255. As a result of each pixel having a specific Red, Green and Blue value, it is possible to classify the data and cross-reference this **RGB** data with the **LiDAR** data. The technology can be directly applied in color detection or indirectly for shape recognition of geological units (Desta and Buxton [2018]). The biggest shortcoming of the **RGB** image technology in the underground environment is the requirement of adequate lighting, which is not always readily available, especially in freshly blasted tunnel areas.

4.1.1 Instrumentation

In order to conduct these measurements, the [GML LiDAR](#) system from GroundProbe has been used. This device combines 3D [LiDAR](#) scanning with Slope Stability Radar ([SSR](#)) signal processing. The [SSR](#) monitors the entire surface of a slope, or in underground measurements the wall, and also works without targets. The [GML](#) is shown to have an accuracy of ± 0.4 mm during continuous measurements ([GroundProbe \[2021a\]](#)). Several accuracy measurements to analyze the accuracy of the equipment when using a tripod are described in this report. The [GML](#) is able to provide data in almost real time. The data obtained through this device is unaffected by metal objects such as machinery, bolts and mesh. The processing of the [SSR](#) signal removes the issue of the split beams and low point repeatability.

4.2 DATA GATHERING METHODS

4.2.1 LiDAR data gathering

This report focuses on the implementation of the GroundProbe [GML](#) equipment in order to measure the displacement and likelihood of displacement in the Kristineberg tunnel system. By comparing subsequent time-separated [PCD](#) sets, the deformation of the rockmass can be visualized. In order to obtain the absolute displacement at specific locations, georeferencing is applied to the targets used in the measurements. "The advantage of absolute positioning when recording deformations is that translations of individual tunnels due to nearby excavation activities can be recorded; in contrast, only closure measurements can be obtained when using relative positioning." ([Walton et al. \[2018\]](#)). The idea of georeferencing is that the measurements are recorded in a working software, i.e. MicroStation, and can thus be used to analyze the stability of individual tunnels due to the nearby excavations.

Additionally to the displacement measurements, the [PCD](#) that is generated is integrated with the geological interpretation of the faces after subsequent blasts. The resulting 3D model includes a hazard heatmap of the obtained data. Finally, the [GML](#) measurement technique is compared to conventional measurement techniques to analyze the accuracy of the data.

4.2.2 RGB imaging

Next to the [LiDAR](#) sensor technology [RGB](#) images were collected in this research. The [RGB](#) images were collected by use of a regular smartphone camera, in this case a Google Pixel 3XL. The phone has a very standard smartphone camera of 12 MP and can be used in the underground environment. It must be noted that proper lighting is required to be able to analyze the 3 [RGB](#) color bands. The images were stored in the 3 color bands Red, Green and Blue with values that range from 0 to 255. As a result of each pixel having a specific Red, Green and Blue value, it is possible to classify the data and cross-reference this [RGB](#) data with the [LiDAR](#) data.

4.2.3 LiDAR Scan Settings

The parameters used with the GroundProbe [GML](#) are shown in [Table 4.1](#). These parameters have been determined to be the most suitable for underground laser measurement purposes ([GroundProbe \[2021b\]](#)), and were thus used throughout every measurement described in this thesis.

Table 4.1: GML scanner parameters.

Settings	Description
Resolution	6.3mm@10m
Scan Mode	Close
Pulse Select	Last
Periodic Monitoring Setup Error	+/-3mm
Convergence Measurement Accuracy	+/-0.4mm

The resolution is considered to be high resolution and is described as the points(/pixels) in the [PCD](#) being 6.3 mm apart from each other at a distance of 10 m, or $2 * 6.3 = 12.6$ mm apart from each other at 20 m distance etcetera. The scan mode is by default 'Close', as it offers the best quality data in underground environments with dark surfaces and low reflectivity (at most 9%) ([GroundProbe \[2021b\]](#)).

This scan mode is one of the four options: close, detail, low power and high speed. Close offers the best quality data in case low reflectivity rocks were present and the environment is dark, detail offers more detailed data in case the rock were slightly more reflective (18% reflection of the light), low power is a battery-saving mode that does not provide detailed datasets and high speed does not offer high quality but is very fast as the name suggests.

Pulse select then allows for selection between either the first or the last pulse, in case a beam is split up by an irregular surface as shown in [Figure 4.1](#). First pulse means that the first return of the surface measurement is collected while last pulse means that the last return of the surface measurement is collected.

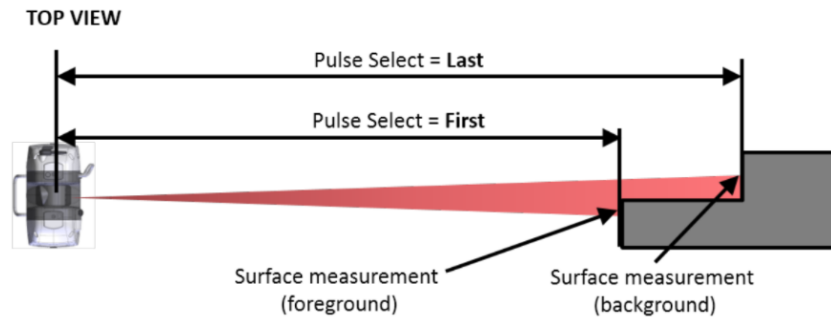


Figure 4.1: Illustration of the Pulse Select parameter (from [GroundProbe \[2021b\]](#)).

Furthermore, [Table 4.1](#) shows the error typically found in the data obtained from experiments with the GML, according to [GroundProbe \[2021b\]](#). The total error obtained when conducting the periodic measurements ranges from values between $-3 - 0.4 = -3.4$ mm up to $3 + 0.4 = 3.4$ mm. This means that if there were 3 scans, there can be a $3.4 + 3.4 = 6.8$ mm error between scans, under the assumption that the worst-case scenario occurred. This is a precision limitation of the equipment that was taken into account when analyzing the data.

5 | METHODOLOGY

This chapter focuses on the methodology regarding the data acquisition, the (pre-)processing of the data, the modelling of the data and finally the validation of the models.

5.1 DATA ACQUISITION

In order to provide a more detailed overview, [Table 5.1](#) shows where and how much data was gathered for this study.

Table 5.1: Size of the acquired dataset.

	L62H	KK2	KK3	Size [GB]
Tape extensometer	-	18	6	0.05
Survey measurements	12	-	-	0.05
RGB images	-	24	-	0.12
LiDAR data (geological)	-	12	-	6.0
LiDAR data (deformational)	16	15	6	55.5

Deformational measurements

Each underground scan in a new so-called ‘room’ is conducted following the same procedure. An initial scan is conducted from the corner of the room that connects the room with the access drift, where the targets can be installed in a presumably stable environment. From the data of the initial scan, stable locations for new prisms for subsequent scan locations were determined. Then, as each blast advances the room 3 to 5m, a new scan location is initiated after approximately 15 – 20m in order to get a new zero-reading of that region. This process is continued until the room is finished. This is illustrated in [Figure 5.1](#).

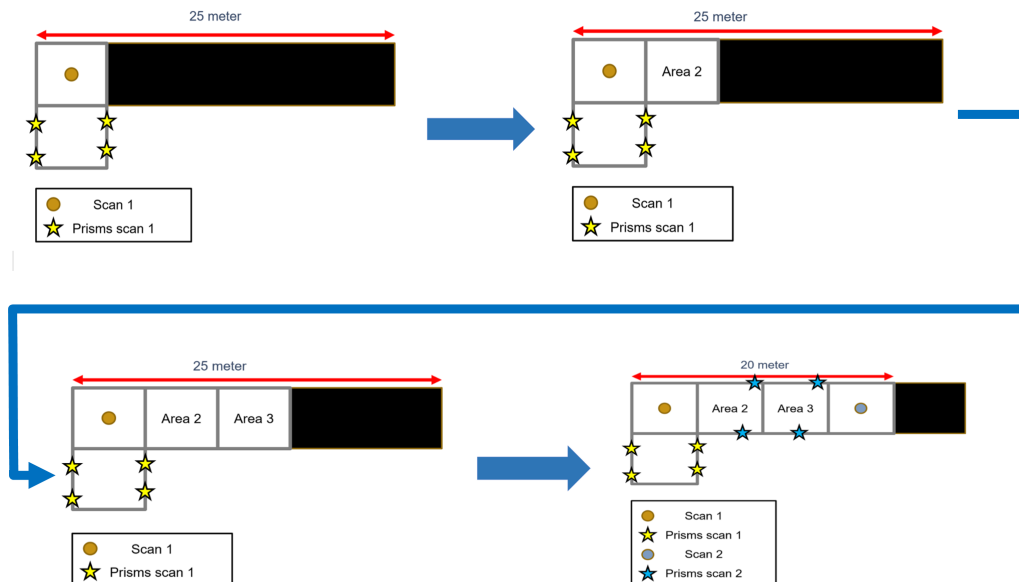


Figure 5.1: Progression of scan and prism locations.

However, an important downside of this must be noted. The zero-reading of a new area along with the corresponding geological scan can only occur as soon as the previous area of the tunnel has been blasted. Therefore it is difficult to obtain an understanding of the correlation between the lithologies and geological circumstances and the long-term deformation in each section of the tunnel. The underground measurements were conducted in three rooms, namely L62-H, KK2 and KK3.

After a deformation measurement and geological mapping has been finished, the shotcrete is applied and a successive blast is conducted. The newly visible fresh rock is measured again, as shown in Figure 5.2 and this procedure is repeated. The structural geology along with the lithological structures obtained from the acquired LiDAR data can then be linked to the displacement of the rock, in order to get a more thorough understanding of what the root cause of the displacement is.

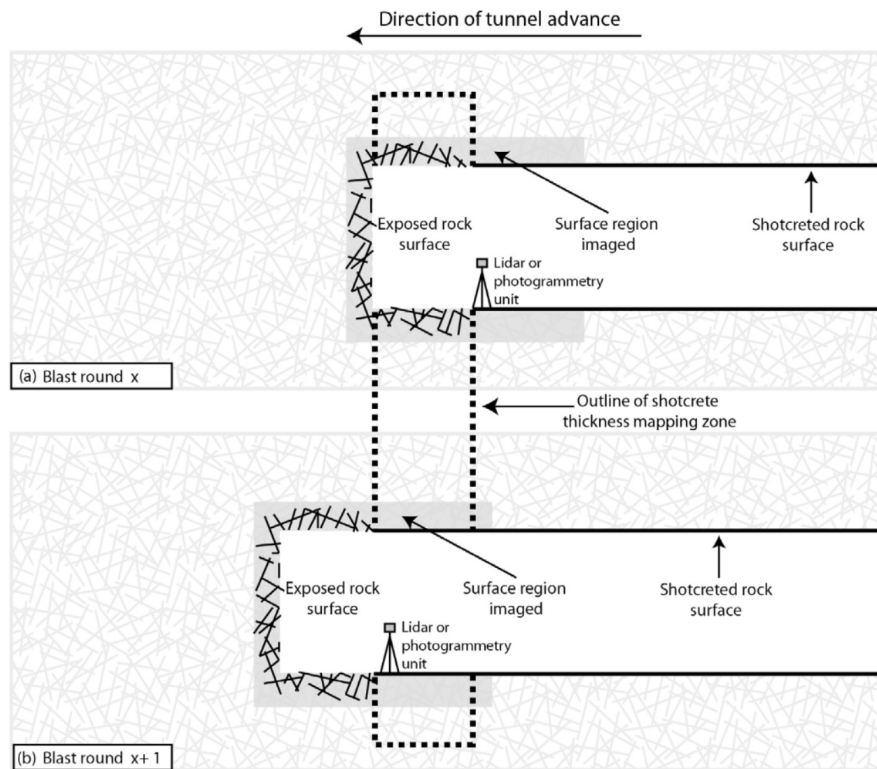


Figure 5.2: Illustration of how the LiDAR scans from the exposed rock surfaces were taken. (Lato and Diederichs [2014]).

5.1.1 Room L62-Höger

Initially, a number of measurements have been carried out in room L62-HÖGER. The locations of these scans are shown in Figure 5.3. The coding of the scans was done according to the room measured (L62H), followed by the number of the scan (1).

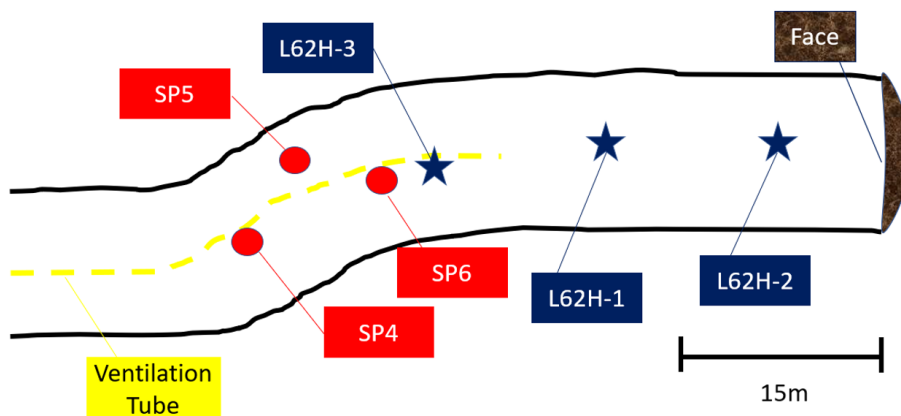


Figure 5.3: Location of the measurements in room L62-HÖGER.

In order to obtain a better understanding of how accurate the results of the scans with the GML are, the total deformation and the daily movement in the rock mass have been compared to the measurements conducted by the Boliden surveyor team by using a Leica TotalStation (as explained in subsection [Total Station](#)). This subsection has shown that the Leica TotalStation provides accurate results (± 2.5 mm), but only for the specific points being measured.

This section consists of 4 measurement dates and the deformation between the subsequent scans. A total of 4 scans were analyzed for both the total deformation (in mm) as well as the deformation rate (in mm/day). The workflow in this room consisted of:

1. Boliden surveyor team measured with TotalStation
2. Measurements were conducted with the LiDAR scanner
3. Comparison of TotalStation vs. LiDAR scanner results

Where the comparison is made between 3 different GML scan positions with respect to 3 survey points (SP's), as shown in [Figure 5.3](#). It must be noted that some of the scan locations have difficulty to view all of the survey points properly, either due to the angle with respect to the tunnel wall, or by (partial) blocking of the survey point by the ventilation tube. This is part of the research, to analyze if it matters at which angle the LiDAR scanner is still able to provide accurate results. The reason behind this is that sometimes due to time limitation or blocking of the room, the scanner is not being put in the most ideal situation. Therefore, it is important to analyze if the equipment is still capable of producing accurate results in such a situation.

5.1.2 Room KK2

The second room of interest is called KK2 (Kopparklumpen 2). The locations of the conducted scans are shown in [Figure 5.4](#). Again, the coding of the scans was done according to the room measured (KK2), followed by the number of the scan (1). Additionally to the convergence scans, geological scans have been conducted. Initially, the room progressed in the right direction.

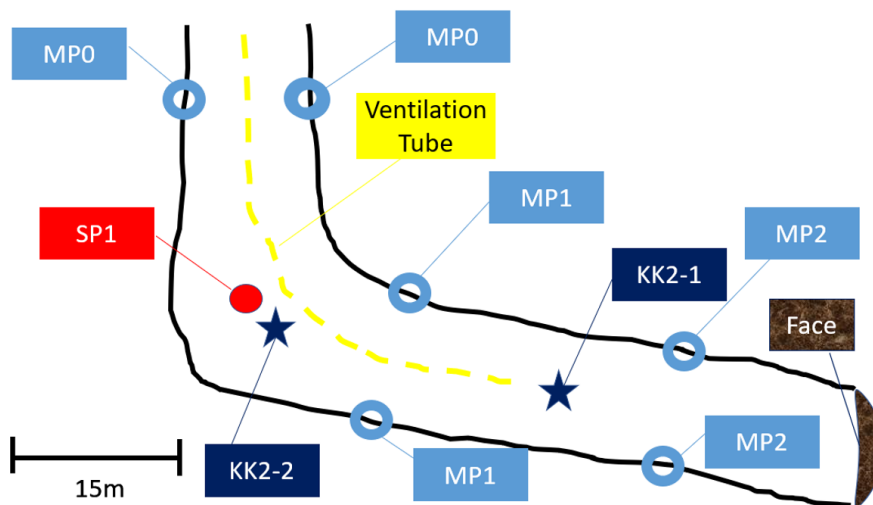


Figure 5.4: Location of the measurements in room KK2 (initial).

Initially, the room progressed in the right direction. At a later stage, the right side of the room was used as temporary waste rock storage, while a new face was blasted on the left side of the tunnel. This final stage is shown in [Figure 5.5](#).

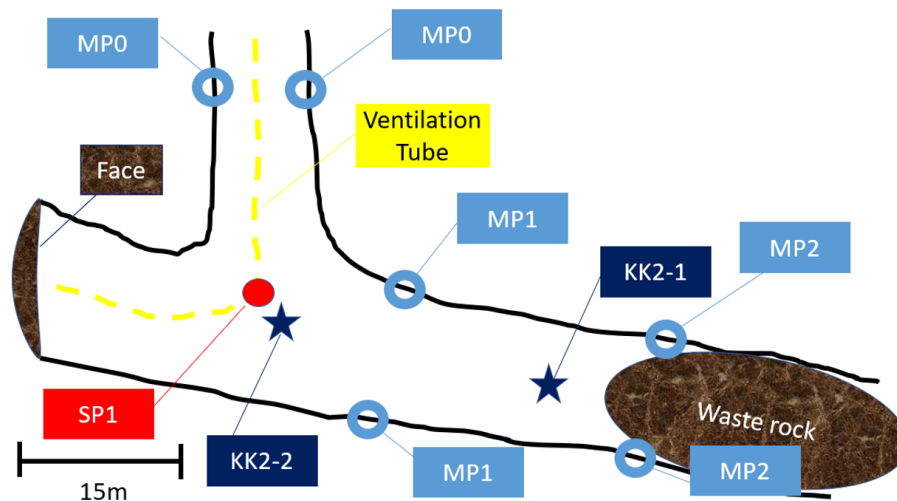


Figure 5.5: Location of the measurements in room KK2 (final).

In order to collect the data regarding the geological structure and the lithology of the area of interest, the fresh rock was measured straight after a blast. This can lead to a more thorough understanding of the deformations, as suggested in Fekete et al. [2010]. There was a specific time window in which the data can be acquired, generally shortly after mucking and scaling and before the shotcrete was applied. After the measurement, the shotcrete was applied and a successive blast was conducted. The newly visible fresh rock was measured again, as shown in Figure 5.2 and this procedure was repeated. The structural geology along with the lithological structures obtained from the acquired LiDAR data can then be linked to the displacement of the rock, in order to get a more thorough understanding of what the root cause of the displacement is.

An overview of the collected data is presented in Figure 5.6 and in Figure 5.7. On the left side of the Kopparklumpen 2 (KK2) tunnel, data has been collected from 22/04 until 18/05. After this moment, this part of the tunnel was backfilled and no longer accessible for measurements. A total of 6 geology scans were taken from this left side of the tunnel, along with 6 deformation scans.

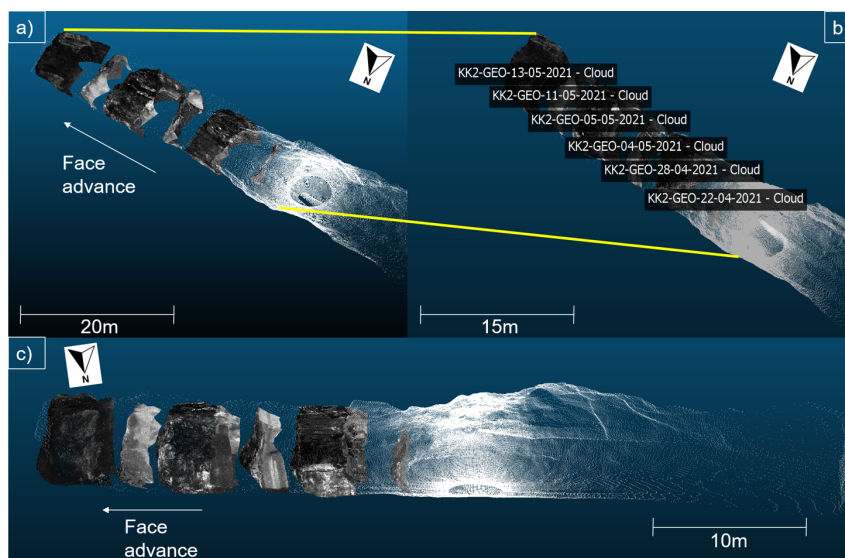


Figure 5.6: Overview of the locations of the exposed rock surface scans taken in the left side of KK2.

As shown in Figure 5.7, a total of 6 geology scans have been taken from the right side of the tunnel as well. As this location for the deformation scans (KK2-2) has been accessible since the beginning of this experiment, a total of 11 deformation scans were taken from this side of the tunnel, including the time before this face was opened up. This means data has been gathered on this location from 22/04 until 18/06. Therefore, this side of the tunnel has more potential to give a better understanding of the long-term deformation reaction after several blast cycles. Though it should also be mentioned that because this face was not open from the very beginning, it was more difficult to analyze what impact the different geological structures in this area have had on the long-term deformation that occurred since the very beginning of the measurements.

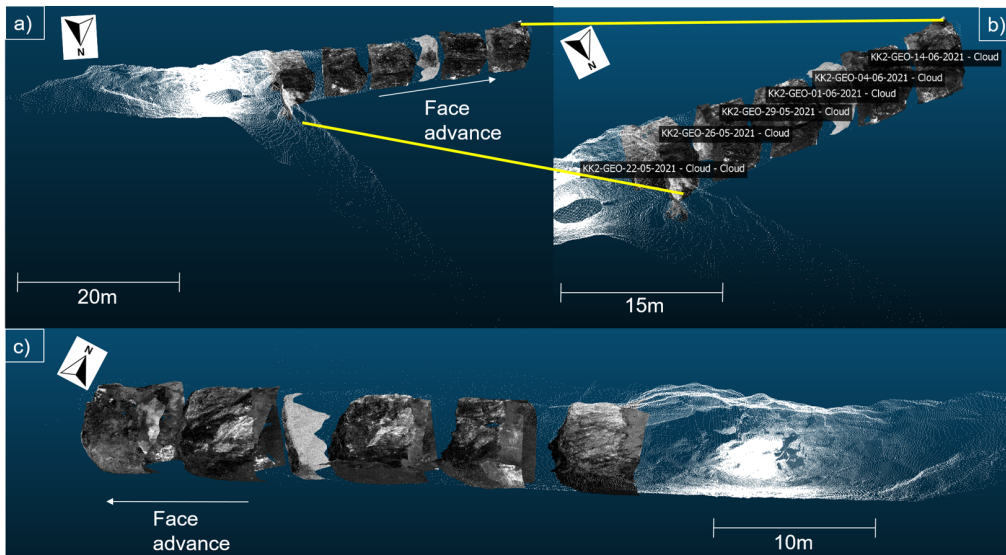


Figure 5.7: Overview of the locations of the exposed rock surface scans taken in the right side of KK2.

Geological mapping

The LiDAR scan of the exposed rock surface was then visualized based on the varying intensity levels, in order to distinguish different litho-types. The intensity was normalized between 0 and 1 for easier handling of the data. In Figure 5.8 can be seen that there is a clear distinction between different areas of the exposed rock surface. For example, in the bottom of the centre there was a high intensity (dark red) and when comparing this to Figure 5.17, this was the area where most of the minerals associated with copper ore were found. In contrast, the waste rock seems to exhibit a much lower intensity when looking at the central area of the face and the surroundings.

3D Heatmap based on intensity levels for LiDAR geology scan 28/04/2021

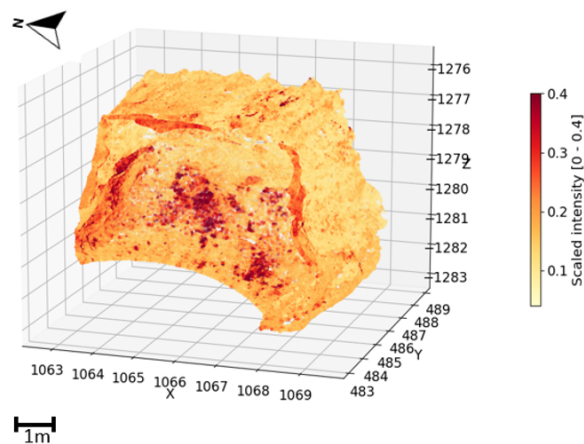


Figure 5.8: LiDAR intensity data obtained from the fresh rock surface in KK2 on the 28th of April.

Additionally, the LiDAR scans have been analyzed in Maptek's PointStudio software. This was done through the use of the X, Y and Z coordinates of the pixels and their corresponding normal vectors. Pixels with similar normal vector orientations were then grouped together and were shown as one structure. This will be discussed in the next subsection.

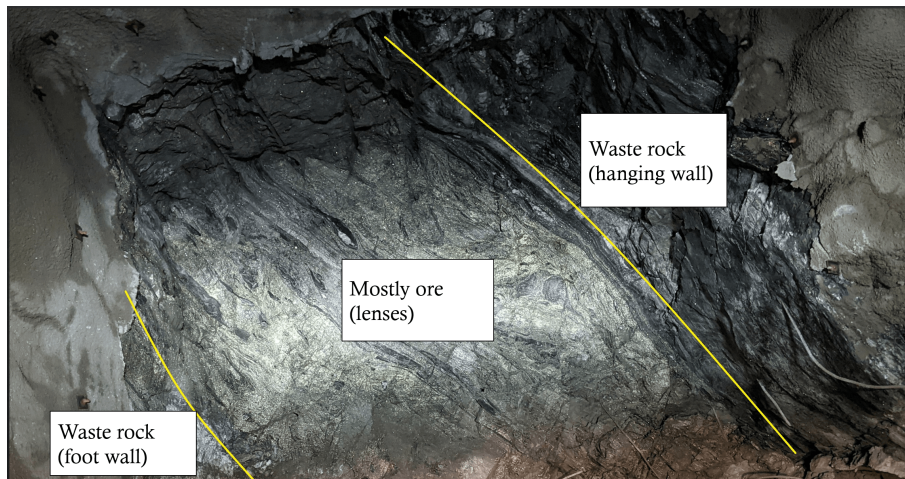


Figure 5.9: Figure illustrating the geological setting in the face of KK2 on the 28th of April.

As shown in [Figure 5.9](#), the hanging wall was located on the right side of the tunnel. As mentioned before in section [Tunnel wall convergence studies](#), the hanging wall is pushing down on the foot wall, potentially leading to a stronger deformation in the right wall compared to the left wall, which was also observed in [Figure 6.71](#).

Continuous Measurement KK2

Finally, an experiment was performed where the scanner was left in the room right after a blast to scan every 20 minutes for a total of 6 hours overnight. This experiment was done to get a more thorough understanding of the measurements with and without a repositioning error and to visualize the movement in the fresh rock face right after a blast. A total of 17 scans have been collected during this experiment and will be discussed in this section.



Figure 5.10: Set-up of the continuous measurement experiment.

The set-up used during the continuous measurements is shown in [Figure 5.10](#). The tripod was installed on the right side of the tunnel, where the face advances. The face has been blasted during the shift before the GML was put into position. The rest of the tunnel was covered in shotcrete. On the other end of the tunnel, the left side, waste rock is stored to stabilize the tunnel and to save time removing the material. A sketch of the set-up is illustrated in [Figure 5.11](#).

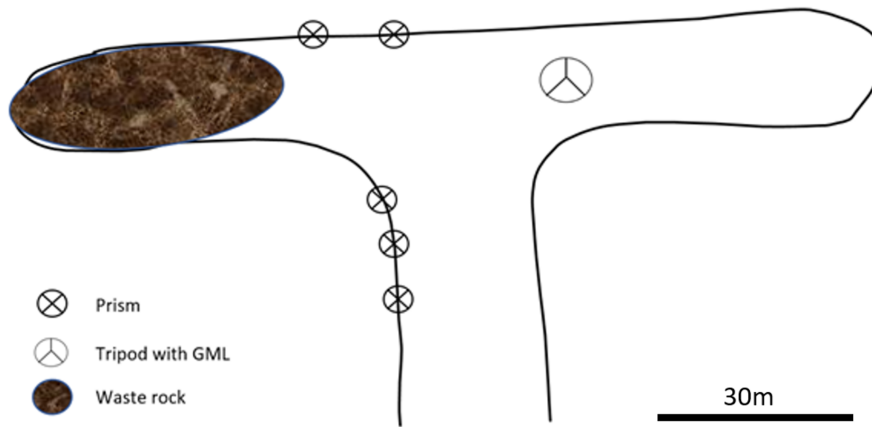


Figure 5.11: Sketch of the set-up of the continuous measurement experiment.

A total of 5 prisms have been installed for this measurement, because the prisms give the most accurate results when conducting a [LiDAR](#) scan ([Contogianni et al. \[2007\]](#)). 3 of the prisms were located in the access drift, which was presumed to be stable. This was also confirmed by earlier tape extensometer measurements. Additionally, 2 prisms were installed inside the tunnel itself. This was done in order to see the effect of a potential movement of the prisms.

An [RGB](#) image was taken from the face before conducting the continuous scans. The fresh rock can be seen in [Figure 5.12](#). Typically, the ore was seen in the centre of the face, which will be discussed in more detail. Then on both sides of the ore, waste rock was found. The waste rock consists of chlorite schist, cerussite, quartz and for example biotite. The ore was found in lenses, which has been discussed in section [3.1](#).



Figure 5.12: An RGB image of the face scanned during the continuous measurements.

5.1.3 Room KK3

The last room that has been measured was Kopparklumpen 3 (KK₃). The same procedure of the coding of the scans was used in this room. Due to heavy mining activity that blocked (part of) the room, only one scan location has been measured. In KK₃ tape extensometer measurements have been collected additional to the scans with the GML in order to analyze the accuracy of the deformation scans.

Figure 5.13 illustrates the development of the room during the measurement period. Initially, the face was on the left side (Figure 5.13a), but as this side was depleted after some time, a new face was opened on the right side (Figure 5.13b) and the old left tunnel has been used as temporary waste rock dump. This similar sequence was observed in room KK₂ before.

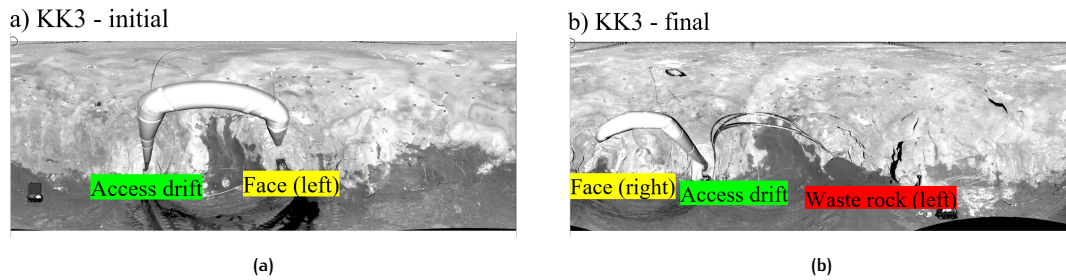


Figure 5.13: LiDAR greyscale images illustrating the layout of room KK₃. (a) Room KK₃ in the beginning of the experiment (b) Room KK₃ at the end of the experiment.

The gathering of the data consists of:

1. Tape extensometer measurements
2. LiDAR deformation scanning
3. Processing and analyzing the data

During the analysis the 2 measurement points were compared against the LiDAR deformation data. The processing of the LiDAR data was done both with the raw data as well as the automatically aligned data before comparison.

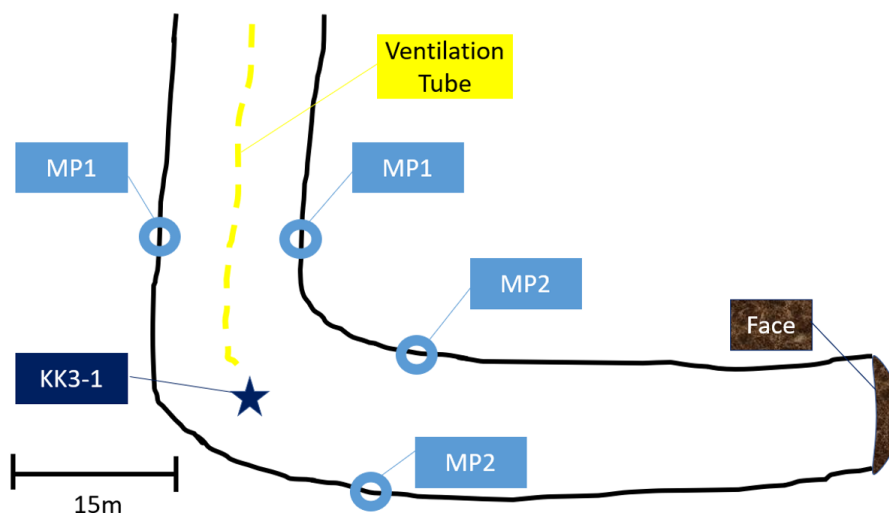


Figure 5.14: The initial layout of KK₃.

The layout of the room KK₃ with the corresponding measurement points is shown in Figure 5.14. As the rest of the tunnel was commonly blocked by mining equipment, there was only one scan location, KK3-1, where both the access drift and the actively mined tunnel were clearly visible.

5.2 DATA PRE-PROCESSING

This section covers the pre-processing of the acquired data. All the collected data has been pre-processed before it has been used to study in further detail. The subsections below describe how this has been done.

LiDAR Data Pre-processing

The raw data collected from both the **GML** has been pre-processed before being analyzed. The data of the **GML** can be divided into two subcategories, namely geological **LiDAR** data and **LiDAR** deformation data. The **LiDAR** deformation data has been georeferenced by using the coordinates of the reflectors attached to the bolts in each of the tunnels or by aligning the point cloud with existing 3D models that were already registered to the mine grid coordinate system introduced in [Figure 3.8](#). Then, the **LiDAR** data of subsequent deformation scans has been processed by using the **SSRViewer** software in order to analyze the deformation zones.

The initial georeferencing of the geological scans was done based on the use of reflectors, and later fine-tuned based on distance from the face and by aligning the point clouds with existing 3D models from the mine system. Therefore, there can be a small offset in the geological scan locations. However, when visualizing the geological scans on top of the deformation scans, the offset has shown to be small (within the range of 5cm at most).

RGB Data Pre-processing

The **RGB** data has been passed through a high-pass (sharpening) filter, in order to accentuate the comparative differences in **RGB** values with neighbouring areas. The high-pass filter uses a weighted kernel neighborhood algorithm to calculate a focal sum statistic of each cell and this allows for a visualization of the boundaries between different features, thus sharpening edges. Additionally, the **RGB** images quite often showed the light coming from the flashlight that led to too much light on some areas of the images. This has been reduced by reducing the contrast of the images, to get a more uniform picture.

5.3 DATA PROCESSING WORKFLOW

This section focuses on the general workflow that has been used throughout this study. An illustrative sketch is shown in [Figure 5.15](#) and explains how all data for this study was gathered and processed.

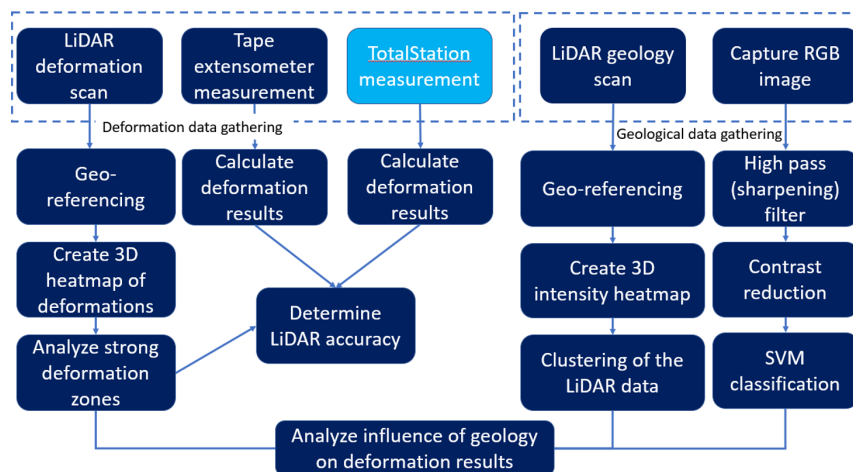


Figure 5.15: Sketch of general workflow.

In light blue, the total station measurements, were carried out by the surveyor team of Boliden. All the other measurements have been carried out by the author of this study. The handling of the data is explained in more detail in this chapter.

5.4 DATA MODELING TECHNIQUES

LiDAR Data Modeling

To analyze the different data sets, the data has been processed and visualized. At first, a visualization of the geological scans in combination with the deformation scan (in greyscale, to show the whole tunnel area) has been collected to be able to see the spatial distribution of the subsequent geological scans.

Then, the LiDAR deformation data has been separated into two deformation stages, namely blast-induced (short-term) deformation and long-term deformation. The blast-induced deformation shows a very strong deformation closest to the face, as illustrated before in Figure 2.1b. However, when looking at the long-term deformation, it was expected that the strongest deformation can be found further away from the face, as can also be derived from Figure 2.1b.

Thirdly, the geological LiDAR data was analyzed in Python. The intensity data obtained by scanning the exposed rock surface with the LiDAR scanner has been processed by use of the K-means algorithm. As mentioned in Clayman et al. [2020]: "Dimensionality reduction methods, such as K-means clustering, are used to capture essential elements and explain larger data sets using a subset of relevant features." The algorithm does so by computing the distance between samples and forms clusters by representing the intensity values as a vector of expression values, therefore, this method is computationally intensive. Dimensionality reduction is necessary in order for the algorithm to be efficient. The K-means clustering was performed on each of the individual LiDAR scans of the exposed rock surfaces.

One of the most difficult parts about implementing the K-means algorithm, was the choice of the number of clusters beforehand (Fard et al. [2020]). Therefore, the elbow method has been implemented in this study. The elbow method was based on the Within Cluster Sum of Squares (WCSS) (also known as the variation) and consists of plotting this sum as a function of the number of clusters. The elbow of the curve was then used to determine the number of clusters to be used. The WCSS is explained by the following equation:

$$WCSS = \sum_{i=1}^k (X_i - C_i)^2 \quad (5.1)$$

In Equation 5.1, C_i is the centre of the i -th cluster and X_i is the location of the i -th point. After analyzing the elbow plot of individual LiDAR data sets, it became apparent that a total of 3 clusters was the optimal number of clusters. An example of such an elbow plot is shown in Figure 5.16, from which can be seen that the 'elbow point' occurs at 3 to 4 clusters. After some trial runs, it was determined that 3 clusters gives the most optimal results for the data set of this study.

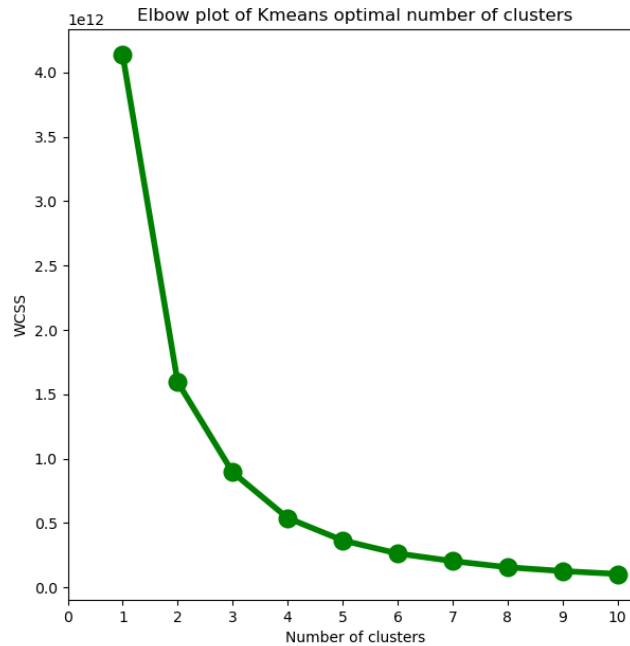


Figure 5.16: Elbow plot of geological LiDAR data 28/04/2021.

In order to compare the K-means results to a different type of clustering, the two-phased clustering method has also been implemented on this dataset. This process involves K-means with a large number of clusters in the first phase, the square root of the number of observations but always between 100 and 200 clusters at most. The second phase then consists of hierarchical clustering which is believed to be more varied and more precise (Mueller and Massaron [2019]).

The Python analysis was conducted by the following steps:

1. Visualization of the 3D Point Cloud
2. Elbow plot of the optimal number of clusters for the data set
3. Number of elements per K-means cluster
4. Number of elements per two-phase cluster
5. Intensity ranges within clusters for both clustering methods
6. Visualization of the 3D intensity heatmap
7. Comparison of both clustering results (with scaled intensity)
8. Visualization of the Kernel Density Estimate (KDE) result

The KDE was implemented in the final stage to visualize the pixel density of the data set. Typically, a Gaussian kernel was used in this algorithm, as mentioned in Vestal et al. [2021]. The Gaussian kernel has been used for this study as well. As explained before, the resolution has been set such that the pixels have a spacing between each other of 6.3 mm at a 10 m distance. This would mean that pixels closer to the scanner would typically have a larger KDE value.

RGB Data Modeling

From the fresh rock surface, an RGB image was taken along with a LiDAR scan to analyze the (structural) geology of the exposed rock. The RGB images were classified based on the SVM algorithm. SVM consists of a supervised machine learning algorithm that is mostly applied in pattern recognition and in image processing for recognition. SVM has been used in order to analyze the RGB images because it generally performs better than other network traffic classifiers in terms of the generalization of a problem (Pradhan [2012]) and because it allows for the handling of non-linear classifications of data sets (Desta and Buxton [2018]). An example of such an RGB image is shown in Figure 5.17.



Figure 5.17: RGB image captured from the exposed rock surface on the 28th of April in KK2.

In order to obtain an SVM classification result, the algorithm was pre-trained on the RGB image first. The labels used to classify the RGB image are the different litho-types present. The litho-types used for classification are:

1. Waste Rock (Code 1)
2. Copper Ore (Code 2)
3. Zinc Ore (Code 3)
4. Shotcrete (Code 4)
5. Shadow (i.e. in case of occlusion) (Code 5)

The process of training such an SVM classification is shown in Figure 5.18. In close cooperation with the geologists at Boliden, it was possible to distinguish between the different litho-types in the exposed rock surface image. A set of areas of each individual litho-type has been selected in order to train the SVM classifier.

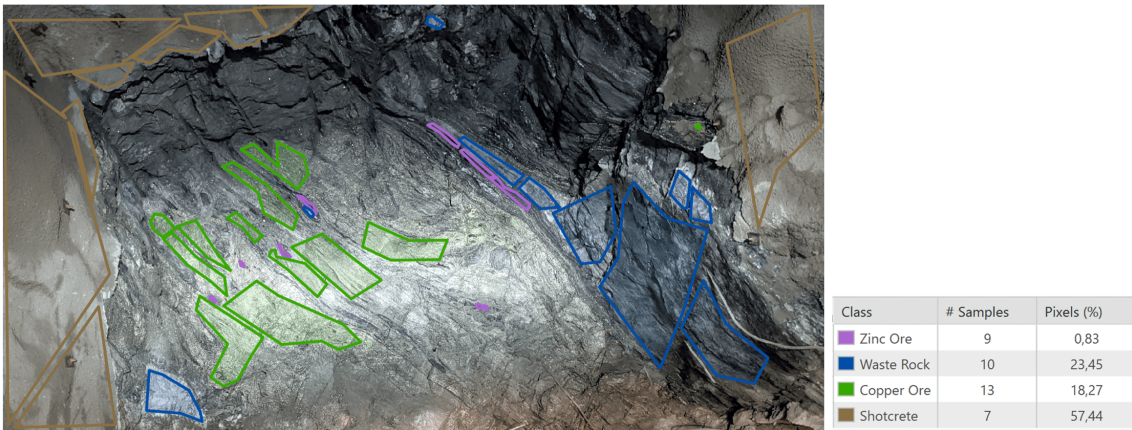


Figure 5.18: Training the SVM classifier on the RGB image captured from the exposed rock surface on the 28th of April in KK2.

The result of the classification is then shown in Figure 5.19. As can be seen by visual inspection, the algorithm has classified most of the rock as expected. However, it must be noted that for example the area in the bottom labeled as 'shotcrete', was incorrect. Also, the copper ore in the centre seems to extend further in height than what the classifier managed to identify. The results are discussed in more detail later in this report.

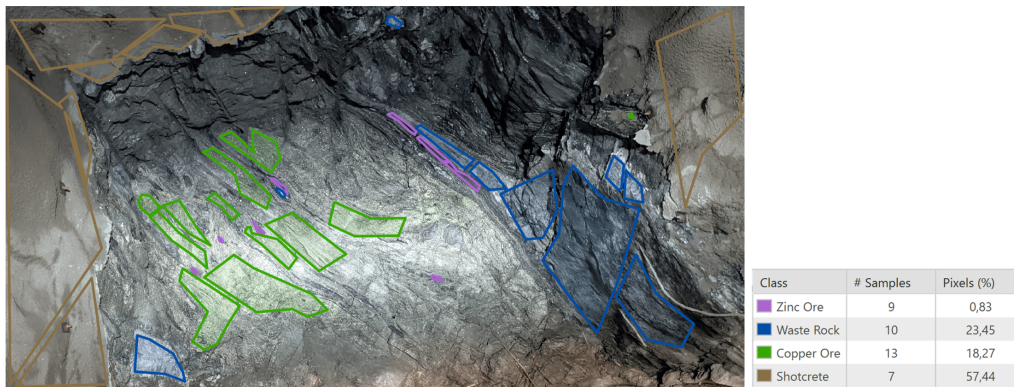


Figure 5.19: SVM Classification based on the RGB image captured from the exposed rock surface on the 28th of April in KK2.

5.5 VALIDATION

In order to validate the accuracy of the **GML** equipment, a number of experiments where the true displacement was controlled have been conducted. In the first accuracy experiment, experiment 1, the tripod with the **GML** scanner was set up and kept in position.

This experiment was conducted in two different settings, one in which prisms were used as targets and one in which reflectors were used as targets, experiment 1.1 and 1.2 respectively. This method allows for an accuracy validation of both the **GML** scanner itself as well as for the use of different targets. The subject of interest was a cardboard box. The true displacement was conducted by moving this cardboard box forward and was measured by using a conventional laser scanner (a Leica Disto D2). The accuracy of this Leica Disto D2 was ± 1.5 mm according to **GeoSystems** [2021]. The set-up of the experiment is illustrated in **Figure 5.20**.

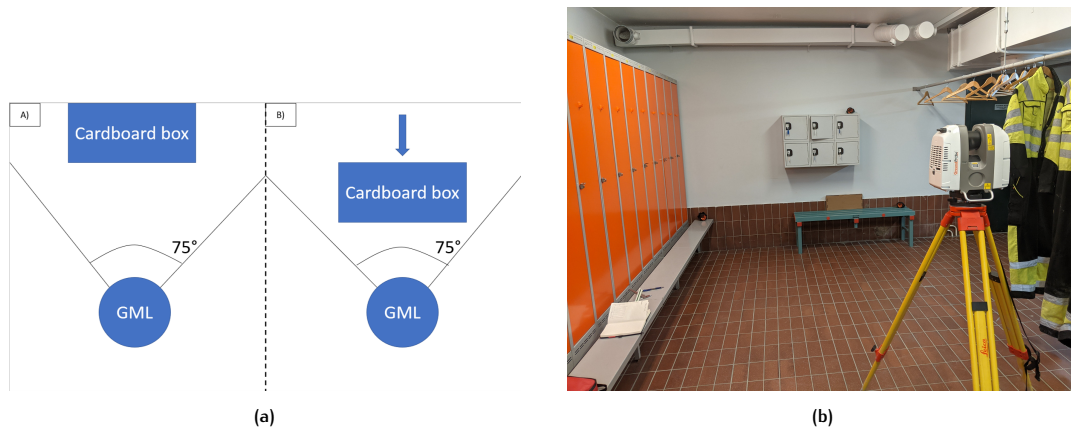


Figure 5.20: Accuracy measurements set-up. (a) Sketch of the measurement process (b) RGB image that shows the set-up.

A circle was drawn in the centre of the cardboard box and was defined as the area of interest. The (true) displacement was measured on the location of this circle. The true displacement obtained from the Leica DistoMeter was then compared to the displacement shown in the **GML** data. The **GML** data was visualized by using **GroundProbe's SSRViewer**, as shown in **Figure 5.21**.

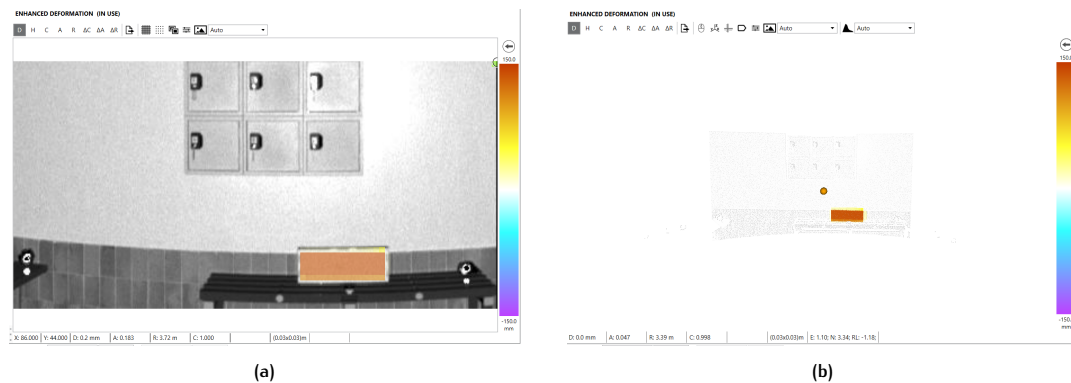


Figure 5.21: GML displacement data visualized in SSR-Viewer. (a) 2D image of the displacement (b) 3D image of the displacement.

For the second accuracy experiment, the same procedure was conducted. Additionally, the **GML** and the tripod were removed in between scans to determine the repositioning error of the equipment. Again, this second experiment was conducted in two different settings, the first one involves the use of prisms and the second one the use of reflectors, experiment 2.1 and 2.2 respectively.

5.5.1 Model validation

LiDAR Model Validation

The unsupervised LiDAR clustering methods performed in Python can be compared to the supervised RGB image analysis. By comparing these methods to each other, it was possible to cross-reference whether or not a clear distinction could be made between waste rock and different types of ore based on this data.

The raw data of the GML scanner was visualized as deformation data but it became clear that the repositioning of the scanner was sometimes causing issues with respect to the alignment of subsequent scan results. Therefore, the data was studied in 3 different settings to obtain a better understanding of this error. The first setting consists of the raw LiDAR data with no correction applied.

The second setting then consisted of the LiDAR data after applying a manual correction to the positioning of the subsequent scans. However, it must be noted that this process was very subjective and time-consuming. Additionally, there was a bias involved if the person correcting the data already has information about the deformation of the tunnel from for example the Total Station data.

Therefore, the manual correction applied during this study consists only of removing symmetrical errors and nothing else. An example of such a symmetrical error was when the roof shows significant negative deformation (showing that it has moved upwards several cm, which was not the case) and the floor showing positive deformation (showing that it moved upward with respect to the scanner as well). This can be a result of the tripod being at a different height in subsequent scan experiments. An example of a symmetrical error where one wall shows negative and the other wall positive deformation is shown in Figure 5.22.

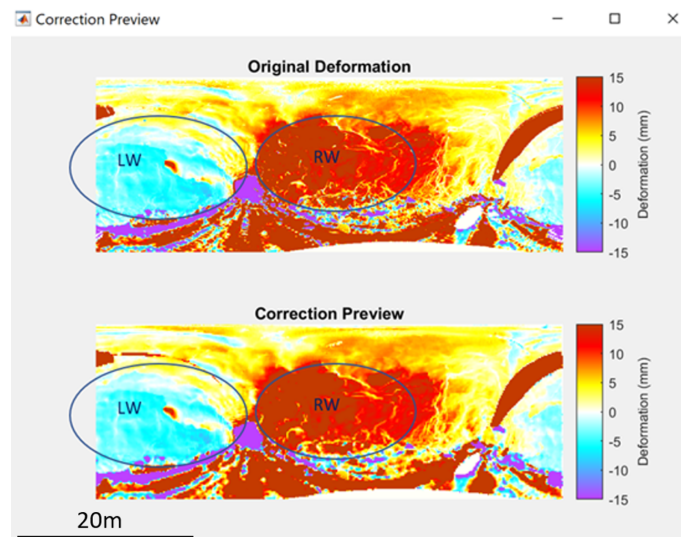


Figure 5.22: Snapshot of the scan correction window that shows the original deformation and a preview of the applied correction (in this case no correction so they are both the same). LW = Left wall, RW = Right wall.

The error shown in Figure 5.22 shows the symmetry in the two walls, as described before. In the left wall (LW), a negative movement can be seen of approximately -5 mm. This means in practice that the wall has moved away from the centre of the tunnel by 5 mm. The right wall (RW) shows a very strong positive deformation of 15 mm and higher. As there is symmetry in these two deformations, a manual correction can be applied to remove the physically impossible negative movement in the left wall. The correction thus consists of a small horizontal angular change. However, this correction can only be applied until the symmetrical error was removed, because the 'true movement' of the rock mass was unknown.

Finally, the last setting consists of applying the 'auto align' method provided by GroundProbe's data processing software GMLControl. This method consists of an algorithm that attempts to properly align subsequent scans based on their respective locations with respect to the targets used. This allows for the user to remove the subjective aspect of applying a correction to subsequent deformation scans. However, the auto align methodology does not always function optimally. Sometimes the algorithm does not manage to properly match the subsequent scan locations and the resulting deformation data shows very strange numbers (i.e. deformations of 20,000 mm in worst-case scenarios).

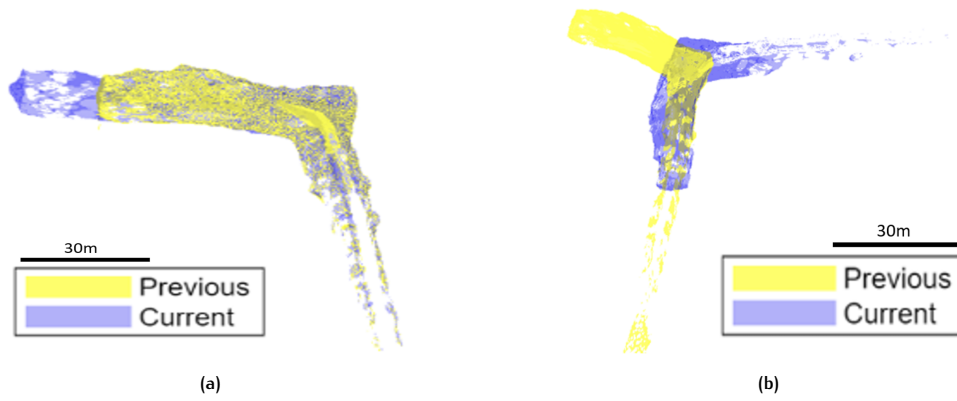


Figure 5.23: Example of automatically aligning subsequent LiDAR deformation scans of room KK2. (a) Properly aligned scans 1 and 2. (b) Misaligned scans 2 and 3.

An example of this alignment solution is shown in Figure 5.23, which shows scans from the KK2 room. In Figure 5.23a the algorithm managed to properly align subsequent scans 1 and 2. Then in Figure 5.23b the algorithm did not manage to properly align scan 2 and 3 and as seen from the visualization, the tunnel was completely rotated and off. However, in the case of properly aligning the tunnel, this data has been included in this study to get an overview of how this relates to conventional methods and raw data.

RGB Model Validation

For the RGB analysis it is important to realize that it was conducted based on visual inspection. As mentioned before in Section 5.4, visual inspection can be used to analyze whether or not the SVM algorithm performed well. Areas in the bottom of Figure 5.19 that were classified as shotcrete, clearly are not shotcreted when looking at the original RGB image. An explanation for this misclassification is that due to dust on the rock face leading to a slight brown color tone, the RGB values of those pixels are similar to those of the shotcreted walls.

Next to the visual inspection from the raw RGB image compared to the classified RGB image, it has also been compared to the unsupervised LiDAR classifications. From this inspection it can become clear how well the RGB image classification performs compared to the LiDAR classification results. This will be explained in more detail later in this report.

6 | RESULTS

6.1 LIDAR ACCURACY MEASUREMENTS

This section focuses on the analysis of the results of the two accuracy experiments that have been performed in order to assess the accuracy of the GroundProbe GML LiDAR scanner. The two experiments have been conducted in a controlled environment and the results are used to move forward during this study.

Experiment I results: controlled true displacement

The accuracy measurement results of the GML data have then been collected and analyzed. A total of 4 points that are within the circle on the box are selected and the corresponding displacement results are shown in Table A.1 and in Table A.2, for the use of prisms and the use of reflectors respectively. This process was repeated for each of the 10 measurements for both using prisms and reflectors. The measurement results of those 4 points are then averaged, and the true displacement that was measured with the Leica Disto D2 was subtracted to obtain the difference between the two. A comparison of the results between the use of prisms and the use of reflectors is shown in Figure 6.1.

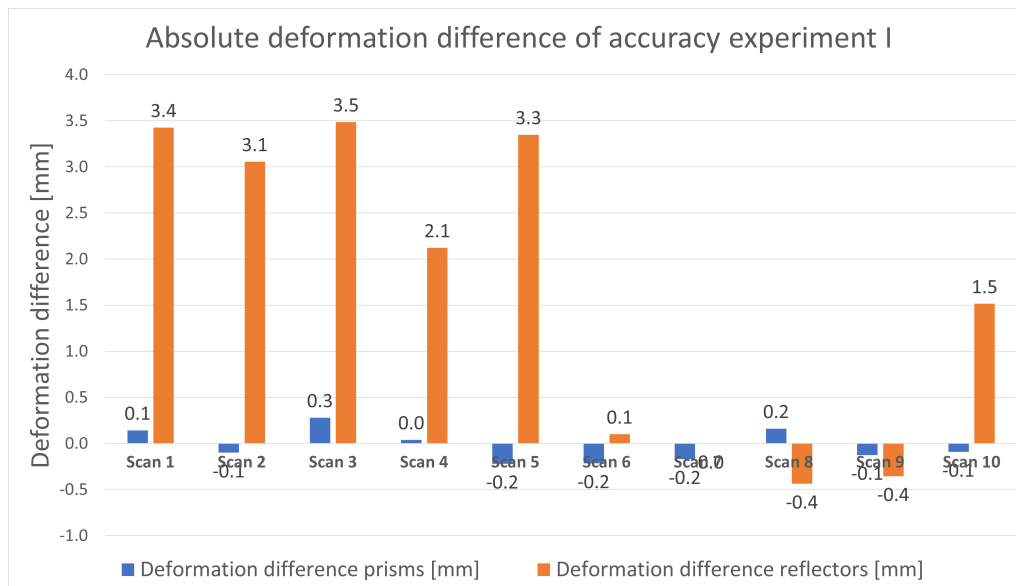


Figure 6.1: Accuracy measurement I absolute deformation results of the box with respect to the Leica Disto D2.

As can be seen in this figure, the difference between the Leica Disto D2 and the GML scanner results with the use of prisms is nearly zero. This means that the use of prisms was preferred in case a high level of accuracy was desired. The use of reflectors clearly shows a fairly high difference in terms of accuracy when compared to the prisms, with maxima in the range of 3 – 3.5 mm difference for some of the performed scans. The prisms show a difference of at most 0.279 mm when compared to conventional measurement tools. This measurement thus supports the theory that the reflectors are lower in accuracy than prisms, as described in section GroundProbe GML.

However, it must be noted that reflectors can still have a useful application when performing a scan in an underground mining environment. One of the benefits of using reflectors was that they can be attached to georeferenced bolts in a tunnel. This results in less time consumed to georeference the targets by the surveyor team. The trade-off in this decision comes down to accuracy versus time, which both can be very valuable in an active mining environment. To illustrate the relevance of the differences between the different targets, the differences have been determined in % compared to the true displacement and those results are shown in Figure 6.2.

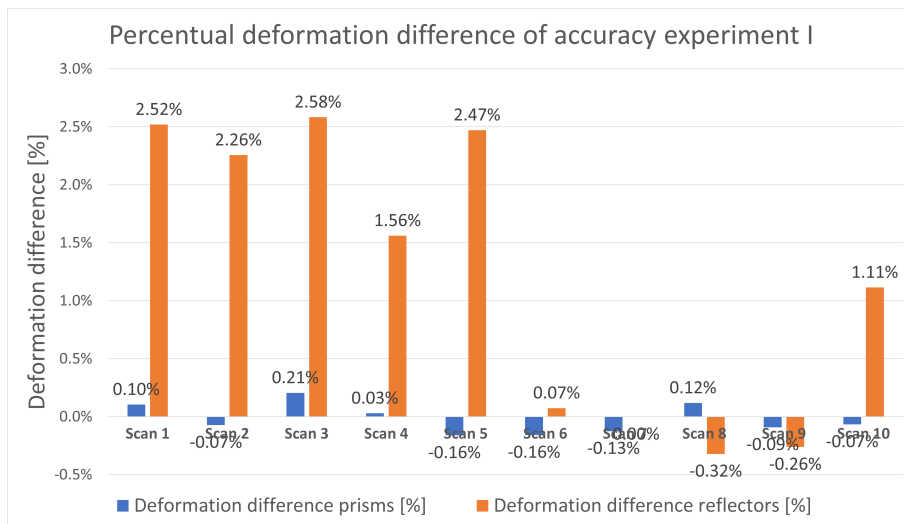


Figure 6.2: Accuracy measurement I percentual deformation results of the box with respect to the Leica Disto D2.

Figure 6.2 shows the relevance of the difference with the use of different targets. In the measurements that have been conducted with reflectors only, there was clearly a much bigger accuracy error of up to 2.6% at most. The maximum difference between the prisms and the Leica Disto D2 was at most 0.21%, which was significantly lower. Therefore, prisms are the main targets used for the scans done in this experiment. As mentioned before though, the reflectors are used to georeference the scans and limit the time pressure on the surveyor team.

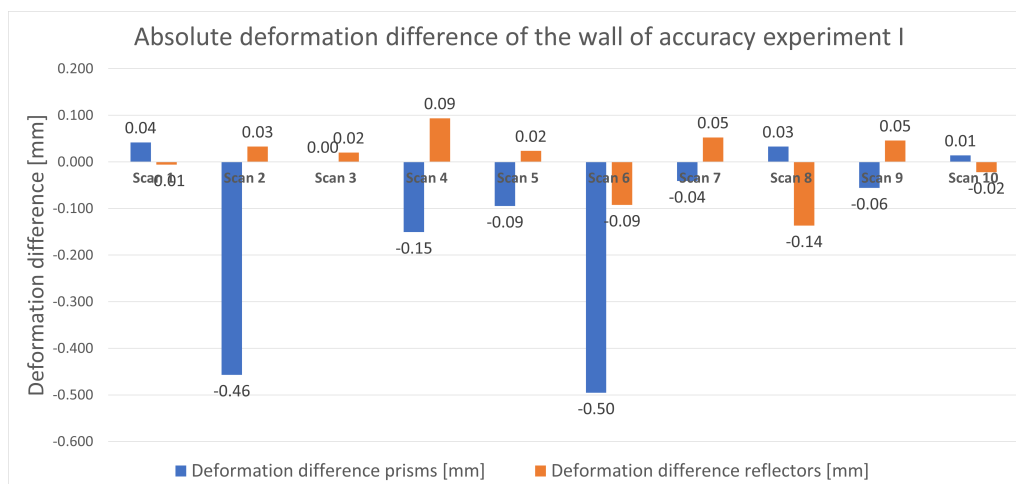


Figure 6.3: Accuracy measurement I absolute deformation results of the wall with respect to the Leica Disto D2.

Figure 6.3 shows the deformation of the wall in the changing room where the experiment was conducted. The wall can be assumed to be stable, as the building was standing still and there was no (mining) activity nearby. From these measurement results, it is important to notice that the measurements with the prisms show a larger discrepancy to the stable wall than the measurements with the reflectors. A possible deduction from this data was that the use of prisms can lead to more noise when looking at stable objects. However, it must be noted that after consultation with GroundProbe, these values are within the range of the noise of the equipment (± 0.5 mm was seen commonly). It is therefore not valid to draw any conclusions based on this.

Experiment II results: repositioning the scanner

For the second experiment, the GML device was removed from the tripod, and the tripod was folded. Then the tripod was repositioned, the GML device was placed back on the tripod and the subsequent scan was conducted. This process was repeated 10 times again for both the set-up with the 3 prisms as well as the 3 reflectors. The cardboard box and the prisms have not been moved in between scans, so the 'true displacement' was zero.

Due to the repositioning of the tripod, the algorithm that was being used to process the data and to align the subsequent scans did not always manage to align the scans exactly on top of each other. This means that a so-called correction was required to align the scans in case they are not correctly matched. The measurements for this research have consisted mainly of periodic scans instead of continuous measurements. Therefore, it was beneficial to explore the impact of applying a correction to the scan results. As this can be quite a subjective process, several corrections are explored in this thesis work, which will be elaborated on in future chapters. First, the results without applying any manual correction are displayed in Figure 6.4.

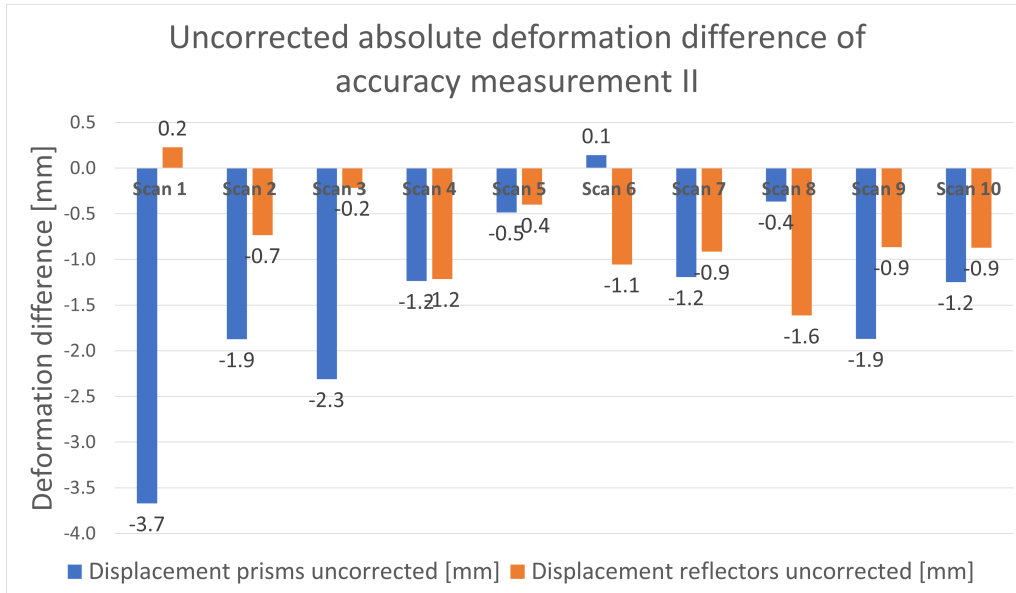


Figure 6.4: Accuracy measurement II (uncorrected) absolute deformation results of the box with respect to the Leica Disto D2.

The results of the raw data with no corrections applied shows that the scans with the use of prisms do not seem to have performed quite as good as before, compared to the reflectors. The prisms even show a difference to the handheld laser of at most -3.7 mm. These results suggested that the prisms can be less accurate when performing periodic scans and not applying any (manual) correction(s).

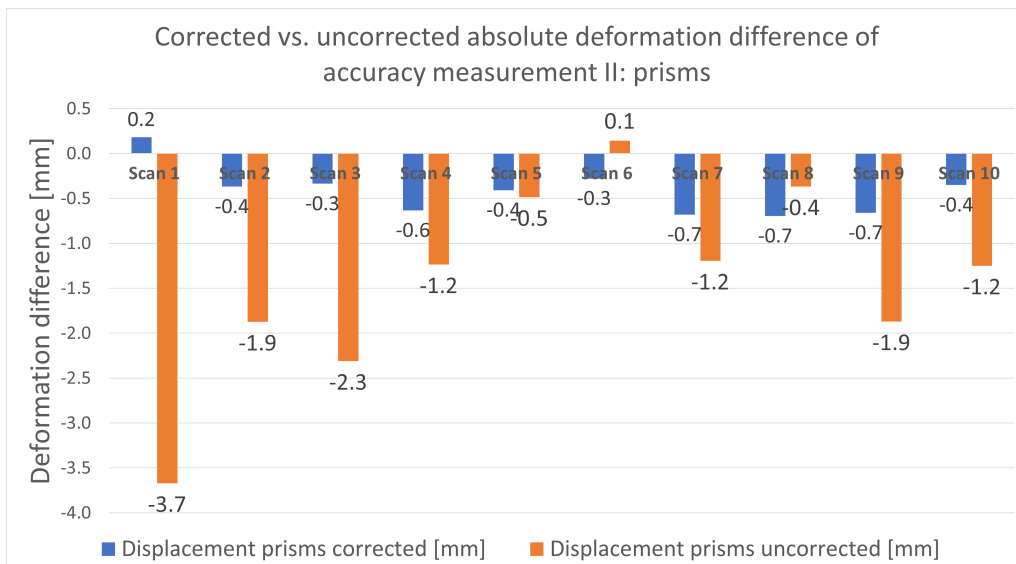


Figure 6.5: Accuracy measurement II: prisms corrected vs. uncorrected absolute deformation results of the box with respect to the Leica Disto D2.

After applying a correction to the scans that involved the use of prisms, the results show more promising accuracy levels, as shown in Figure 6.5. For example, the largest difference to the handheld laser was reduced from -3.7 mm to 0.2 mm, as can be seen in the results for Scan 1. Additionally, the overall average deformation difference was promising and was in the range of the noise levels.

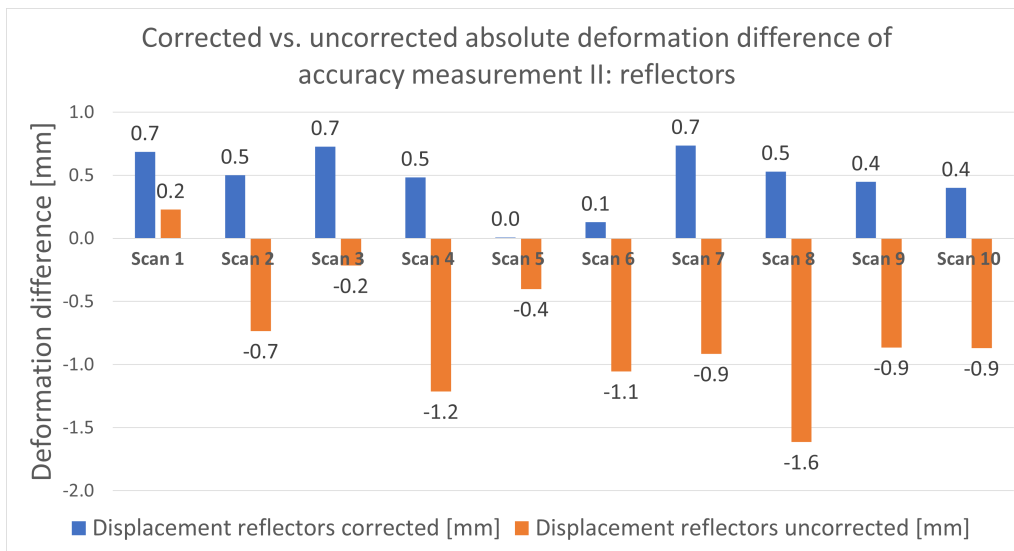


Figure 6.6: Accuracy measurement II: reflectors corrected vs. uncorrected absolute deformation results of the box with respect to the Leica Disto D2.

A similar procedure was conducted for the scans involving the use of reflectors. The result of applying the corrections can be seen in Figure 6.6. A decrease of the error was observed again, but something remarkable is noticed: all of the deformation differences have become positive compared to the Leica Disto D2.

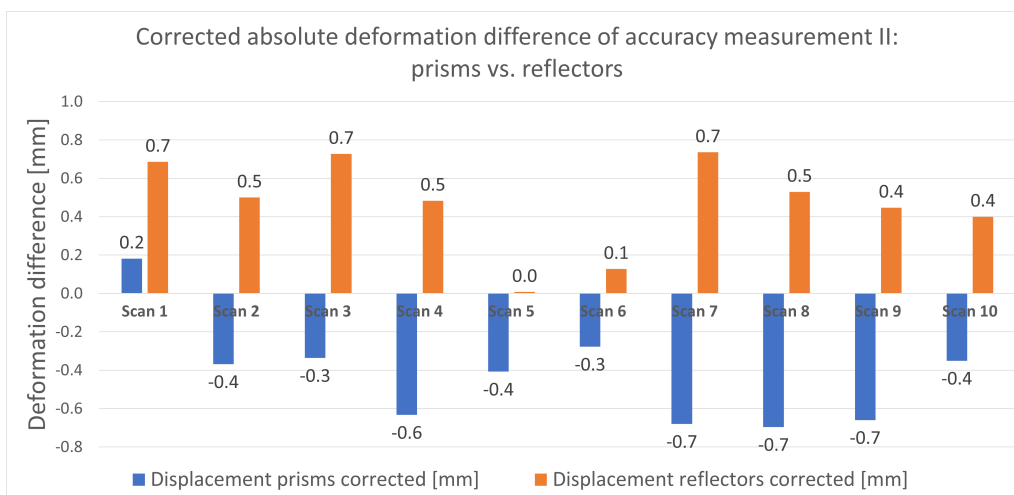


Figure 6.7: Accuracy measurement II: prisms (corrected) vs. reflectors (corrected) absolute deformation results of the box with respect to the Leica Disto D2.

In Figure 6.7, the results for both prisms and reflectors after applying a manual correction have been visualized. As can be seen from this figure, all of the reflector differences are positive and all of the prism differences are negative, except for scan 1. Most importantly, all of the differences for all of the targets are sub millimetre.

Important to realize from the results presented in this section is that although prisms can be more accurate in most of the situations, reflectors proved to be an easier geo-referencing tool in the underground environment. Both prisms and reflectors were therefore used during the analysis in this report.

6.2 LIDAR VERSUS CONVENTIONAL DEFORMATION MEASUREMENTS

In this section the results of the conventional tunnel wall convergence measurement techniques (Total Station and Tape Extensometer) versus the LiDAR deformation scans will be analyzed according to the workflow illustrated in Figure 5.15. This section covers the results from periodic (weekly) LiDAR measurements in room L62-Höger and in rooms KK2 and KK3. Next to that, the application of a (manual) correction was thoroughly analyzed.

6.2.1 Room L62-Höger

In this subsection, the results of the comparison between the GML and the conventional Total Station are discussed. The total deformation of the scan analysis was compared to the total deformation observed from the survey data, to analyze the influence of the use of different targets as well as the influence of applying a manual correction to the LiDAR data. As shown in Figure 5.3, the data was divided over 3 scan locations with 3 different points of interest, point 4, 5 and 6 involving the use of all different targets.

Position 1: L62H-1

The first position used to analyze the GML results was in the middle of the three positions and has the best view at all 3 survey points. Figure 6.8 illustrates the total deformation at survey point 4 based on survey data results compared to the GML results at this same survey point over a timespan of 19 days.

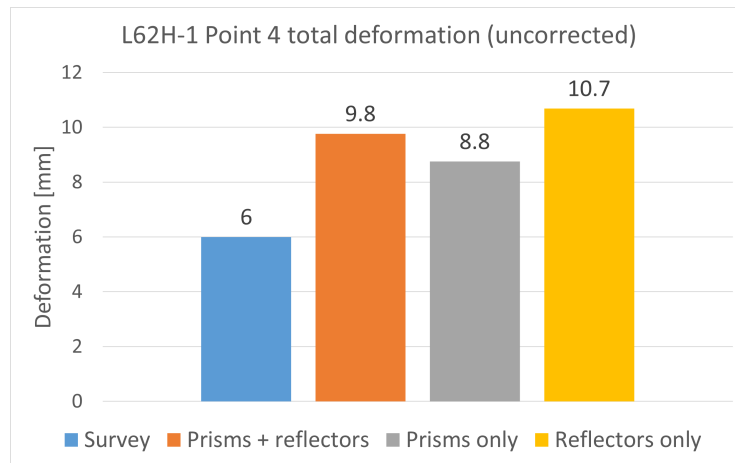


Figure 6.8: L62H-1 survey point 4 total deformation results comparison between the survey data results vs. the LiDAR scans with the use of different targets (uncorrected).

As can be seen in Figure 6.8, the use of different targets provides different results. The total deformation observed in the survey data over this time period was 6 mm. However, when looking at the GML data, it shows some different results. When the scan was processed using only prisms, the result of total deformation is 8.8 mm, which is the closest to the 6 mm with a difference of 2.8 mm. The total deformation measured with the use of prisms + reflectors shows a total of 9.8 mm and the total deformation with the use of only reflectors 10.7 mm. Since the use of prisms only seems to provide the most accurate results compared to the TotalStation and the use of reflectors only the least accurate, it may be possible that the use of the combination of the two targets (prisms + reflectors) leads to a lower accuracy because of the use of reflectors. However, even the most accurate GML measurement data for this experiment shows a deformation that is 45.9% more than the total deformation based on the survey data results.

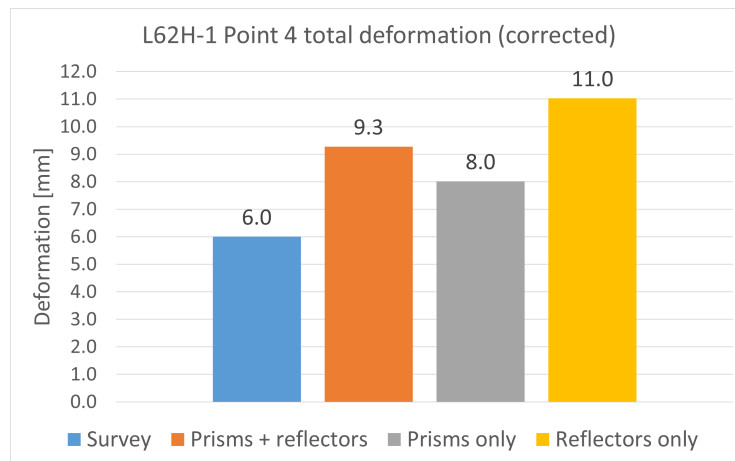


Figure 6.9: L62H-1 survey point 4 total deformation results comparison between the survey data results vs. the LiDAR scans with the use of different targets (corrected).

After applying a manual correction to align the scans with each other, the results have been compared again. This was visualized in Figure 6.9. As becomes clear from this figure, the correction does not always lead to a more accurate result. An example is the scan with the use of reflectors only, where the total deformation without correction is 10.7 mm (Figure 6.8) while the total deformation after a manual correction is 11.0 mm. This was an increase of 3.2% of the measured deformation.

However, the results for prisms only and the combination of prisms + reflectors have been reduced from 8.8 mm to 8.0 mm and from 9.8 mm to 9.3 mm, respectively. These results are closer to the expected 6 mm deformation based on the survey data results. This means that the manual correction has the potential to increase the accuracy of the scan data, but it has to be taken into account that this is a subjective procedure. The only way to manually correct the data, was by removing a symmetrical error whereby you see negative movement on one hand and positive movement on the other.

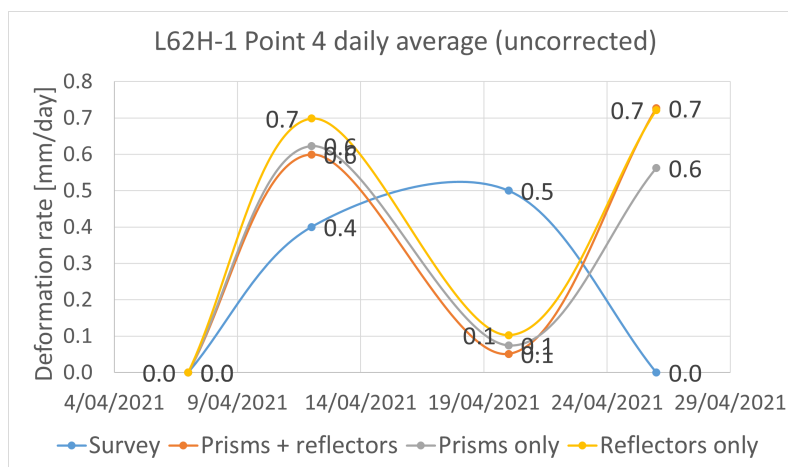


Figure 6.10: L62H-1 survey point 4 daily average deformation results comparison between the survey data results vs. the LiDAR scans with the use of different targets (uncorrected).

Figure 6.10 illustrates the development of the deformation rate overtime during the measurement period. The survey data shows a daily average rate (in blue) with an acceleration at first, then the deformation slows down and eventually stops at 0 mm/day. The GML data clearly shows a different pattern, in an S-shape. From this graph can be derived that for the pattern of movement it does not matter what targets have been used.

Analysis of that pattern shows a relatively high acceleration between the first two measurements, then the deformation rapidly slows down to almost zero, until it accelerates again between the last and second last measurement. As explained in the section [Tunnel wall convergence studies](#), it is of paramount importance to keep track of acceleration of rock mass in underground mining. However, as the GML data shows a very different pattern to the survey measurements, it must be analyzed in further detail to get a better understanding of what is happening in-situ.

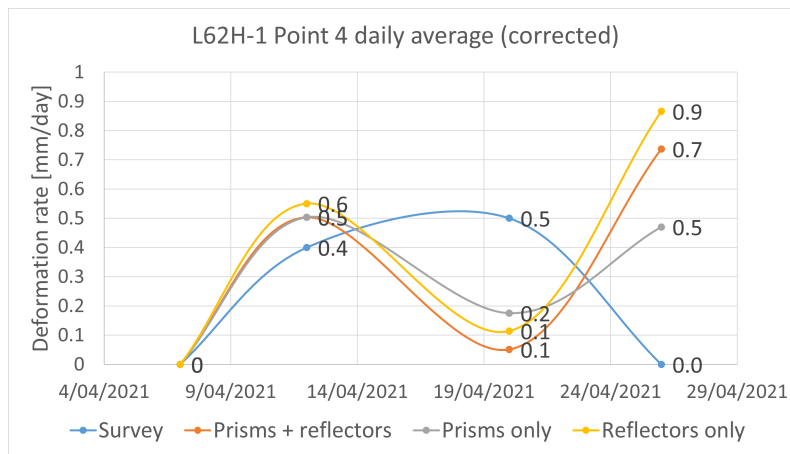


Figure 6.11: L62H-1 survey point 4 daily average deformation results comparison between the survey data results vs. the LiDAR scans with the use of different targets (corrected).

From Figure 6.11 the deformation rate overtime during the measurement period after the manual correction is shown. The survey data remains unchanged. The daily average results in the initial stage are slightly more comparable to the survey data deformation, but the results after that are still showing a significant difference with maximum daily average movement of up to 0.9 mm/day when using reflectors only instead of the 0.7 of the raw LiDAR data.

The result that is closest to what was observed from the survey data was that of the LiDAR data that was processed with the use of prisms only. Something that must be noted is that there is still acceleration measured in the final stage of the experiment, while the rock was expected to slow down eventually.

The sudden acceleration observed was the strongest in the data processed with reflectors only. The rock mass shows a daily average deformation rate of up to 0.9 mm/day in the final stage. This seems highly unlikely, as the rock mass was expected to slow down and no signs of significant movement have been observed.

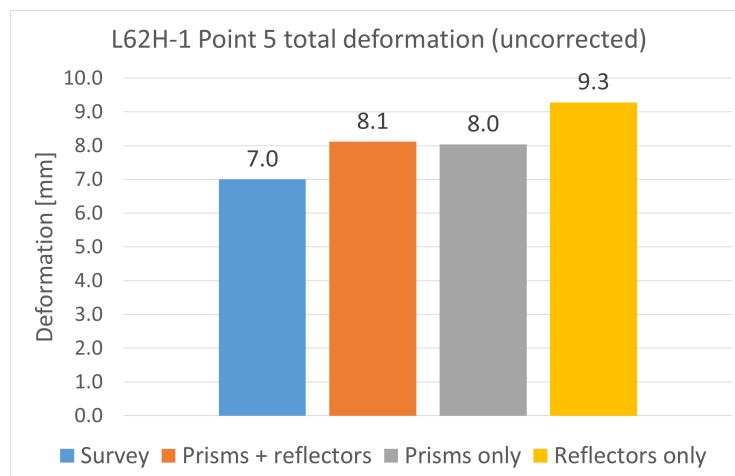


Figure 6.12: L62H-1 survey point 5 total deformation results comparison between the survey data results vs. the LiDAR scans with the use of different targets (uncorrected).

From Figure 6.12 can be seen that the results for this survey point were more similar than the previous survey point which was shown in Figure 6.8. For survey point 5, the GML scan with the use of only prisms shows a total deformation of 8.0 mm compared to the 7 mm based on the survey data results. This means that this time, the presumed most accurate scan result differs 14.9% from the results observed from the survey data. However, it must be noted that the difference was within the range of the expected accuracy of both the TotalStation as well as the GML.

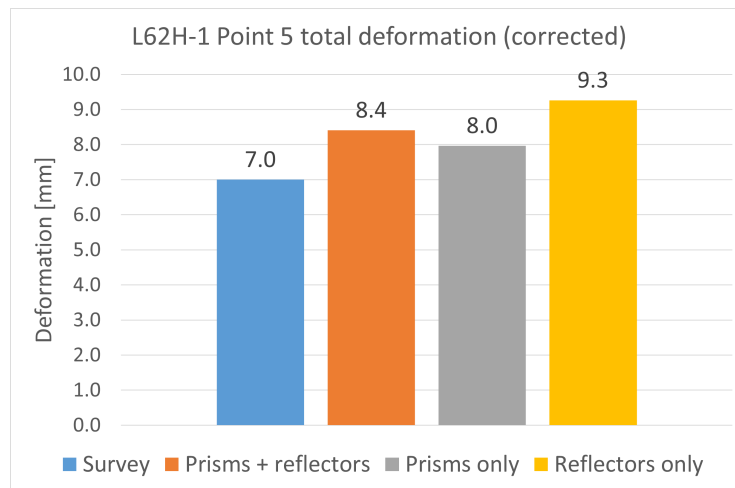


Figure 6.13: L62H-1 survey point 5 total deformation results comparison between the survey data results vs. the LiDAR scans with the use of different targets (corrected).

In Figure 6.13 the total deformation after applying a manual correction to the symmetrical deformation at point 5 is shown. As can be seen, the results are very similar to the results obtained from the raw data. This may be a result of the good visibility of point 5 from the scan location.

The results obtained from processing the data with only prisms shows the most similar results to the results based on the survey data results, a total movement of 8.0 mm was observed compared to 7.0 mm, respectively.

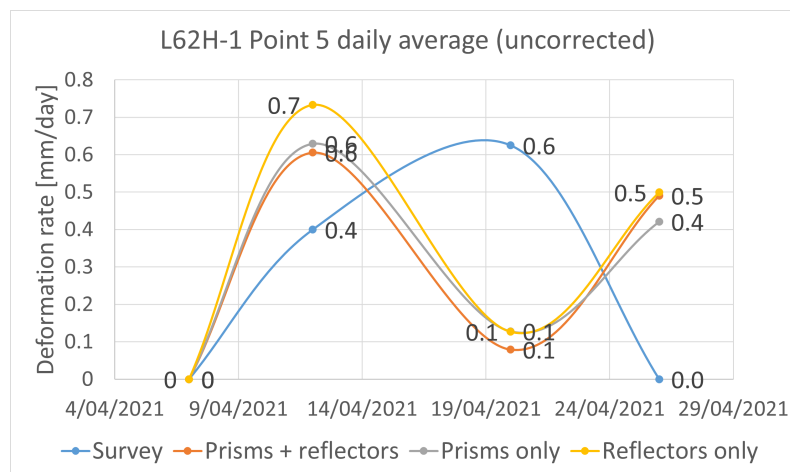


Figure 6.14: L62H-1 survey point 5 daily average deformation results comparison between the survey data results vs. the LiDAR scans with the use of different targets (uncorrected).

Figure 6.14 illustrates the development of the deformation rate overtime during the measurement period. The blue graph illustrates the daily average rate of deformation (in mm/day) based on the survey data results. The same pattern as in Figure 6.10 can be seen. There is an acceleration in the first segment, then the deformation slows down and eventually stops at 0 mm/day again in the end. The GML data again shows the S-shaped pattern. From this graph can be derived that for the pattern of movement it does not matter what targets have been used. There are some small differences between the different targets to note. The reflectors only measurements clearly show a higher acceleration in the start and then joins the graph for the combination of the targets. This can lead to a misinterpretation of the strong acceleration initially and must be carefully analyzed and interpreted.

Analysis of the pattern seen in the GML data shows a relatively acceleration between the first two measurements, then the deformation rapidly slows down to almost zero, until it accelerates again between the last and second last measurement. As mentioned before, it is very important to keep track of accelerations/decelerations of the rock mass in underground mining. Therefore, it is needed to understand the true movement of the rock.

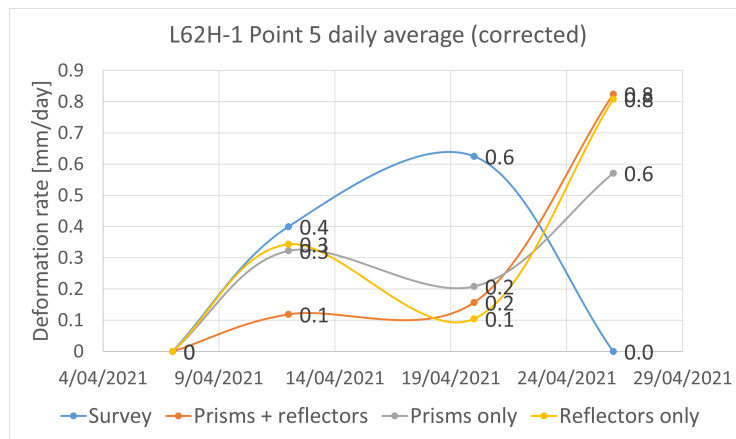


Figure 6.15: L62H-1 survey point 5 daily average results comparison between the survey data results vs. the LiDAR scans with the use of different targets (corrected).

Figure 6.15 illustrates the deformation rate overtime during the measurement period after the manual correction was applied. The daily average deformation in the initial stage seems much more reliable in this data. The second stage of the measurement remains unchanged and then the final stage shows significant signs of acceleration. This is observed especially when using both prisms and reflectors, or when using only reflectors.

Again, the results obtained from the data processed with prisms only is closest to the survey data results. However, the data is closest, but the pattern is still unrealistic. The rock mass shows signs of strong acceleration in the final stage, while the survey data shows that it has stopped moving after some time.

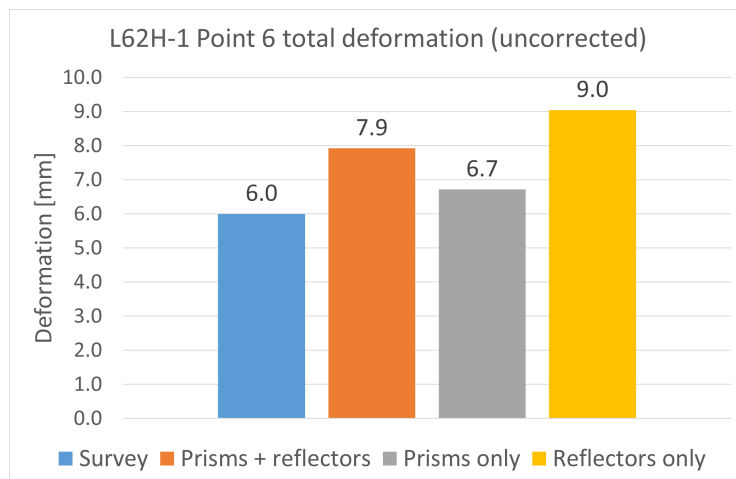


Figure 6.16: L62H-1 survey point 6 total deformation results comparison between the survey data results vs. the LiDAR scans with the use of different targets (uncorrected).

As can be seen in Figure 6.16, the results for this survey point for the use of prisms only are very similar to the results observed in the survey data. The result of the use of prisms only is 6.7 mm total deformation compared to 6 mm measured with the TotalStation. However, the results with the use of prisms + reflectors and the results of reflectors only are less accurate. While the prisms only result differs +12%, the use of prisms + reflectors differs +32% and the results of the reflectors only differs by a total of +51%.

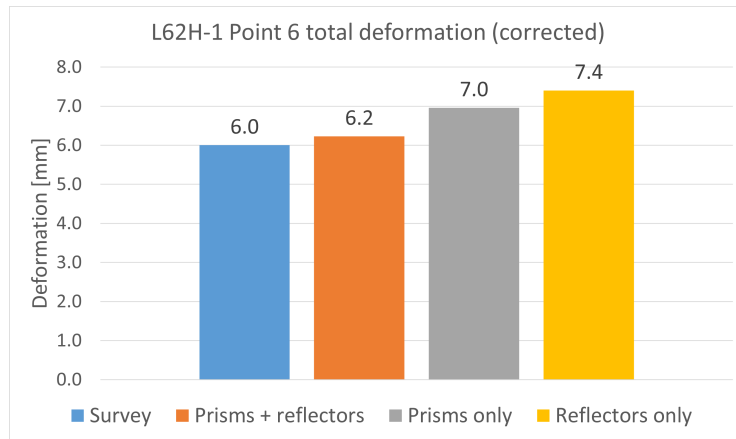


Figure 6.17: L62H-1 survey point 6 total deformation results comparison between the survey data results vs. the LiDAR scans with the use of different targets (corrected).

Figure 6.17 shows the total deformation at point 5 after applying a manual correction to the raw LiDAR data. The results are similar to the raw data results. This is most likely due to the fact that the repositioning error in between these scans did not seem as high. Only small corrections were applied in an attempt to mitigate the repositioning errors of the scan data.

In contrast to the raw data results, the data processed with both the prisms and the reflectors now shows the most similar results to the results obtained by processing the survey data results. However, as must be noted, all results are within reasonable limits and can be erroneous due to accuracy limitations.

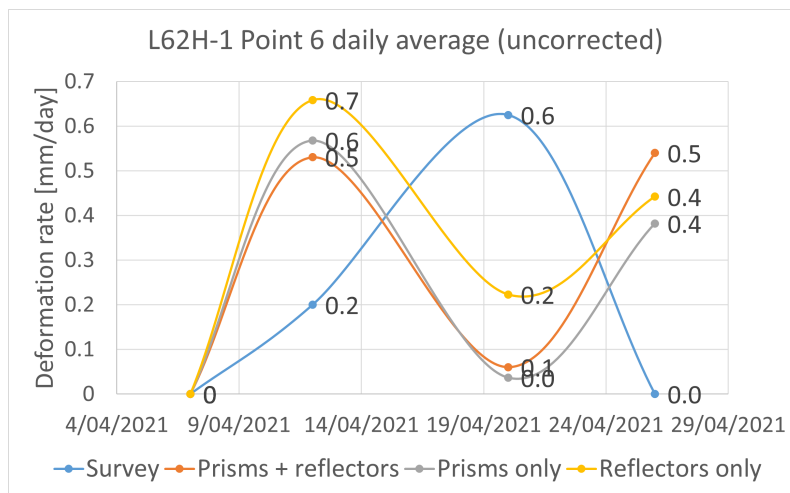


Figure 6.18: L62H-1 survey point 6 daily average deformation results comparison between the survey data results vs. the LiDAR scans with the use of different targets (uncorrected).

Figure 6.18 illustrates the development of the deformation rate overtime during the measurement period. The blue graph illustrates the daily average rate of deformation (in mm/day) based on the survey data results. Again, a similar pattern as in Figure 6.10 and Figure 6.14 can be seen. There is an acceleration in the first segment, then the deformation slows down and eventually stops at 0 mm/day in the end.

The data obtained by the LiDAR scanner again shows the same pattern. However, for survey point 6 the prisms + reflectors daily average is aligned with the prisms only average, while the reflectors only average is slightly different. The initial acceleration is higher than the others, the following deceleration smaller and then it slows down more than the other two. On top of this difference between the use of different targets, the deformation rate in the survey data suggests that the movement of the rock mass comes to a halt at a certain moment. However, the GML data suggests that the movement is increasing.

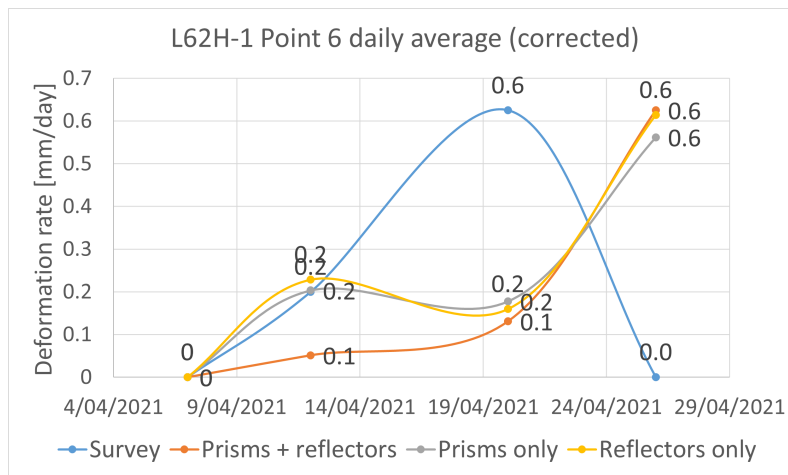


Figure 6.19: L62H-1 survey point 6 daily average deformation results comparison between the survey data results vs. the LiDAR scans with the use of different targets (corrected).

From Figure 6.19 becomes clear that the movement in the initial stage of the measurements is very similar to what was observed from the survey data, in contrast to the raw data. However, the second and the final stage are still strange. The rock mass should show signs of decreased movement, while it accelerates in the LiDAR deformation data. All three processing methods show a very similar daily deformation graph in this data.

Position 2: L62H-2

The second position used to analyze the GML results is the furthest from the survey points and thus has the least visibility and the most oblique angle with respect to the survey points. Survey point 4 was completely invisible and therefore it was removed from this analysis. Figure 6.20 shows the total deformation at survey point 5 based on the survey data results compared to the GML LiDAR results at this same survey point over a timespan of 19 days.

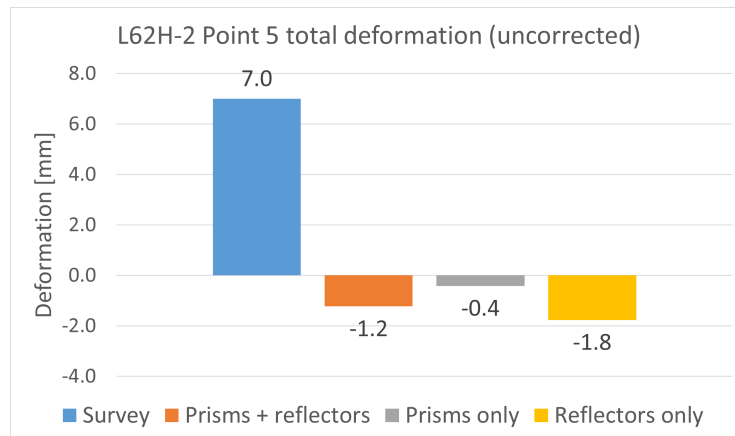


Figure 6.20: L62H-2 survey point 5 total deformation results comparison between the survey data results vs. the LiDAR scans with the use of different targets (uncorrected).

As survey point 5 was visible from this position, it is included in the analysis. The angle at which it is hit by the LiDAR scanner does however make it difficult to achieve accurate results (as mentioned by Fekete et al. [2010] as well). From Figure 6.20 can be derived that the total deformation measured by the LiDAR deformation scans deviate significantly of the total deformation of 7.0 mm observed in the survey data. Even so much, that the LiDAR deformation results show negative results. This suggests that the roof of the tunnel where measurement point 5 is located, has moved upwards by at most 1.8 mm.

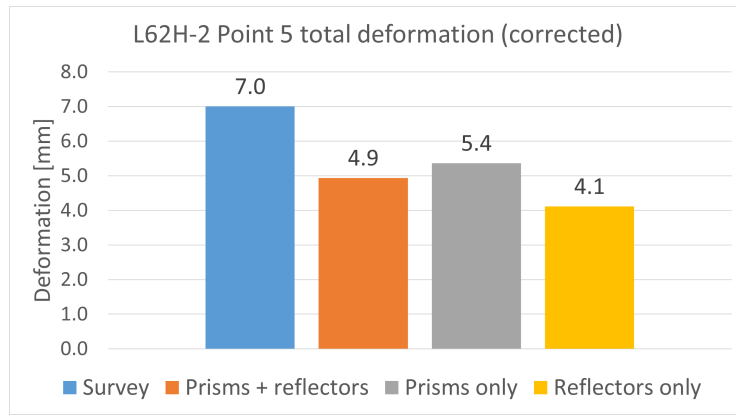


Figure 6.21: L62H-2 survey point 5 total deformation results comparison between the survey data results vs. the scans with the use of different targets (corrected).

After applying a manual correction to properly align the scans with each other, the results have been compared again. This is visualized in Figure 6.9. From this graph can be derived that after applying the alignment correction, the results are much closer to the deformation based on the survey data results. Additionally, the results are now positive instead of negative. A reason for the change in sign of the deformation can be that the repositioning of the scanner was done in such a way, that the height of the tripod varied too much, leading to the scanner being lower to the ground. If the scanner is lower to the ground than in previous scans, it may seem that the roof has gone further away from the scanner, which is possible to a certain extent, but is not deemed realistic in this area.

Under the assumption of the survey data showing the true deformation of survey point 5, the use of prisms only provides the most promising results in this set-up with a $7.0 - 5.4 = 1.6$ mm difference or 22.9%. However, it is still much more accurate and a more reliable result (solely judging numbers) than without applying any correction. Something that must be taken into account when analyzing these results is the bias of the person that applies the correction. If the 'true deformation' is known beforehand, the person may try to apply a correction in such a way that the data correlates better, which is not always the case.

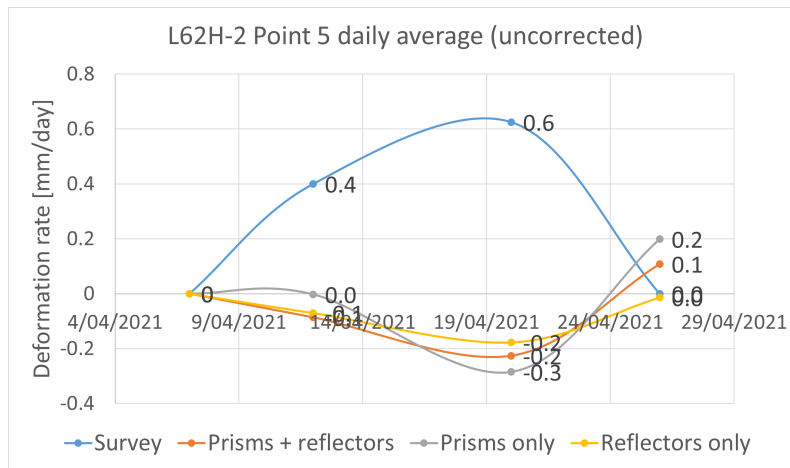


Figure 6.22: L62H-2 survey point 5 daily average deformation results comparison between the survey data results vs. the LiDAR scans with the use of different targets (uncorrected).

In Figure 6.22 the development of the deformation rate overtime can be seen. In blue, the daily average rate of deformation (in mm/day) based on the survey data results is shown. The survey data shows an acceleration initially and then the deformation rate has decreased to 0 mm/day at the end of the measurement period.

The LiDAR data shows a very different pattern. It seems that in the initial stage of the deformation, the rock at point 5 is moving away from the scanner and then in the final stage it comes back down. This can be possible if some shotcrete would be scraped or some similar mining activity, but it was not done at this stage of the experiment. Therefore, this type of movement seems very unlikely.

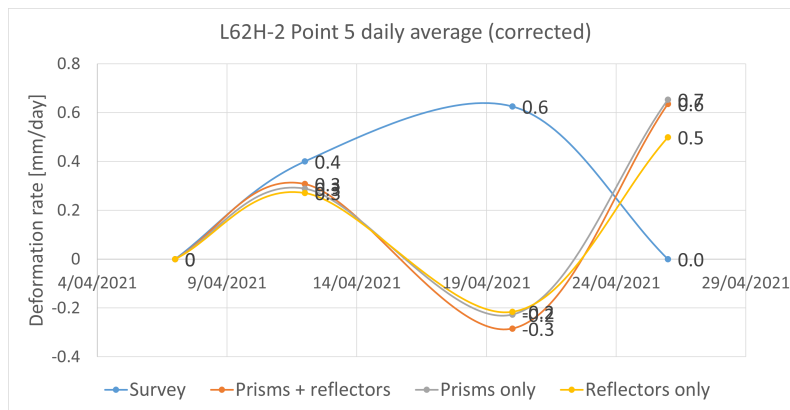


Figure 6.23: L62H-2 survey point 5 daily average deformation results comparison between the survey data results vs. the LiDAR scans with the use of different targets (corrected).

After a manual correction was applied for the repositioning error of the scanner, the daily average results were found to be as shown in Figure 6.23. This figure shows a very different pattern than the previous one. The initial deformation rate is now found to be very similar to the survey data, with a strange dip to a negative rate in the middle, and finally a rapid acceleration of the deformation.

Especially the rate obtained in this final stage is concerning, because as discussed before in section 2.1, the convergence is expected to slow down after a certain time. If the convergence shows an acceleration, this can cause reason for concern because it indicates that the rock started moving which may lead to failure zones. When comparing it to the rate observed from the survey data and the literature (i.e. Assali et al. [2016]), it makes no sense to assume that the LiDAR deformation rate is correct. No significant movement was observed during the final stage of the experiment.

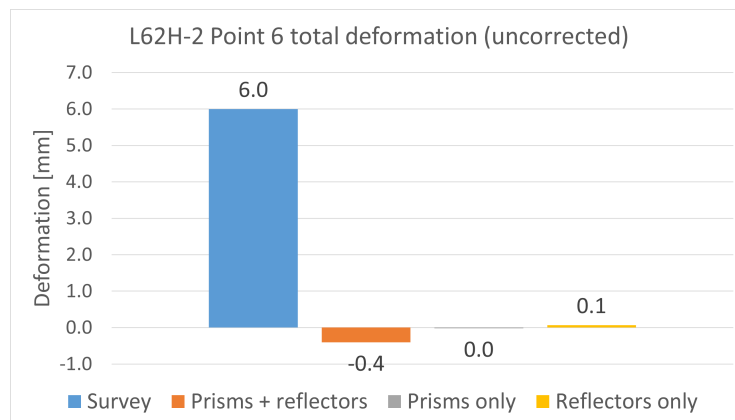


Figure 6.24: L62H-2 survey point 6 total deformation results comparison between the survey data results vs. the scans with the use of different targets (uncorrected).

The raw LiDAR data observed at survey point 6 shows a similar trend as the data observed at survey point 5, namely a negative or even a zero millimetre total deformation. Point 6 should in theory be visible better than point 5, if it would not have been so close to the ventilation tube. On top of that, the angle at which this survey point is hit is highly oblique (≥ 60 degrees) which makes it difficult to obtain accurate results (as mentioned by Fekete et al. [2010]).

In Figure 6.24 the results of the GML scanner are shown as comparison to what was obtained from the survey data. The total deformation at survey point 6 is 6.0 mm. The tunnel walls showed clear signs of convergence damage, as shown in Figure 6.25. Cracks in the shotcrete are typically found at locations where the tunnel converges over time, according to Bolidens rock mechanical engineers.



Figure 6.25: Shotcrete damage found in L62-H as result of convergence. (a) Shotcrete damage in the top right wall. (b) Shotcrete damage in the right wall.

Therefore, it is safe to assume that the tunnel was in reality converging, and not showing almost zero movement, as the raw LiDAR data suggests.

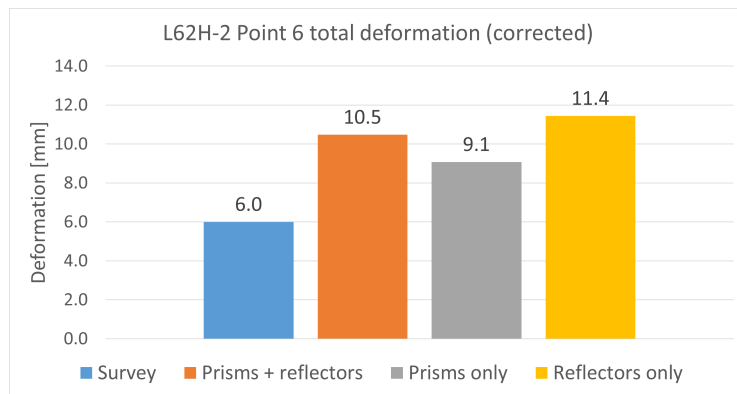


Figure 6.26: L62H-2 survey point 6 total deformation results comparison between the survey data results vs. the scans with the use of different targets (corrected).

After applying a manual correction to the deformation data, the results at survey point 6 seem more realistic, but may be too high. Taking into account the accuracy of the Total Station used from the survey data, there should be only a ± 1 mm difference. The result from the LiDAR scanner that is closest to the survey data is with the use of prisms only, which shows a total deformation of 9.1 mm. Even this closest result differs 51.7% from the Total Station results.

Additionally, once again, the 'true deformation' of 6.0 mm was known beforehand and therefore the manual correction may have an amount of bias towards this result. However, these results do seem more realistic than what the raw data was suggesting.

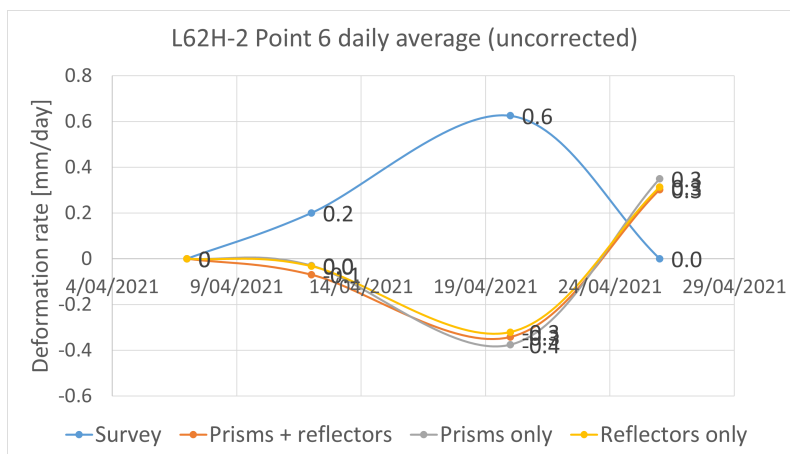


Figure 6.27: L62H-2 survey point 6 daily average deformation results comparison between the survey data results vs. the LiDAR scans with the use of different targets (uncorrected).

The uncorrected daily average deformation rate at survey point 6 is shown in Figure 6.27. Again, a very similar pattern as the one at point 5 is observed. In the initial stage, (almost) nothing seems to happen within the rock, then a negative deformation rate is measured and finally the rate goes back up. Contrasting to those results, the survey data measurements show an initial acceleration and then in the final stage the rock stopped moving entirely.

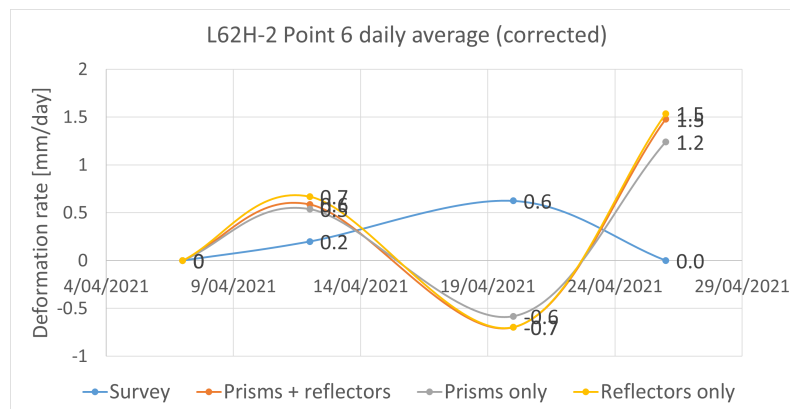


Figure 6.28: L62H-2 survey point 6 daily average deformation results comparison between the survey data results vs. the LiDAR scans with the use of different targets (corrected).

After the correction was applied, the initial stage shows strong deformation rates, while the stage in the middle shows a very negative deformation rate. Finally, the rock accelerates from -0.7 mm/day up to 1.6 mm/day in the manually corrected LiDAR data. If this were truly the case, this would ring many alarm bells because this would have high potential to become a failure zone. The fact that the strong negative deformation rate in the middle is physically impossible along with the very strong acceleration, which is not observed from the survey data at all, this seems highly unlikely to be the case.

Position 3: L62H-3

The third position used to analyze the GML results is the closest to the survey points and should especially be able to obtain good results for survey points 4 and 6, because they had the best visibility from this location. Figure 6.29 shows the total deformation at survey point 4 based on the survey data results compared to the raw GML LiDAR results at this same survey point over a timespan of 19 days.

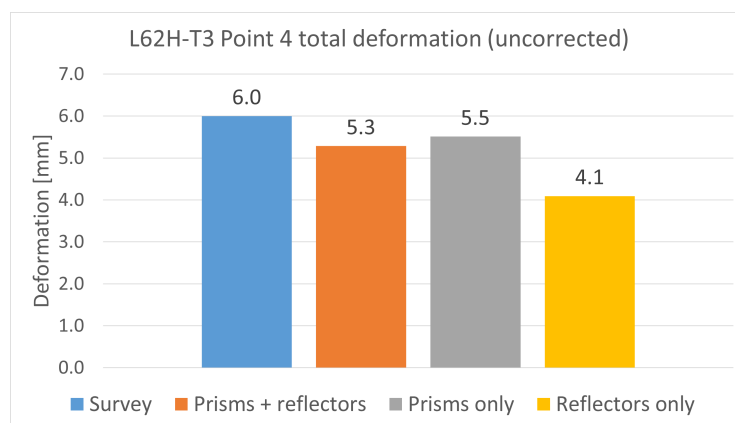


Figure 6.29: L62H-3 survey point 4 total deformation results comparison between the survey data results vs. the scans with the use of different targets (uncorrected).

As this point was clearly visible and close to the scan location, it was expected to give good results (based on GroundProbe [2021b] and Fekete and Diederichs [2013]). When comparing the total deformation observed from the raw data set to the deformation observed from the survey data, it can be seen that it indeed gives very comparable results. The data processed with prisms only provides the result similar to the results obtained from the survey data, with a total deformation of 5.5 mm.

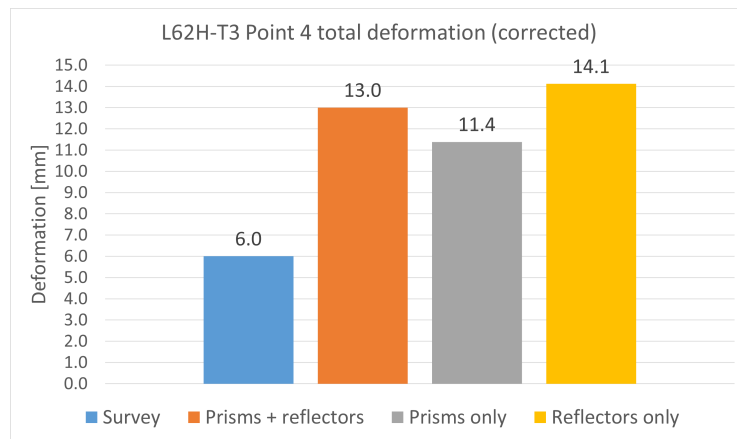


Figure 6.30: L62H-3 survey point 4 total deformation results comparison between the survey data results vs. the scans with the use of different targets (corrected).

After applying a manual correction for the repositioning of the scanner, the results turned out to become worse in this case, under the assumption that the survey data is accurate. From Figure 6.30 can be seen that instead of the total deformation results getting closer to the survey data, they differ approximately 100%, with at most 14.1 mm instead of the measured 6.0 mm. Therefore, these results do not make sense. This can be a result of a correction bias, but also an issue in the algorithm of the processing software.

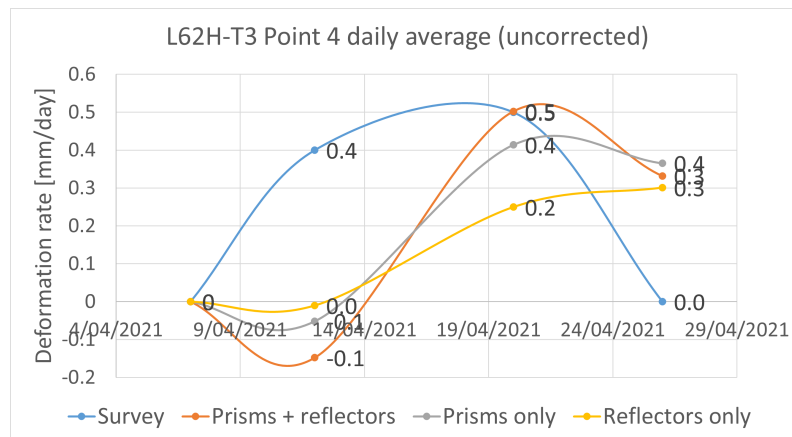


Figure 6.31: L62H-3 survey point 4 daily average deformation results comparison between the survey data results vs. the LiDAR scans with the use of different targets (uncorrected).

The uncorrected daily average deformation rate at survey point 4 is shown in Figure 6.31. The blue line shows the rates observed from the survey data and the other 3 lines show the results from the raw LiDAR data. While the survey measurements show a very gradual progression of the tunnel convergence over time, the LiDAR data does not. Especially the end of the measurement period is interesting, because the rock movement should show signs of decreased movement, which it does not show significantly.

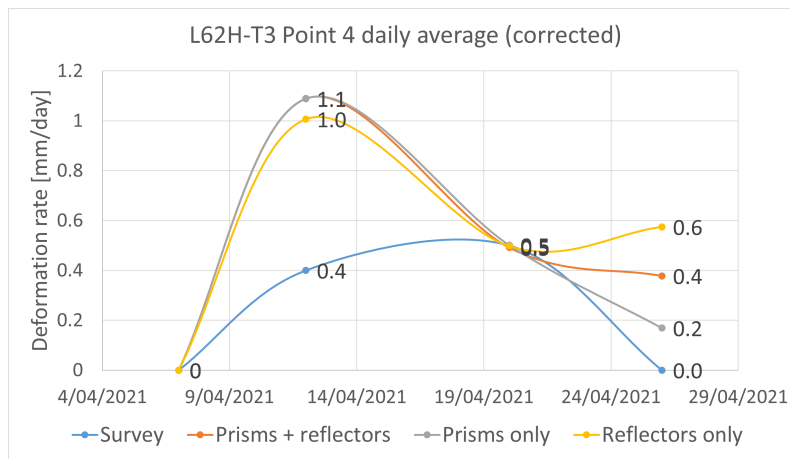


Figure 6.32: L62H-3 survey point 4 daily average deformation results comparison between the survey data results vs. the LiDAR scans with the use of different targets (corrected).

The daily average deformation after the manual correction with the use of prisms only shows almost exactly the same trend as measured by the survey data, but the numbers are unrealistic. An increasing deformation initially that gradually slows down overtime to (almost) zero mm/day is observed by analyzing the survey data. However, in the LiDAR data in the initial stage, the deformation rate is relatively high with a rate of up to 1.1 mm/day. The survey data shows only 0.4 mm/day in the initial stage, which is almost 1/3rd times lower.

Then the movement slows down to 0.5 mm/day with eventually the prisms only results showing the most similarity to the survey data results with the rate of movement in the rock decreasing in the final stage. However, the 1.1 mm/day in the initial stage seems very unlikely.

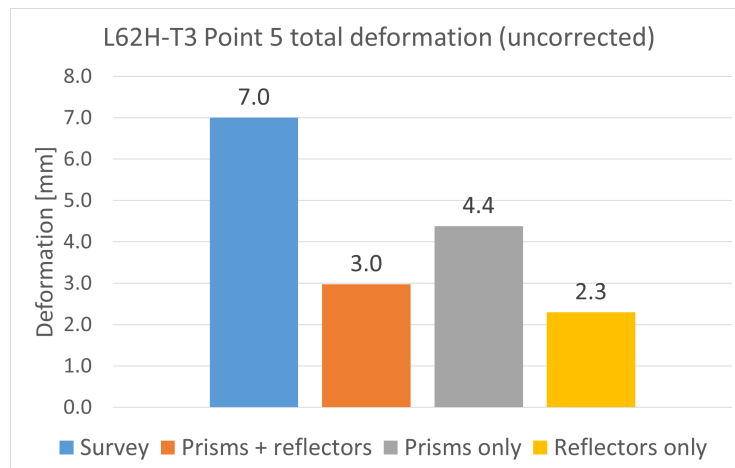


Figure 6.33: L62H-3 survey point 5 total deformation results comparison between the survey data results vs. the scans with the use of different targets (uncorrected).

Point 5 was more difficult to see from this position and the assumption is therefore that the results may vary from the 'true deformation'. What must be noted is that it was still very close to the scanner meaning that the results could still be reasonable. The results are shown in Figure 6.33.

Although the results are not identical to the deformation identified from the survey data, they seem to be within a realistic range. Especially the 4.4 mm deformation measured by the raw data processed with prisms only is reasonably close to the convergence measured by the survey data (7.0 mm). It must be taken into account that this is still a significant difference of $7.0 - 4.4 = 2.6$ mm or 37%.

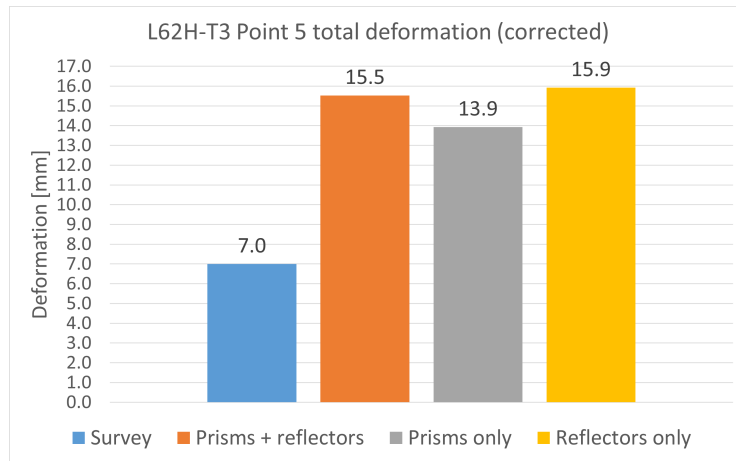


Figure 6.34: L62H-3 survey point 5 total deformation results comparison between the survey data results vs. the scans with the use of different targets (corrected).

In Figure 6.34 the results of the total deformation measured from the LiDAR data after the manual correction is shown. Again, as was observed at point 4, the data differs more from the survey data than before. These results do not seem realistic, as no significant deformation was observed in the room. The manual correction can prove to lead to erroneous values in this case, as a result of human error or a flaw in the algorithm. It is also possible that the limited visibility of the measurement point leads to wrong results.

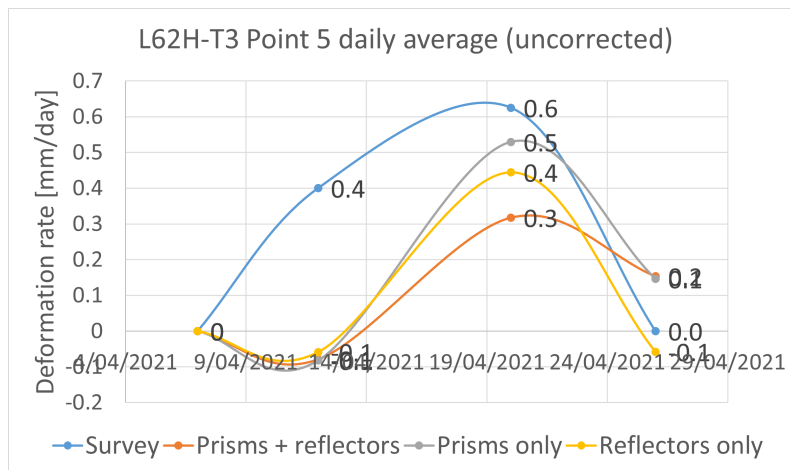


Figure 6.35: L62H-3 survey point 5 daily average deformation results comparison between the survey data results vs. the LiDAR scans with the use of different targets (uncorrected).

The raw data daily average deformation rate at survey points 5 is shown in Figure 6.35. The gradual pattern observed by the survey data is not as gradual when looking at the LiDAR data. The data suggests that the rate of movement in the tunnel was decreasing in the initial stage, then accelerated with deformation rates of up to 0.5 mm/day (in contrast: the survey data deformation shows a rate of movement in the rock mass of 0.6 mm/day). Then the LiDAR data shows signs of decreased movement in the rock mass in the final stage, which is in line with expectations.

In this case, the LiDAR data processed with the different targets all show similar results in terms of the deformation pattern. The data processed with prisms only shows similar rates to the rates observed from the survey data.

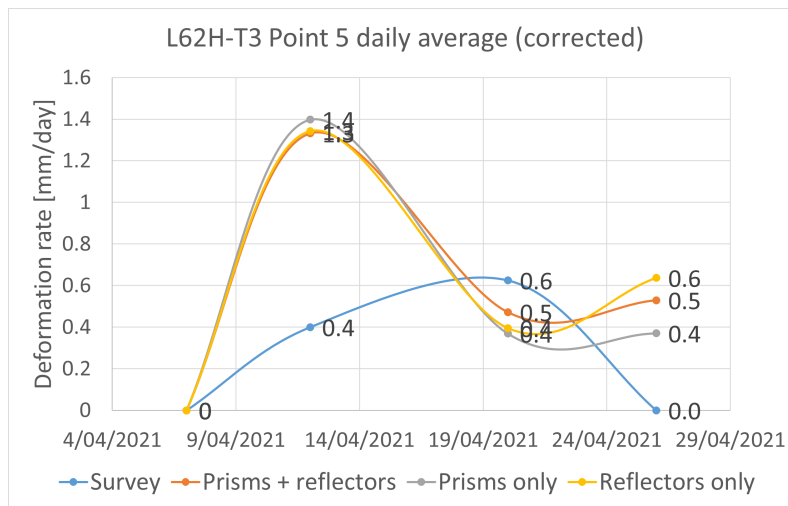


Figure 6.36: L62H-3 survey point 5 daily average deformation results comparison between the survey data results vs. the LiDAR scans with the use of different targets (corrected).

When looking at the daily average deformation rates after the correction, the trend of the movement in the rock mass is very unrealistic compared to the TotalStation measurements. The significant peaks in the LiDAR data during the initial stage of up to 1.4 mm/day compared to 0.4 mm/day seem unlikely but theoretically not impossible. The rock mass then slows down to a nearly constant deformation in the final stage.

As the rock mass is expected to have stopped moving by the end of this experiment, the constant deformation rate is deemed unrealistic. The raw LiDAR data showed signs of decreasing rate of movement in the rock mass in the end, this makes more sense and is almost similar to what is observed in the survey data.

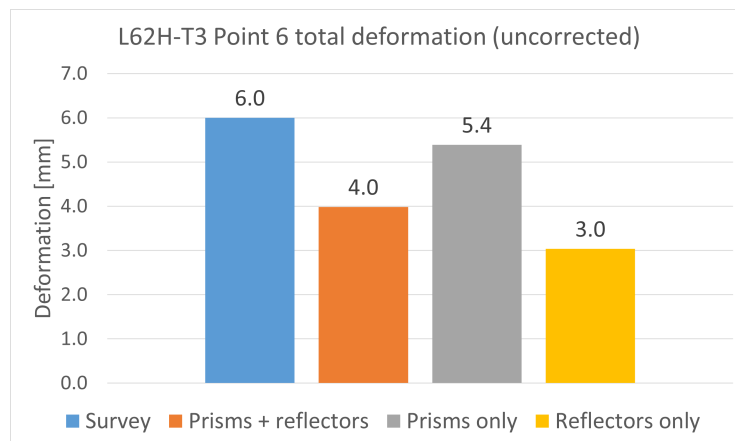


Figure 6.37: L62H-3 survey point 6 total deformation results comparison between the survey data results vs. the scans with the use of different targets (uncorrected).

Finally, the results of measurement point 6 are shown in Figure 6.37. This measurement point deformation data with the use of prisms only has shown to be very similar the deformation obtained from the survey data data, 5.4 mm with respect to 6.0 mm, respectively. The use of reflectors only is again the least accurate and the combination of both reflectors and prisms in the middle.

The reflectors only data shows a difference of a total of 3.0 mm or 50%, which is still reasonable. Signs of major deformation zones (> 50 mm) or potential danger zones can still be identified, even with a 3.0 mm difference.

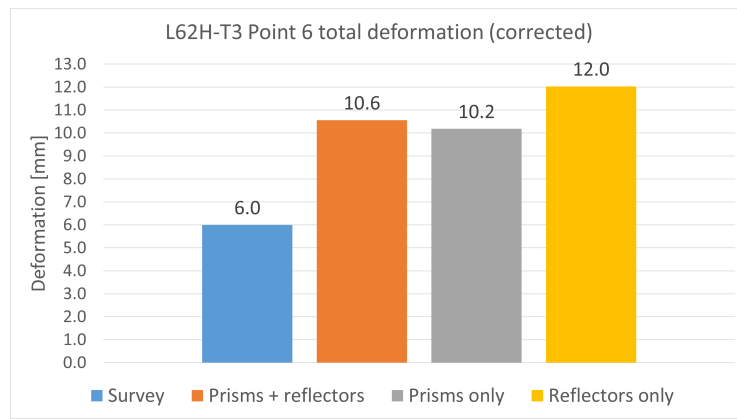


Figure 6.38: L62H-3 survey point 6 total deformation results comparison between the survey data results vs. the scans with the use of different targets (corrected).

Figure 6.38 shows the corrected total deformation results. As seen at point 4 and 5 as well, the deformation results differ more than the raw data has shown. These results are also not expected to be correct. The raw data results with using only prisms prove to be the most realistic.

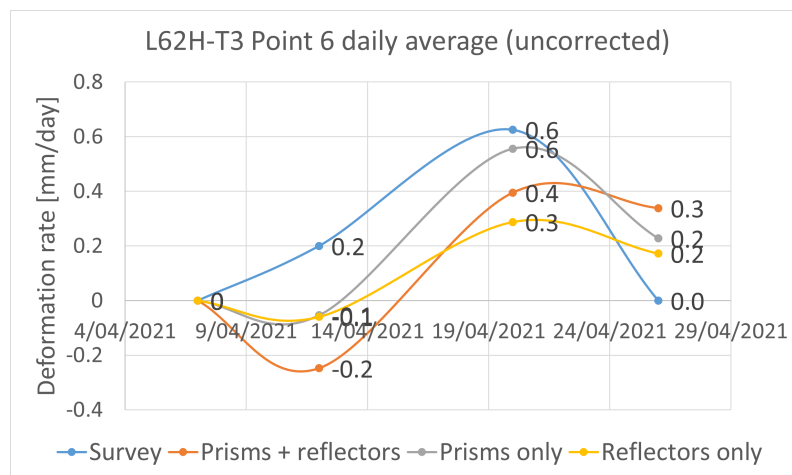


Figure 6.39: L62H-3 survey point 6 daily average deformation results comparison between the survey data results vs. the LiDAR scans with the use of different targets (uncorrected).

The daily average deformation rate of the raw LiDAR data at survey point 6 is illustrated in Figure 6.39. The data shows deceleration in the initial stage again, then accelerates and finally slows down to low deformation rates. The pattern is not very unlikely assuming that there is a small accuracy error, especially in the initial stage where the rock is not expected to decelerate. This would technically mean that the rock mass would move away from the scanner and the tunnel would thus diverge, instead of converge, which is possible in theory, but not expected in this setting.

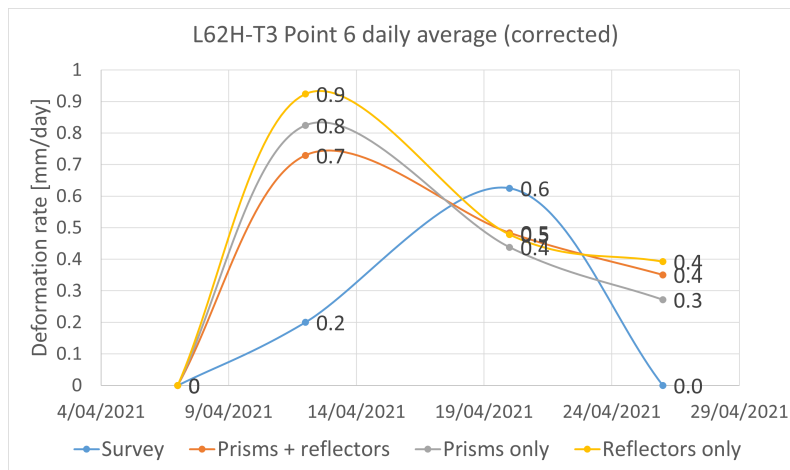


Figure 6.40: L62H-3 survey point 6 daily average deformation results comparison between the survey data results vs. the LiDAR scans with the use of different targets (corrected).

The average daily deformation rates after the correction show high rates, especially in the initial stage of the experiment, where rates of up to 0.9 mm/day are observed in the data. This is not in line with the expectations. The rock mass did show signs of decreased movement in the final stages of this experiment (i.e. little to no shotcrete damage visible and the face progressing further away).

In contrast to the survey deformation results, the LiDAR data suggests that the majority of the movement has occurred in the initial stage of the experiment until the rock halts to a more constant deformation rate. This would not be impossible if the measurement point was very close to the face and most deformation would be blast-induced, but since that was not the case, the assumption is that these results are incorrect.

6.2.2 Room KK2

On top of the LiDAR scans, tape extensometer measurements have been conducted in room KK2, to verify the accuracy of the LiDAR deformation scans. As explained in subsection [Tape Extensometer](#), the measurements with the digital tape extensometer typically have a relatively high accuracy of ± 0.01 mm, but the result is limited to two specific points.

A sketch on top of the greyscale LiDAR data visualization is illustrated in [Figure 6.41](#). The locations of the tape extensometer measurement points are highlighted by red circles, while the survey measurement point is highlighted by a navy blue circle (Survey Point I (SP₁)).

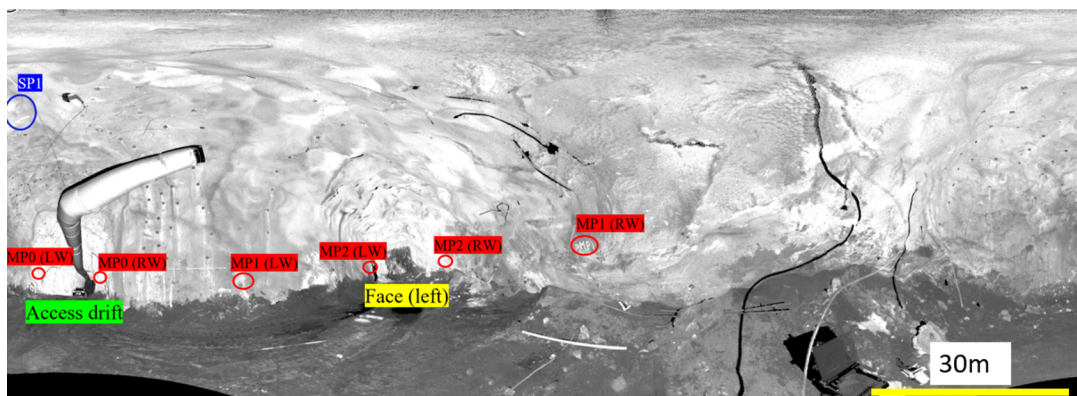


Figure 6.41: Illustration of the layout of the periodic measurements in KK2 on location 2. MP = measurement point, SP = survey point, LW = left wall, RW = right wall.

The results of the GML LiDAR scans have been compared to the tape extensometer measurement results. The scans are compared in three different settings: a) the raw data processed by GroundProbe's software, b) the data after applying a manual correction to remove symmetrical errors and c) the LiDAR data after applying the auto alignment function.

Manual corrections can be applied when a symmetrical error is observed, as explained earlier in [Figure 5.22](#). This is however a subjective way of aligning the scans, because the 'true deformation' is unknown. Therefore, such corrections have only been applied to remove the symmetrical error. Once this is achieved, no further correction was applied.

The auto alignment function is a function of GroundProbe's processing software GMLControl. The algorithm of the software attempts to automatically match points in the PCD to analyze if there is a better alignment solution than the original alignment. After consultation with GroundProbe, it has become clear that this algorithm is not yet optimized, but it was decided to analyze how well the algorithm performs compared to other methods.

As can be seen in Figure 6.41, MP0 is located in the access drift, which is assumed to be moving the least (Lato and Diederichs [2014]) and this is confirmed by Boliden's earlier measurements. The point based on the survey data results through a Total Station is called Survey Point 1 (SP1). This point is located exactly at the intersection between the access drift and the room itself.

The other two tape extensometer measurement points are located towards the face, which is initially on the left side of the room. The first measurement point, MP1, is located close to the scanner with little to no possible occlusion. This point should provide the most accurate results (Lato et al. [2010]). The second measurement point within the room, MP2, is located closer to the face. Due to the longer distance and the oblique angle, this can lead to less promising results (GroundProbe [2021b]).

Figure 6.42 illustrates the total deformation results observed at MP0 over time. As can be seen, the GML shows very different results at this measurement point when compared to the tape extensometer. One of the explanations can be the oblique angle at which the scanner hits the surface.

Especially on the right wall, the deformation results are erroneous compared to what is observed with the eyes. The results of the deformation in the right wall are spiking up and down, showing an alteration between positive and negative deformation results. These results are presented in Appendix A.

The auto alignment method shows fairly similar results compared to the raw scan data and the manually corrected data when looking solely at the total deformation results.

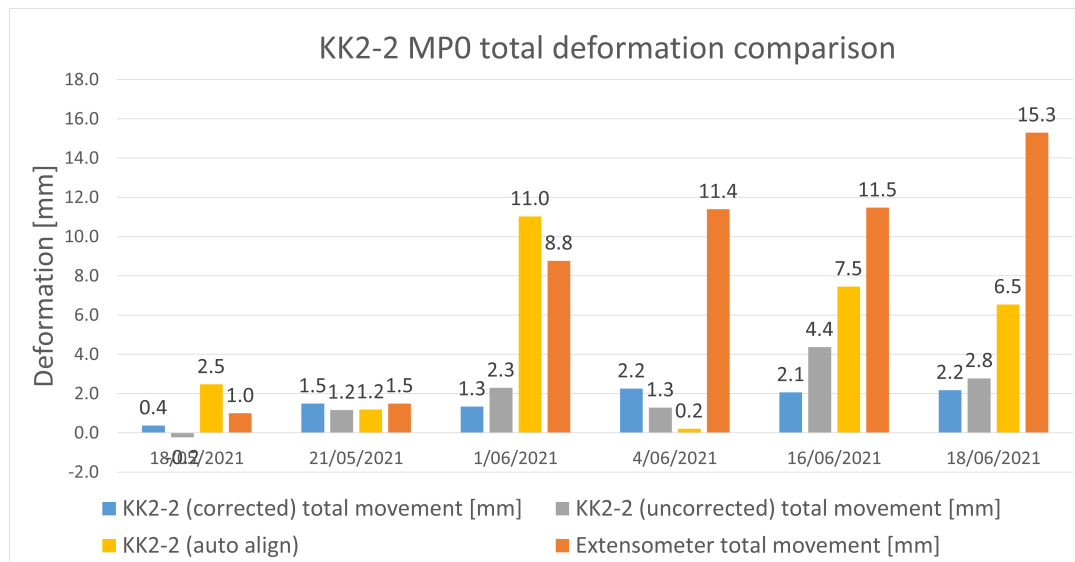


Figure 6.42: Comparison of LiDAR total deformation results vs tape extensometer results at KK2 location 2, measurement point o.

However, when inspecting the data on the daily average movement that is measured in between scans in Figure 6.43, it becomes clear that the auto alignment option is spiking up and down, which seems very odd. This would mean that the walls in which MP0 is located are alternating between convergence and divergence, which is physically impossible.

The manually corrected data follows a similar trend as the deformation measured by the tape extensometer. The uncorrected data graph is almost a mirror of the tape extensometer measurements. From this data it seems like the tunnel deformation is accelerating while the tape extensometer shows a deceleration and vice versa.

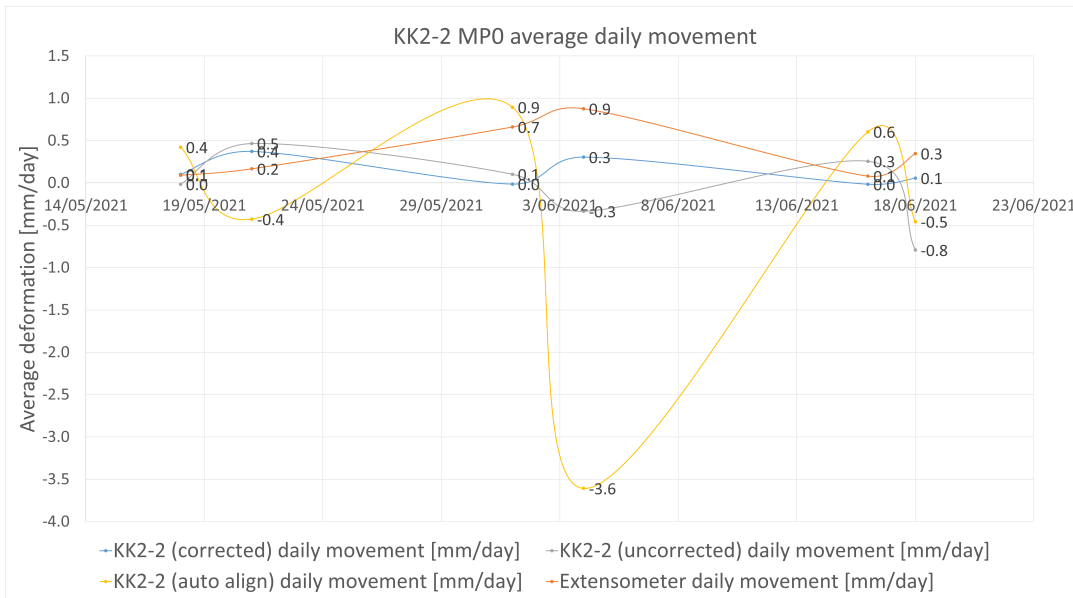


Figure 6.43: Comparison of LiDAR daily average deformation vs tape extensometer results at KK2 location 2, measurement point o.

Figure 6.44 illustrates the total deformation results observed at MP1 over time. At 18/06/2021, the tape extensometer equipment failed, which is why the measurement is left at 0.0. However, 18/06/2021 was left in the graph to illustrate how the GML data progressed in just a 2 day window. From the graph can be derived that the LiDAR data results were similar to the actual tape extensometer results up until 04/06/2021.

It must be noted that again the auto aligned data performs better than the other two, mainly because it is the only one that shows an increase in deformation at every stage till 16/06/2021. When looking at the actual data in more detail it becomes clear that although the total deformation sums up quite accurately (-3.2 mm at most at 07/05/2021), the movement in the individual walls make no sense.

The biggest problem seems to be that the algorithm does not manage to align the subsequent periodic scans properly, leading to a significant repositioning error. The left wall shows positive deformation throughout all measurements, while the right wall shows negative deformation results. After consultation with the rock mechanics engineers from Boliden, this seems highly unlikely to be the case.

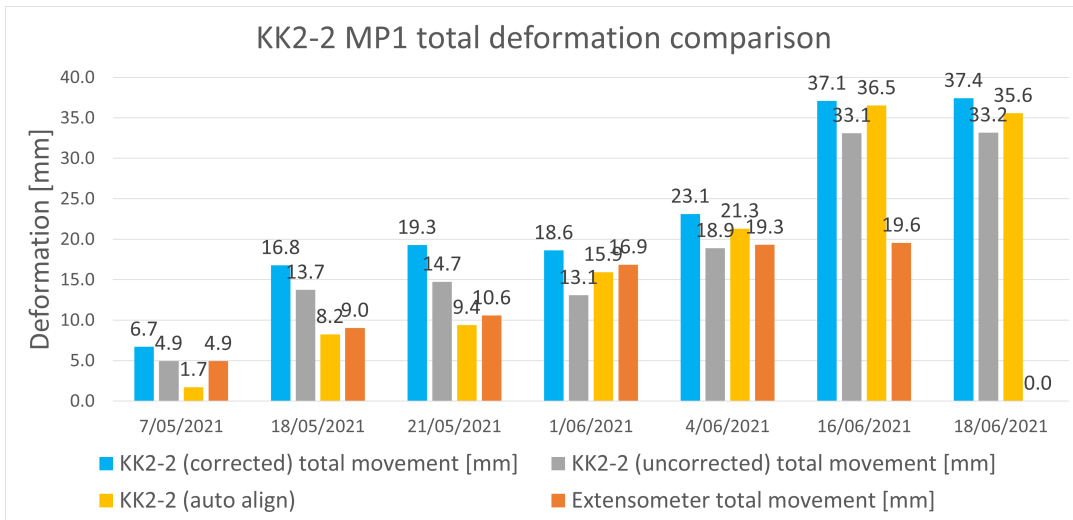


Figure 6.44: Comparison of LiDAR total deformation results vs tape extensometer results at KK2 location 2, measurement point 1.

Inspection of the results obtained from Figure 6.45 show that all of the LiDAR results follow a similar trend that closely resembles that of the tape extensometer. The manually corrected data shows most similar results to the tape extensometer measurements, but as mentioned previously, this correction is very subjective. Therefore, it is more important to focus on the raw and auto aligned data. In this case, the auto aligned data performs better than the uncorrected (raw) data. The trend is relatively closely resembling that of the tape extensometer, with a difference of up to 1.3 mm/day at most, which is still too much on a daily basis to obtain accurate results.

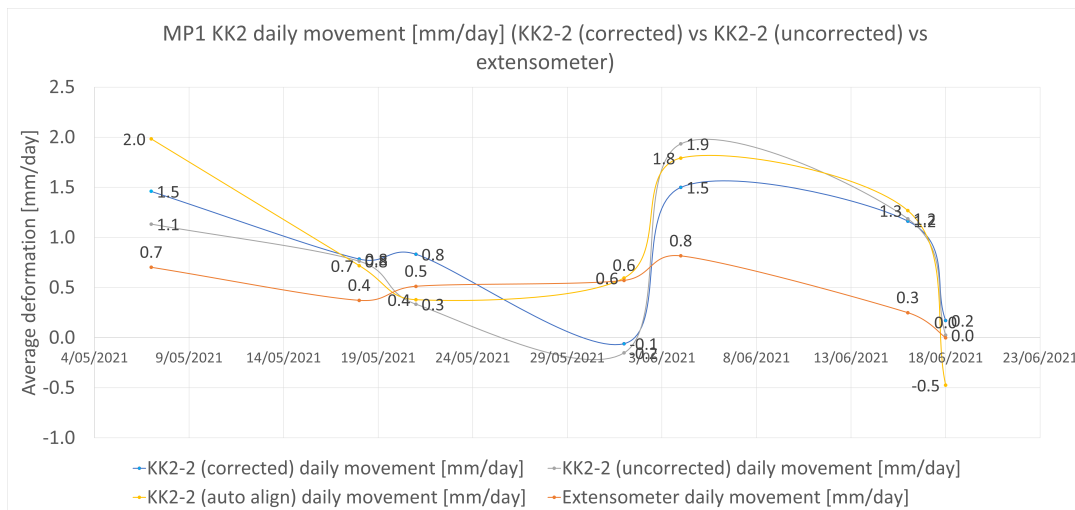


Figure 6.45: Comparison of LiDAR daily average deformation vs tape extensometer results at KK2 location 2, measurement point 1.

In Figure 6.46 the total deformation measured at measurement point 2 is shown. This measurement point has only been measured for 2 weeks, because after that moment, this part of the room was filled with waste rock. The manually corrected scan data is performing better than the other two compared to the tape extensometer.

The total deformation measured by the GML equipment is very similar to that of the tape extensometer, however, it must be noted that there is a discrepancy in the deformations observed in both walls again. One of the walls is again exhibiting negative movement, while the other one shows positive deformation. Since the outward movement of the wall is physically impossible, unless shotcrete was removed by mining equipment for example, the results are unrealistic.

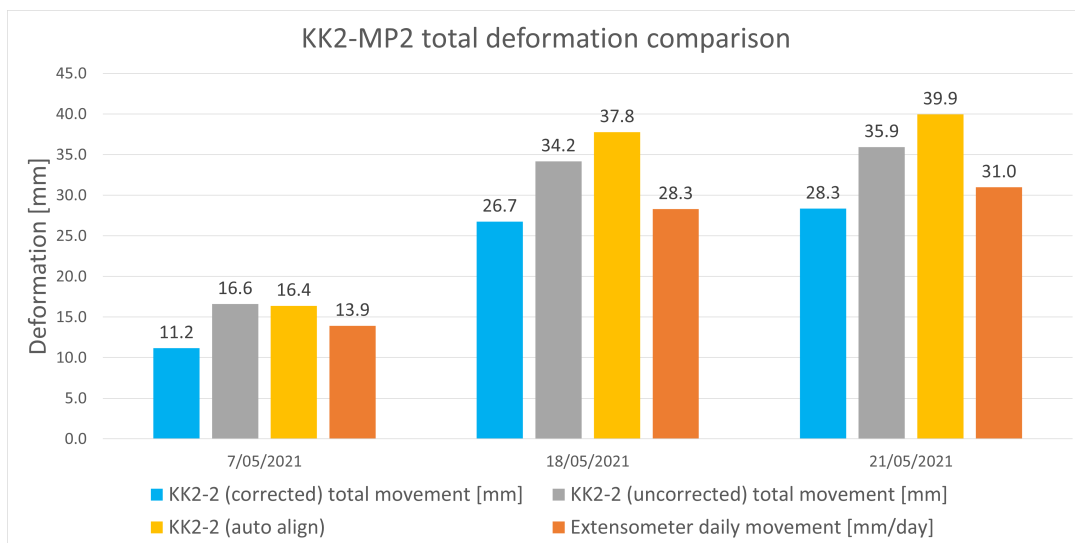


Figure 6.46: Comparison of LiDAR total deformation results vs tape extensometer results at KK2 location 2, measurement point 2.

When analyzing the average daily movement at measurement point 2, all 4 analyses show a similar trend. In particular, the automatically aligned dataset is showing similarities to the tape extensometer results. Based on all 3 measurement points, the auto alignment option gives the best results in this particular measurement setting. However, this measurement point only includes limited data and is therefore not deemed as reliable as the other results.

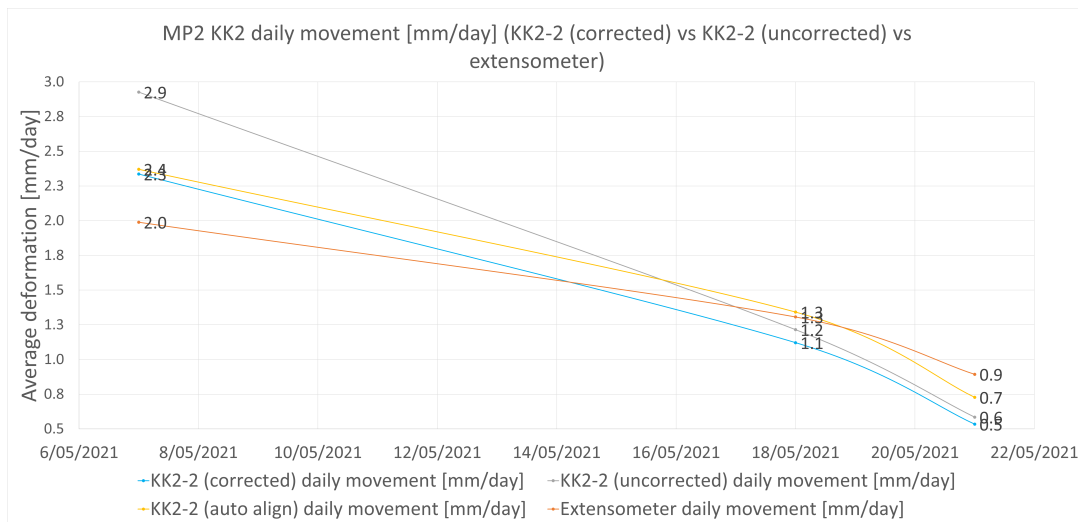


Figure 6.47: Comparison of LiDAR daily average deformation vs tape extensometer results at KK2 location 2, measurement point 2.

When comparing the auto alignment to the raw data with respect to the total deformation results and the daily average results, the uncorrected data shows a more consistent resemblance to the tape extensometer measurements than the automatically aligned data. After consultation with GroundProbe and analysis of the results, it became clear that the automatic alignment algorithm currently has some limitations. Therefore, the raw data was used for the remainder of this study where the geological LiDAR data is compared to the deformation data.

6.2.3 Room KK3

In the third room of interest, KK3, a number of deformation scans and tape extensometer measurements have been conducted as well over the timespan of 5 weeks. In order to remove the subjective aspect of manual corrections, only the raw LiDAR data as well as the automatically aligned LiDAR data are compared to the tape extensometer results.

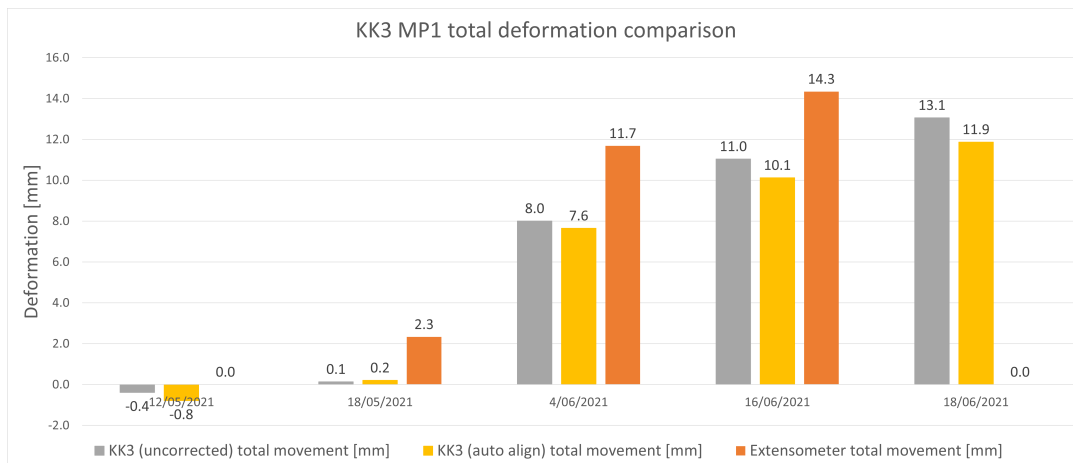


Figure 6.48: Comparison of LiDAR total deformation results vs tape extensometer results at KK3 location 1, measurement point 1.

The total deformation observed at measurement point 1 in room KK3 is shown in Figure 6.48. The measurement period ranges from 13/05/2021 until 18/06/2021 and shows the development of the results over time. The results at this measurement point shows that the raw LiDAR data is able to provide similar deformation observations compared to the tape extensometer measurements.

The auto alignment method is showing different results from both the raw data and the tape extensometer data, but the difference is not big. The auto align method seems to provide insight in what is happening, but it may not be as correct as the raw data in this case.

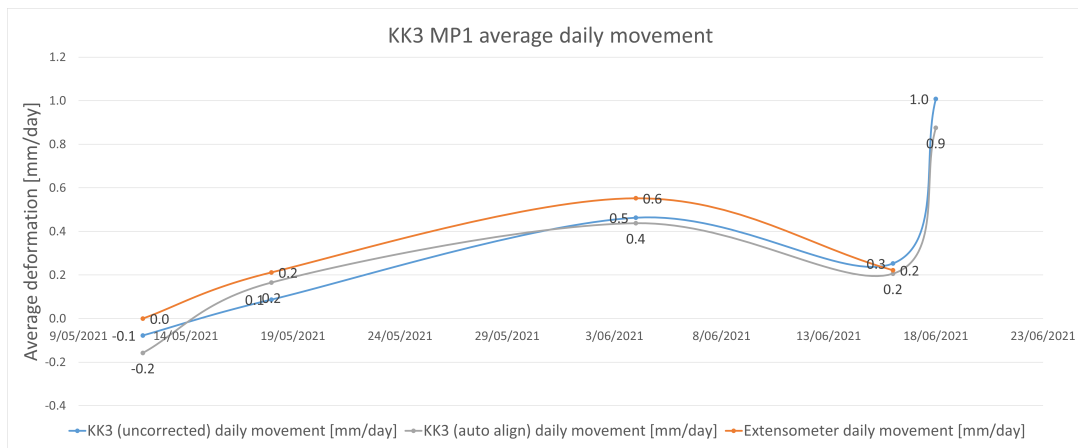


Figure 6.49: Comparison of LiDAR daily average deformation vs tape extensometer results at KK3 location 1, measurement point 1.

The trend that is observed when looking at the average daily movement of the rock mass is shown in Figure 6.49. Both LiDAR datasets show close resemblance to the deformation measured with the tape extensometer. Something to note is that the tape extensometer initially shows some acceleration in the first measurements, but then finally the rock mass slows down.

This is not observed in the LiDAR data, this data shows signs of significant acceleration towards the end of the measurement period. This can be a result of an accuracy limitation, because the last 2 measurements were only 2 days away from each other. This would suggest that the error of this measurement amounts to at least $1.0 * 2 \text{ days} = +2 \text{ mm}$ and is assumed to be incorrect, when comparing it to the overall deformation trend.



Figure 6.50: Comparison of LiDAR total deformation results vs tape extensometer results at KK3 location 1, measurement point 2.

The total deformation observed at measurement point 2 is shown in Figure 6.50. The results at this measurement point are limited, due to blocking of mining machinery at the time of measuring and/or limited visibility due to mining activity. The general trend is however again that the raw LiDAR data provides some insight in how the tunnel develops over time.

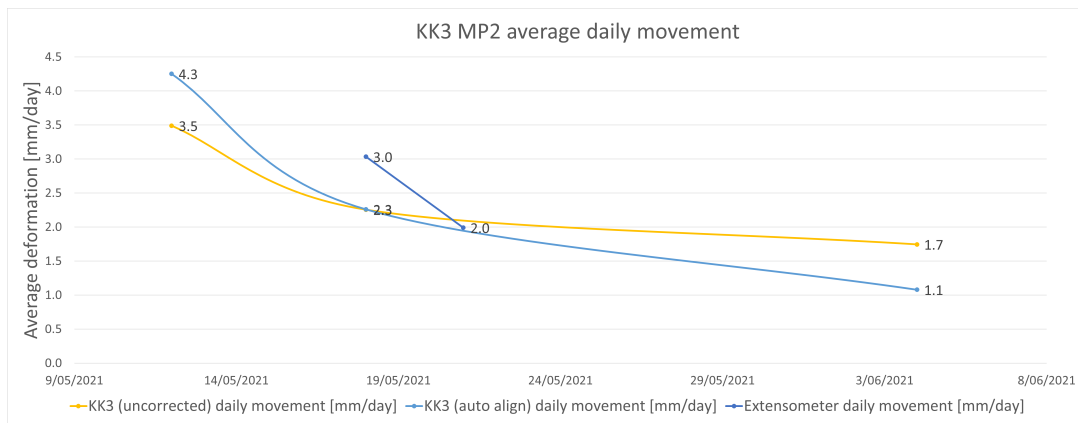


Figure 6.51: Comparison of LiDAR daily average deformation vs tape extensometer results at KK3 location 1, measurement point 2.

The daily average deformation rate at this measurement point was therefore difficult to analyze. The data is limited, but the general trend can be visualized. It then becomes clear that the tape extensometer results also show the decrease of movement in the rock mass in the data that is available. Due to the limited data, it is difficult to draw any conclusions from the results of this measurement point.

In room KK3 there have also been some regions in the tunnel that had to be covered in new shotcrete due to the old shotcrete breaking as a result of too high pressure from the rock mass. The addition of new shotcrete is clearly visible on a GML scan, as illustrated in Figure 6.52 and in Figure 6.53.

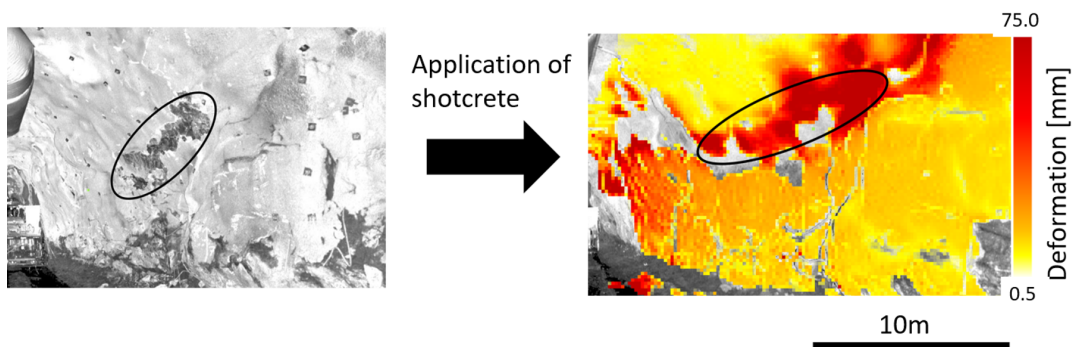


Figure 6.52: Figure illustrating LiDAR deformation data in room KK3 before and after shotcrete application.

The application of the shotcrete is clearly visible on the deformation data that is obtained through the LiDAR measurements. It should therefore be possible for the user to map the thickness of the shotcrete by conducting a deformation measurement shortly before and after the application of the shotcrete. This can provide valuable insight in how consistent an operator is able to achieve certain thickness levels.

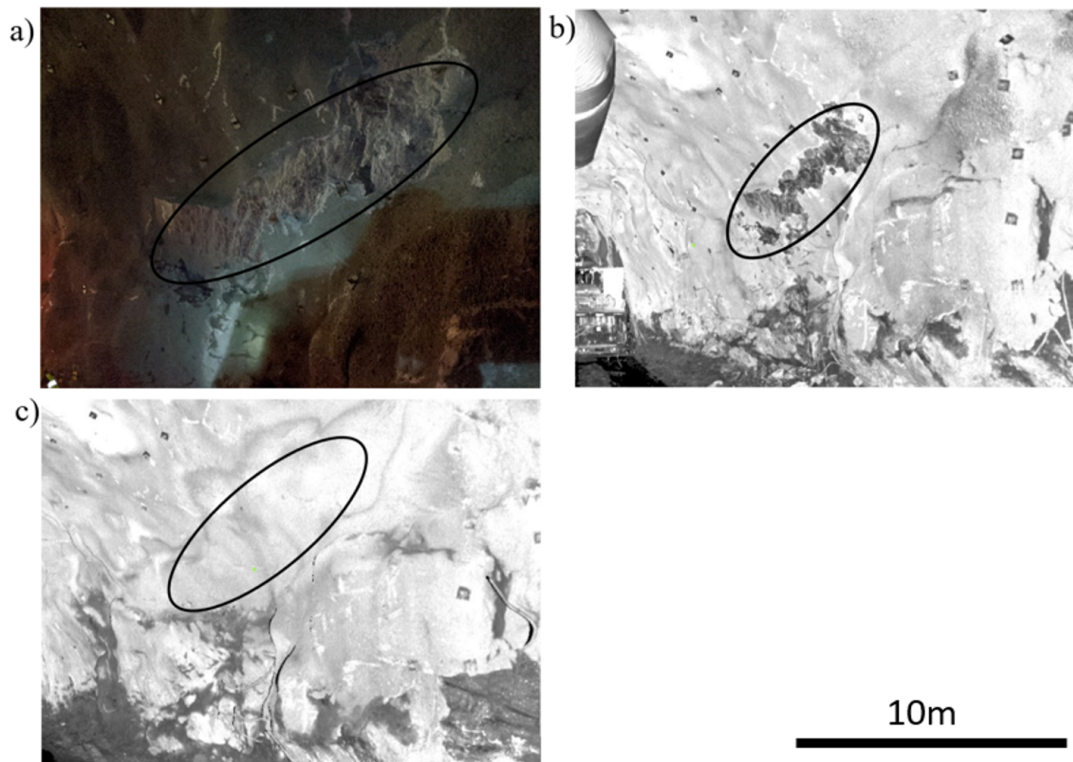


Figure 6.53: Figure illustrating shotcrete application with LiDAR data. a) RGB Image of the damage in the wall. b) LiDAR data of the damage in the wall. c) LiDAR data of the damage after shotcrete application.

Figure 6.53 shows the comparison between the damaged area without new shotcrete applied (a), the LiDAR image obtained from a deformation scan which provides a very clear greyscale image of the subsurface (b) and a LiDAR image obtained from the deformation scan straight after application of the shotcrete, also in greyscale (c).

The image shows the potential of the use of LiDAR technology to visualize changes in the subsurface environment with limited lighting. The images are sharp and are hard to distinguish from regular RGB images, when those are visualized in greyscale. This can prove valuable insight in the deformation of the tunnel as well as dimensional changes.

6.3 CONTINUOUS MEASUREMENTS: KK2

The continuous measurements have been processed and visualized in GroundProbe's SSR-Viewer. The majority of the movement detected during the measurements was observed in and around the face, as expected based on (Lato and Diederichs [2014]) because a blast was conducted shortly before the experiment was carried out.

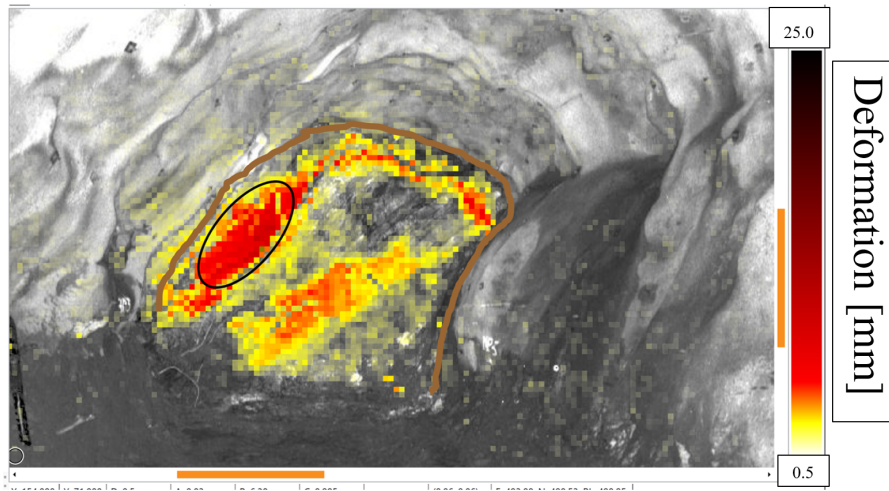


Figure 6.54: Figure illustrating the LiDAR deformation data in the direction of the face during the continuous measurements (with prisms). Brown delineation shows where the shotcrete starts and the area covered within the black circle shows the greatest deformation.

In Figure 6.54 the results of the movement in the face at the end of the 6 hours of the continuous measurements are shown. As expected, most movement is identified in the waste rock on the hanging left wall and in the roof. The area encircled by the black circle has shown the most deformation during the measurements, with a maximum of 13.4 mm. As seen in the deformation graph over time as shown in the top left in Figure 6.54, the deformation was fairly gradual with no sudden accelerations observed.

This means that if this deformation would continue for a full 24 hours at this same rate, a total of $(13.4/6) * 24 = 53.6$ mm would be seen. However, as explained before in Figure 2.1a, the movement is expected to slow down over time. This trend can also be seen in the graph in the top left of Figure 6.54, there seems to be a deceleration after some time at the end of the measurements. The graph is slightly curved towards a more stable deformation rate.

For comparison, the data has also been processed targetless (so without the use of the prisms). Since this measurement was continuous and the notch of the tripod was kept in the same direction, this is expected to give the most reliable targetless results (GroundProbe [2021b]).

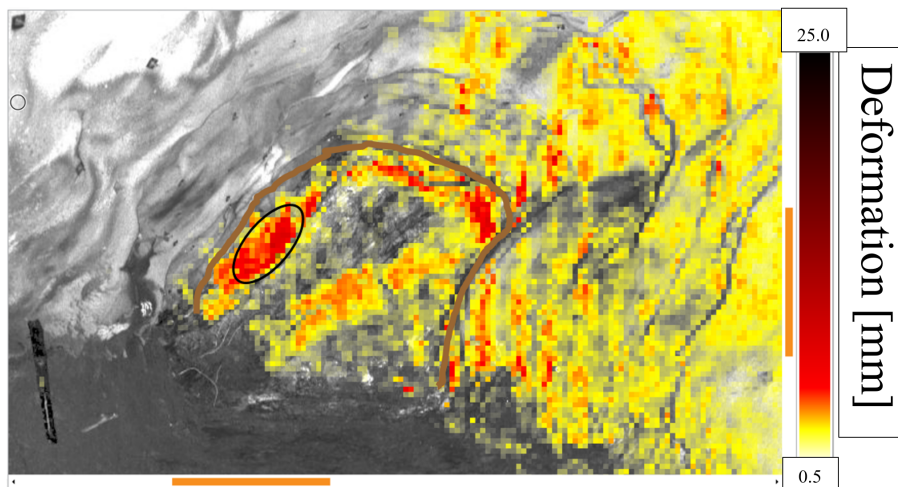


Figure 6.55: Figure illustrating the LiDAR deformation data in the direction of the face during the continuous measurements (without prisms). Brown delineation shows where the shotcrete starts and the area covered within the black circle shows the greatest deformation.

As can be seen in [Figure 6.55](#), a similar deformation pattern was observed in the face when processing the data without the prisms. When looking closer into the data, the maximum movement observed was only 10.2 mm. This is a difference of $13.4 - 10.2 = 3.1$ mm, or 23%. Such a big difference in continuous measurements gives the impression that either the prisms have moved too much in the 6 hour timespan to obtain accurate results or that the accuracy of the targetless measurements is not yet high enough to provide a detailed understanding of the movement in the rock mass.

When looking at the rate of deformation and assuming the deformation is consistent over time, this would result in $(10.2/6) * 24 = 41.0$ mm movement in 24 hours. Compared to the previous 53.5 mm, this is a big difference of 23.4% again. However, it must also be noted that the general movement pattern of the deformation has remained almost entirely the same when processing the scans without prisms. There is still a deceleration at the end of the measurements, which gives reason to believe that the rock is stabilizing after some time.

It has also been observed that the targetless scan registers significantly more movement in the right (foot) wall. At some points that are coloured dark red, movement of up to 5.0 mm was detected, whereas the same region in the scan with the prisms shows a movement of 0.6 mm.

When comparing the two different LiDAR processing results, it has become clear that there are some significant differences. The 3D representation of the deformation data is shown in [Figure 6.56](#).

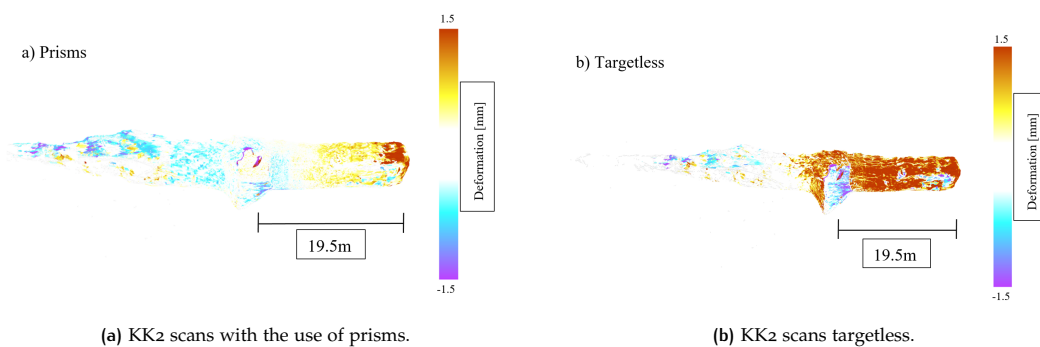


Figure 6.56: LiDAR scan result from continuous measurements in KK2 showing positive and negative deformations. (a) KK2 scans with the use of prisms. (b) KK2 scans targetless.

When comparing [Figure 6.56a](#) to [Figure 6.56b](#), it becomes immediately clear that the deformations measured in the walls is much higher when processing the scans targetless than with the use of prisms. This is due to the fact that when the algorithm of the scanner detects a movement, it uses targets to apply a correction to the deformation in order to make it relative to the original position ([GroundProbe \[2021b\]](#)). Without the use of targets, the algorithm can not apply such a correction and therefore every deformation that is measured will be more strongly visible. This can be seen in more detail when coloring the scans on a positive deformation color scale.

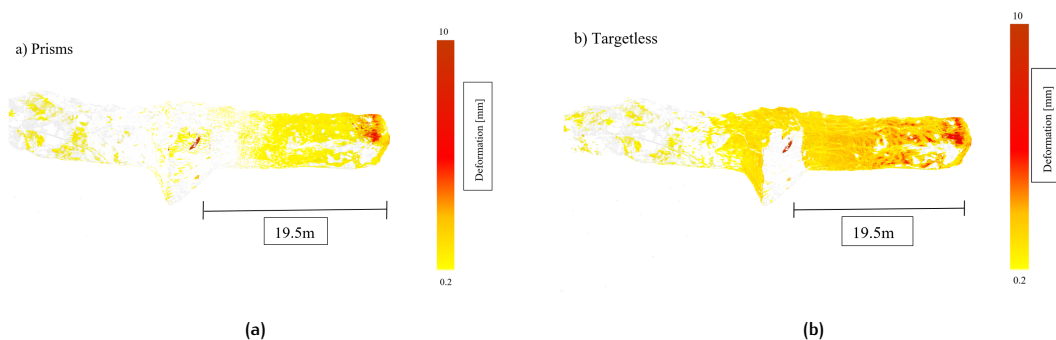


Figure 6.57: LiDAR scan result from continuous measurements in KK2 showing positive deformations. (a) KK2 scans with the use of prisms. (b) KK2 scans targetless.

[Figure 6.57](#) shows the results on a scale from 0.2 to 10 mm. When comparing the use of prisms to the targetless results in these two images, it was observed that the deformations from the targetless measurements are higher judging by the more present orange to red colors seen in the face and in the walls in [Figure 6.57b](#).

Moreover, measurements with the tape extensometer have been conducted to get a better understanding of the accuracy of the GML equipment w.r.t. the tape extensometer. The results are presented in [Figure 6.58](#).

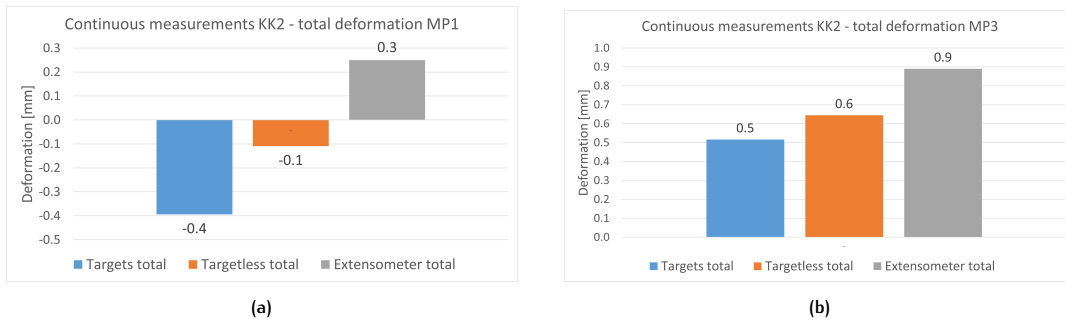


Figure 6.58: Visual representation of LiDAR convergence vs. Tape Extensometer measurements. (a) Deformation at measurement point I (b) Deformation at measurement point III.

From Figure 6.58a can be seen that at Measurement Point I (MP_1), the results of both the scans with the use of prisms as well as the targetless scans are showing a deformation that is negative, whereas the tape extensometer measurement has shown a positive deformation of 0.3 mm. Since the walls are expected to converge towards the centre of the tunnel, it is safe to assume that the tape extensometer results are valid in this case.

However, there is no clear explanation for the negative movement of the walls measured by the GML. It can be due to accuracy limitations that the scanner has a slight error in this measurement and is therefore unable to detect the 'true deformation' measured by the extensometer.

In Figure 6.58b can be seen that the results for Measurement Point III (MP_3) seem to be more promising for both with and without targets. The tape extensometer result shows a total deformation of 0.9 mm at MP_3 , which was closer to the face than MP_1 and thus expected to show more blast-induced deformation. Both the results of the scans with prisms as well as the targetless ones show a positive deformation here. The results in this location have shown to be more promising than those at MP_1 . The results with the use of targets differ only $0.9 - 0.5 = 0.4$ mm w.r.t. the tape extensometer results.

6.4 THE INFLUENCE OF THE GEOLOGY ON THE DEFORMATION

In this section, the link between the structural geology and the lithologies present with respect to the observed deformations are discussed. At first, the geometry and geology of the tunnel is discussed.

The ore is generally stronger than the waste rock in the Kristineberg mine. The waste rock is softer and thus more amenable to deformation than the ore so more deformation is expected on both sides of the ore where the waste rock is located.

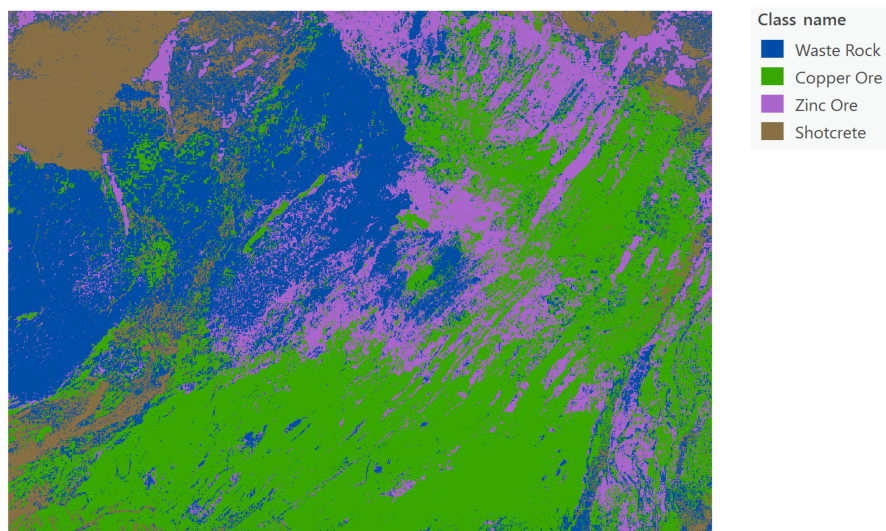


Figure 6.59: The image classification result after applying a SVM deep learning algorithm to the RGB image of the face scanned during the continuous measurements.

Image analysis by means of the SVM algorithm in ArcGIS illustrates the different litho-types present in this face. As can be seen in Figure 6.59, there are a total of 4 litho-types observed in this case. Namely, the waste rock on the left wall is clearly identified, the copper/zinc ore in the centre dipping from the bottom left to the top right and finally some shotcrete is identified.

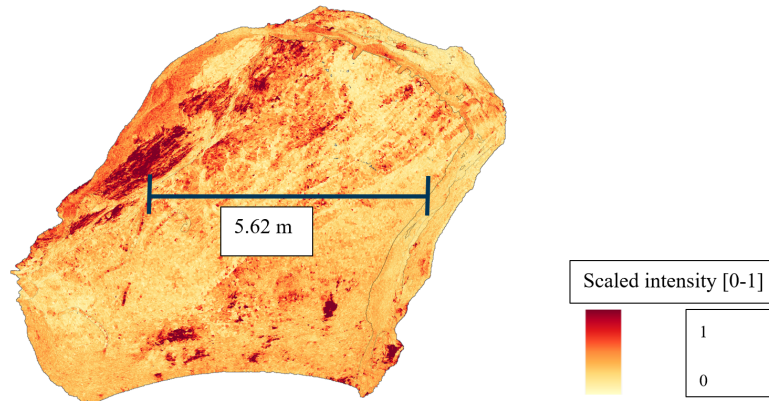


Figure 6.60: Image showing the LiDAR data based on varying intensity levels in the face scanned during the continuous measurements.

Figure 6.60 shows the LiDAR data based on the intensity levels measured by the GML. As can be seen, there is a similar pattern visible when comparing this image to Figure 5.12. The generally lighter waste rock shows a higher intensity on the LiDAR data versus the ore rock.

Therefore, a clear distinction can be made between the waste rock on the left side and partially in the roof versus the ore in the centre of the image. As explained before in this study, most deformation is expected in the wall and the roof where the waste rock in combination with more unstable conditions are expected to be found.

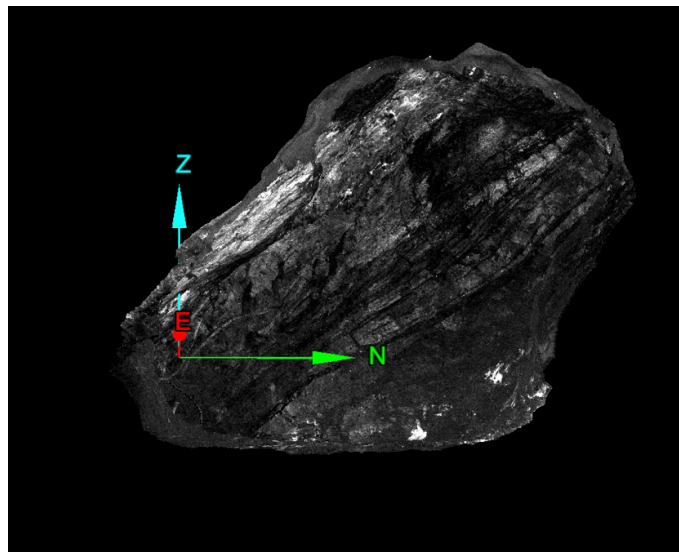


Figure 6.61: The LiDAR scan result of the fresh rock at the face during the continuous measurements.

Figure 6.61 illustrates the image obtained from the LiDAR geological scan of the fresh rock, which shows a similar geological structure as described before. The structural geology was further analyzed by the use of Maptek software, which will be discussed next.

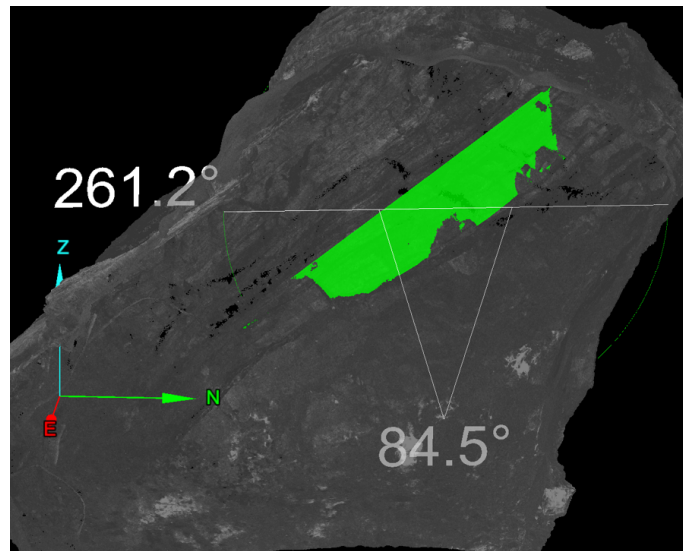


Figure 6.62: Analysis of the structural geology seen in the LiDAR scan result of the fresh rock at the face during the continuous measurements.

The LiDAR scan data was interpreted in Maptek by means of visual inspection and the use of the X, Y and Z coordinates of the pixels. Pixels with identical angles are then grouped together and are shown as one structure. As can be seen in Figure 6.62, the ore in the centre of the face has an orientation of 84.5/261.2/171.0 (dip/dip direction/strike). From Figure 6.63 becomes clear that the waste rock in the left wall shows an approximately similar structure throughout the entire wall with angles of on average 40.5/190.4/100.5. Not enough data could be acquired from the right wall to analyze the structures, due to occlusion of the laser beam.

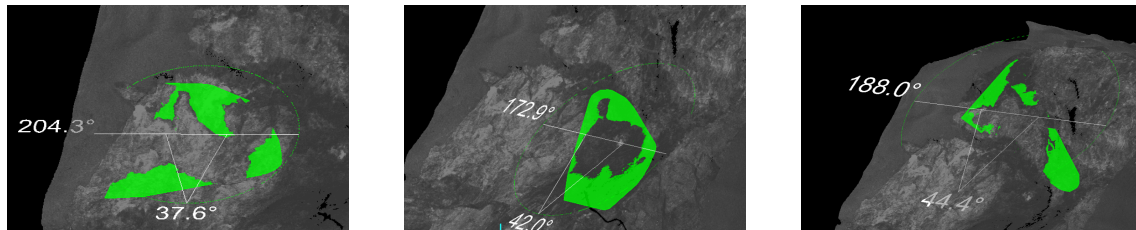


Figure 6.63: a) Left wall bottom left, b) Left wall bottom right c) Left wall top.

Finally, the roof shows an overall structure with the following angles: 17.4/331.6/241.2. This structure is seen in all of the roof analyses that have been conducted in this study.

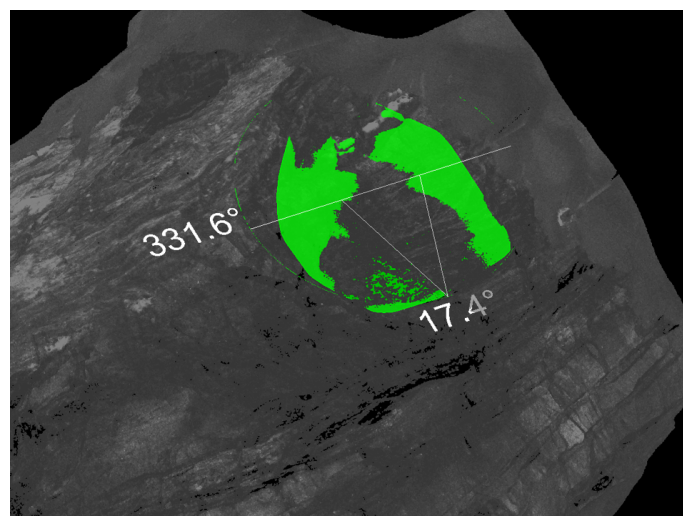


Figure 6.64: Analysis of the structural geology seen in the LiDAR scan result of the fresh rock at the face during the continuous measurements.

As the outer edges of the face showed the strongest deformation straight after the blast, it is hard to say which of these major structures have had any impact on the convergence of the room. The most logical seems that the hanging wall was pushing down on the foot wall, therefore causing the most movement in the hanging wall itself and because of the tunnel being skewed, the roof also deforms with the hanging wall. This eventually pushes the foot wall inwards as well, leading to a positive deformation inwards with respect to the tunnel center.

6.4.1 Blast-Induced Deformation

The blast-induced deformation observed over the timespan of 4 – 7 days in room **KK2** commonly shows a very strong deformation in the roof and in the hanging wall. This data was visualized along with the corresponding geological scans of that particular area of the tunnel. As previously described in [Figure 2.1a](#), the convergence of the tunnel straight after a blast shows a strong deformation in the tunnel.

Then, as time progresses, the tunnel tends to stabilize over time after the stresses in the rock mass have reached an equilibrium ([Lato and Diederichs \[2014\]](#)). The highest deformation is therefore generally measured shortly after the blast, which is also confirmed by the results of this study. When looking at the results, as seen in [Figure 6.65](#), strong deformation (up to 35-40 mm) can be found in the hanging wall and in the roof shortly after the blast over a total of 7 days.

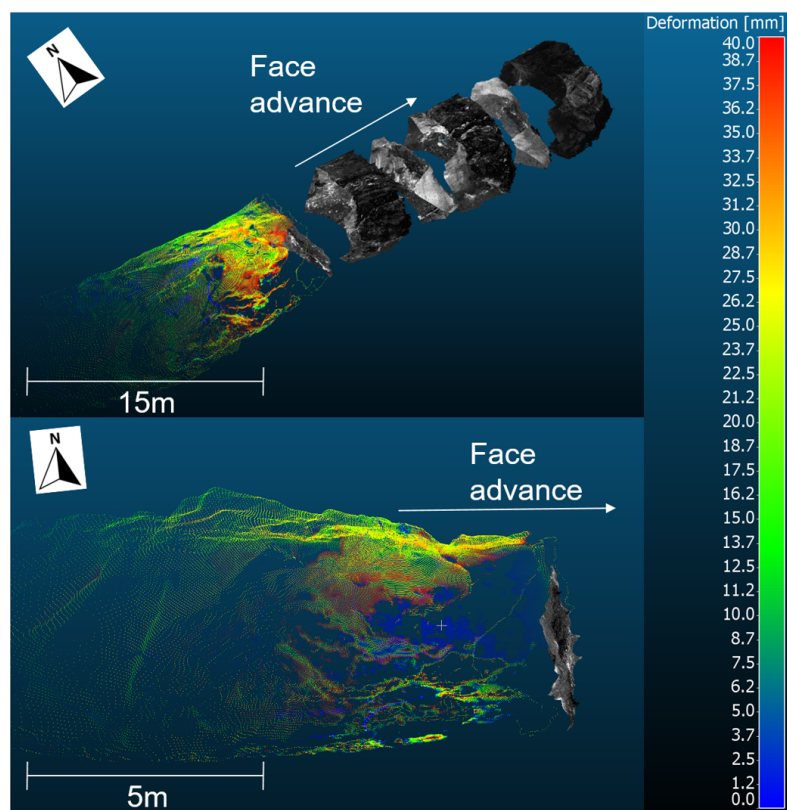


Figure 6.65: Blast-induced deformation in room **KK2** from 23/04 until 30/04 including geology scans.

Then in [Figure 6.66](#) an example of the convergence of the tunnel in the same room over a timespan of the 5 days that follow is shown. A similar pattern can be detected, where the hanging wall of the tunnel converges strongly compared to the rest of the tunnel. However, the deformation is already lower than in the first 7 days.

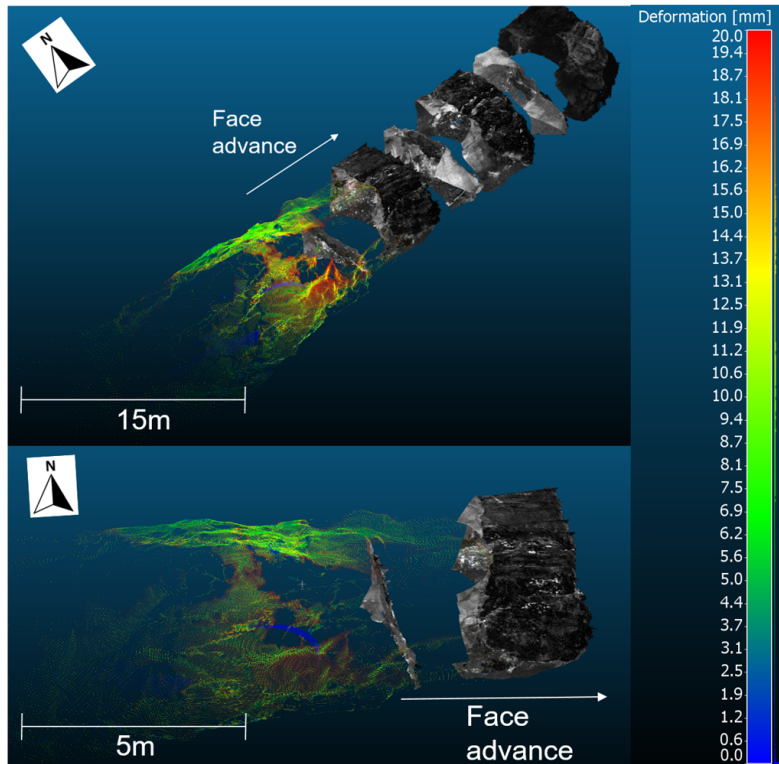


Figure 6.66: Blast-induced deformation in room KK2 from 30/04 until 04/05 including geology scans.

Along with the deformation data, the geological LiDAR scans of the exposed rock surfaces have been visualized in greyscale. There is relatively strong deformation found in the right half of the roof and in the hanging wall on the right. Figure 6.66 includes deformation data up till 04/05 and thus the bottom part of the figure shows only the deformation data along with the corresponding geological scans, namely those of 22/04 and 28/04.

As the tunnel progresses, the blast-induced deformation pattern shows similar results. The deformation between 04/05 and 11/05 is less than previously seen in 7 days as illustrated in Figure 6.65. There is again a stronger convergence observed in the hanging wall, compared to the rest of the tunnel.

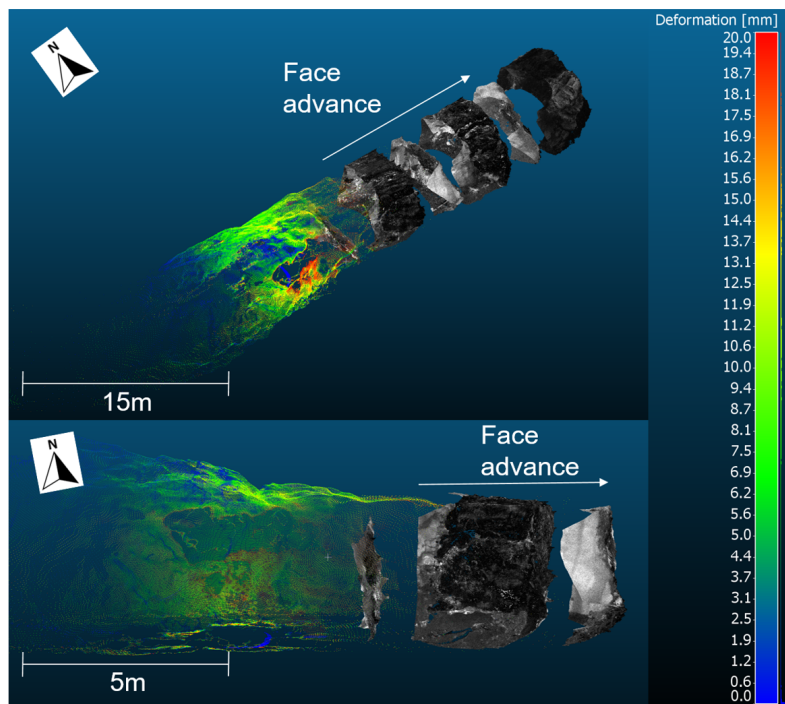


Figure 6.67: Blast-induced deformation in room KK2 from 04/05 until 11/05 including geology scans.

Then at the next stage, when looking at [Figure 6.68](#), the convergence of the tunnel walls is observed mostly in the hanging wall, where the deep red colours indicate deformation of up to 20 mm in merely 7 days. Along with the convergence, the greyscale geological LiDAR scans are visualized again to indicate which lithologies and structural geological structures may have had an impact on the observed deformations.

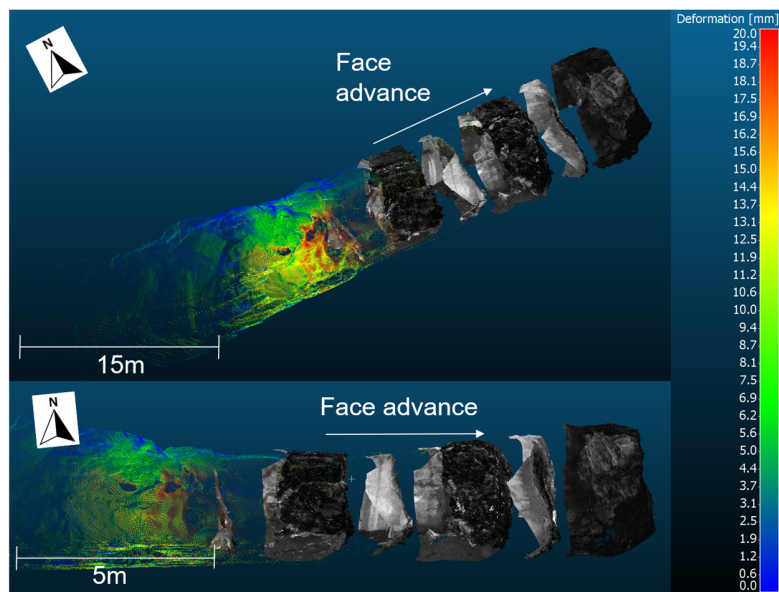


Figure 6.68: Blast-induced deformation in room KK2 from 11/05 until 18/05 including all geology scans.

In order to get an understanding of the large scale geological situation of the scanned area, [Figure 6.69](#) shows the distinction between the foot wall, the ore zone and the hanging wall. This structure is observed in all of the RGB images of the exposed rock surfaces shown in [Figure 6.68](#).



Figure 6.69: Illustration of the geological setting in the face of KK2 on the 28th of April.

From this RGB image can already be seen that the hanging wall is hanging at such an angle that it pushes down on the ore and the foot wall. It is therefore in line of expectations that the hanging wall shows most deformation in the LiDAR deformation scan results. The influence of the geology and the geometry of the tunnel is discussed in more detail in the next sections.

6.4.2 Long-Term Deformation

After some time, the convergence in a tunnel slows down and eventually stabilizes ([Satici and Topal \[2021\]](#)). This same principle was shown in [Figure 2.1b](#). The rock mass reaches an equilibrium and stabilizes eventually. Both the geological scans as well as the deformation scans are georeferenced and visualized in the same window in CloudCompare in order to see the corresponding deformation at the exact location of the analyzed geological scans. An example of this visualization is shown in [Figure 6.70](#).

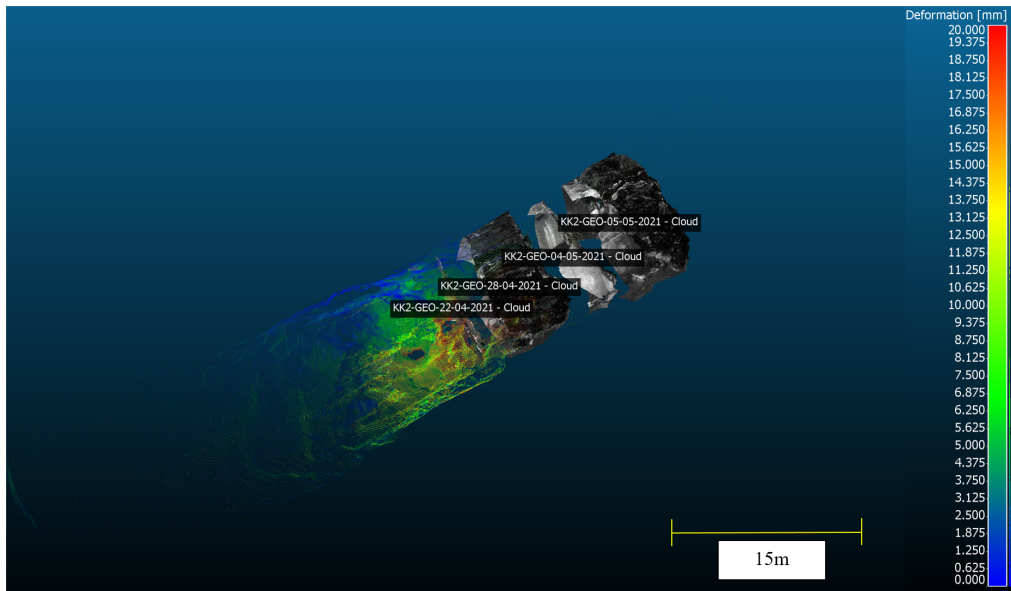


Figure 6.70: CloudCompare visualization of the LiDAR deformation data between 11/05 and 18/05 with geological LiDAR scans coloured in greyscale based on intensity levels.

As shown in Figure 6.70, the point clouds from the geological scans are georeferenced and illustrated at their corresponding locations within the KK2 tunnel. The deformation data shows a relatively strong deformation in the top right of the right wall, which is shown with a red circle in Figure 6.71.

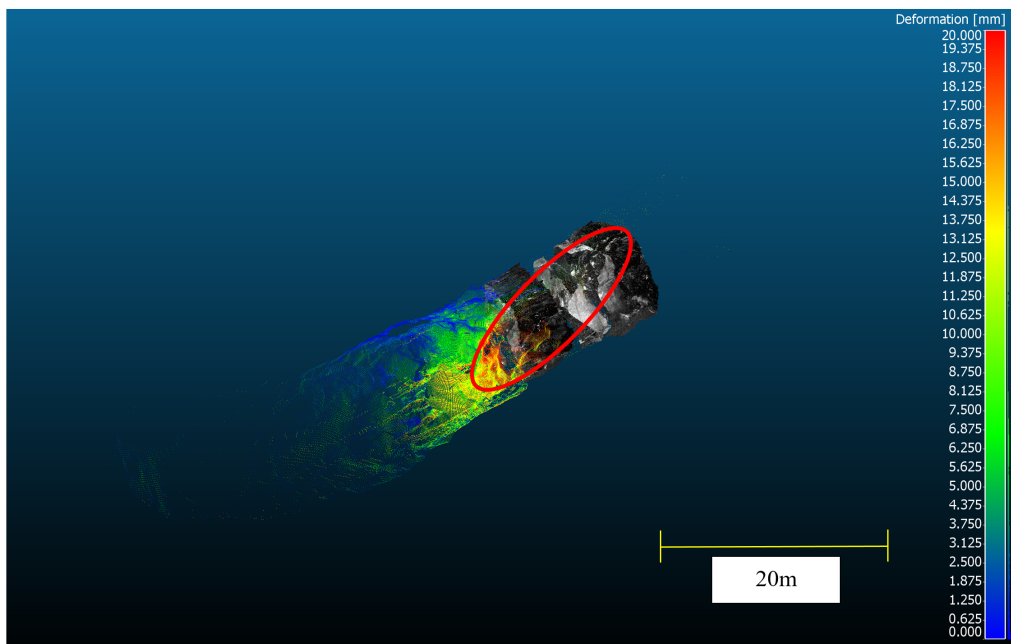


Figure 6.71: LiDAR deformation data with greyscale geological LiDAR scans. Red circle to indicate strong deformation.

The long-term deformation in the left side of KK2 over a timespan of almost 3 weeks is illustrated in Figure 6.72, along with the corresponding geological scans. As can be seen, the hanging wall shows a relatively strong deformation again. As the face advances, the deformation zone that was initially observed as blast-induced, extends along the same area and shows stronger deformation.

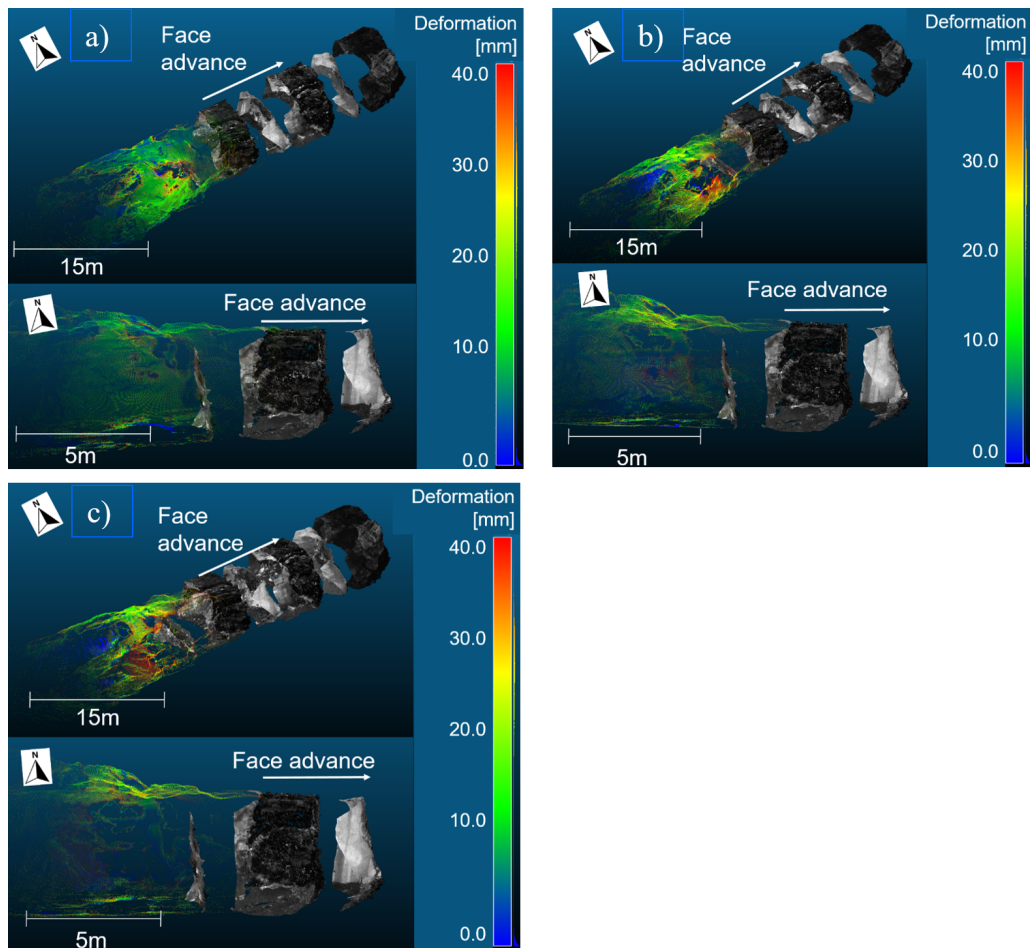


Figure 6.72: Long-term deformation in room KK2 from 30/04 until 18/05 including geology scans. a) Deformation from 30/04 until 04/05. b) Deformation from 30/04 until 11/05. c) Deformation from 30/04 until 18/05.

The largest deformation of up to 40 mm is again found in the hanging wall on the right side of the tunnel. The corresponding geological scans are shown in the sideview in the bottom half of each image. They include the exposed rock surface on 22/04/2021, 28/04/2021 and 04/05/2021.

These geological scans have been analyzed and it has become clear that aside from the hanging wall pushing down on the rocks, the generally weaker waste rock is more prone to deformation, especially when the waste rock is showing heterogeneous mineralogical composition based on the varying intensity levels. The results of the analysis are shown in [Appendix D](#) and [Appendix C](#).

[Figure 6.73](#) shows the long-term deformation in the right side of KK2 over a timespan of again almost 3 weeks, along with the LiDAR geological scans taken in that part of the tunnel. Again, the hanging wall and parts of the roof show signs of significant deformation over time.

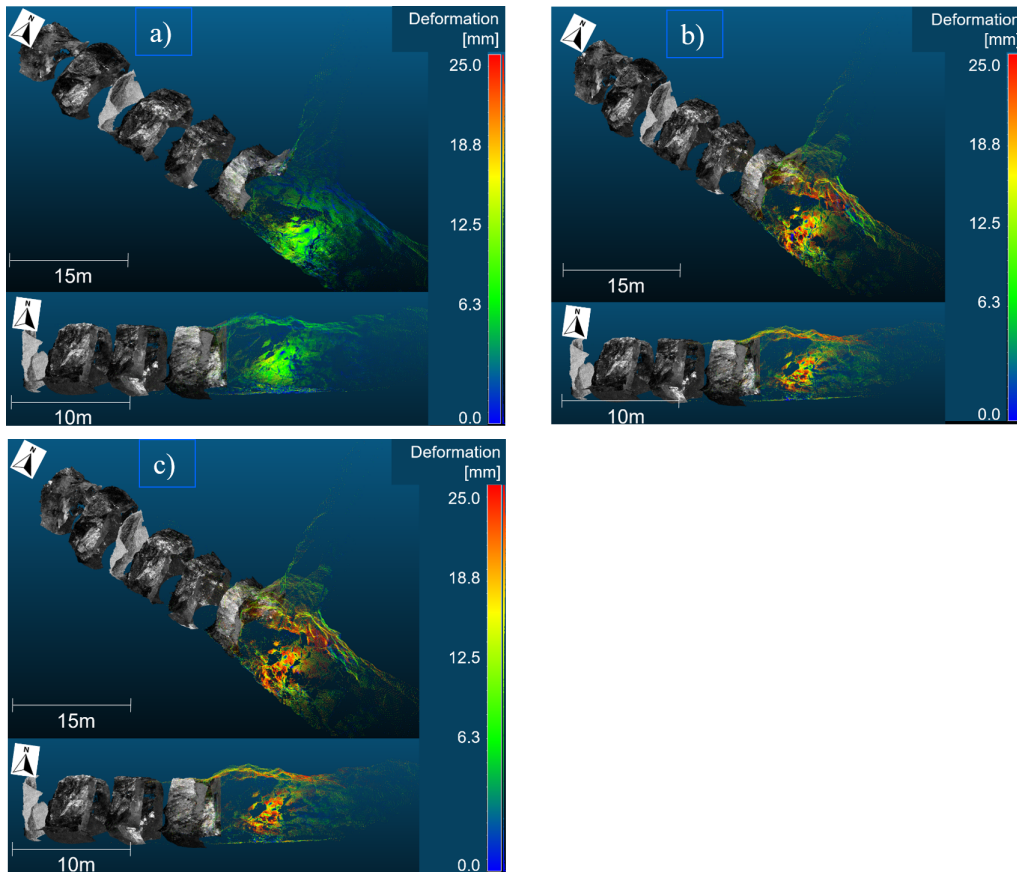


Figure 6.73: Long-term deformation in room KK2 from 01/06 until 18/06 including geology scans. a) Deformation from 01/06 until 05/06. b) Deformation from 01/06 until 16/06. c) Deformation from 01/06 until 18/06.

The largest deformation obtained in this part of the tunnel is approximately 25.0 mm between 01/06/2021 and 18/06/2021 and is found in the hanging wall and in some parts of the roof. The geology scans involved are taken on 22/05/2021, 26/05/2021, 29/05/2021 and 01/06/2021. The remainder of the geological LiDAR scans are analyzed also, to be used as a prediction for future deformation movement.

6.4.3 LiDAR Geology Scans

From the LiDAR scans of the exposed rock surfaces in KK2, it was possible to extract the different intensity levels that were collected from the fresh rock. Based on the varying intensity levels, the data was visualized and clustered into different lithologies. This clustering of the LiDAR data can also be cross-referenced with the supervised SVM classification of the RGB images, which will be discussed in subsection 6.4.4.

An example of the results obtained from the geological scans of the exposed rock surface on 28/04/2021 is shown in the figures below. In Figure 6.74 the raw point cloud data can be seen, along with the elbow plot, the point cloud coloured based on intensity levels as well as the point cloud coloured based on the amount of neighbouring pixel within a set search radius of 5 mm. As can be seen from this image, the pixels closest to the scanner typically exhibit a stronger KDE than those further away. This is in line with what is expected based on the set resolution within the GML equipment, which states that pixels at 10 m distance can be at most 6.3 mm apart from each other, at 20 m distance at most 12.6 mm and so forth.

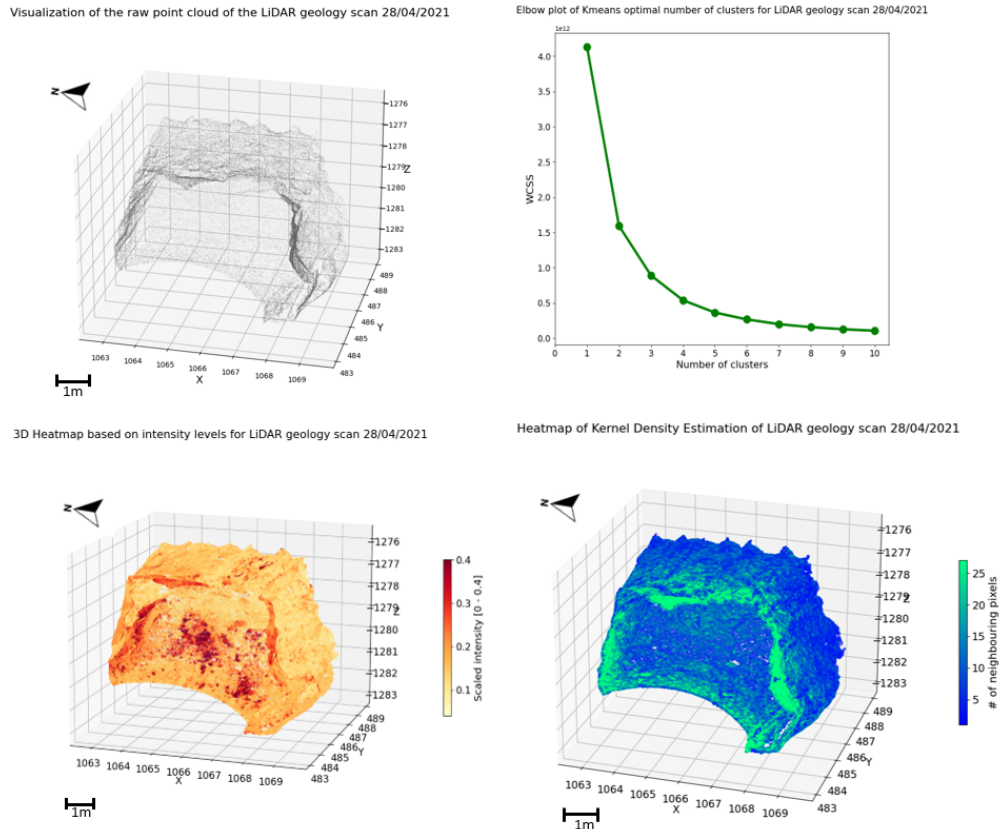


Figure 6.74: 3D Intensity and density visualization using LiDAR geology scan 28/04/2021 [1/3].

Subsequently, the dataset was clustered based on the unsupervised K-means clustering method and for comparison, the two-phased clustering method has also been applied. The obtained result is shown in Figure 6.75 and shows interesting results. Clearly, there is a distinction between both methods for cluster 0 and cluster 1, which is caused by both methods choosing different intensity ranges for the final clustering. However, the green area of interest (cluster 2) shows clear signs of overlap with the SVM results obtained from the RGB image classification, which is discussed in section 6.4.4.

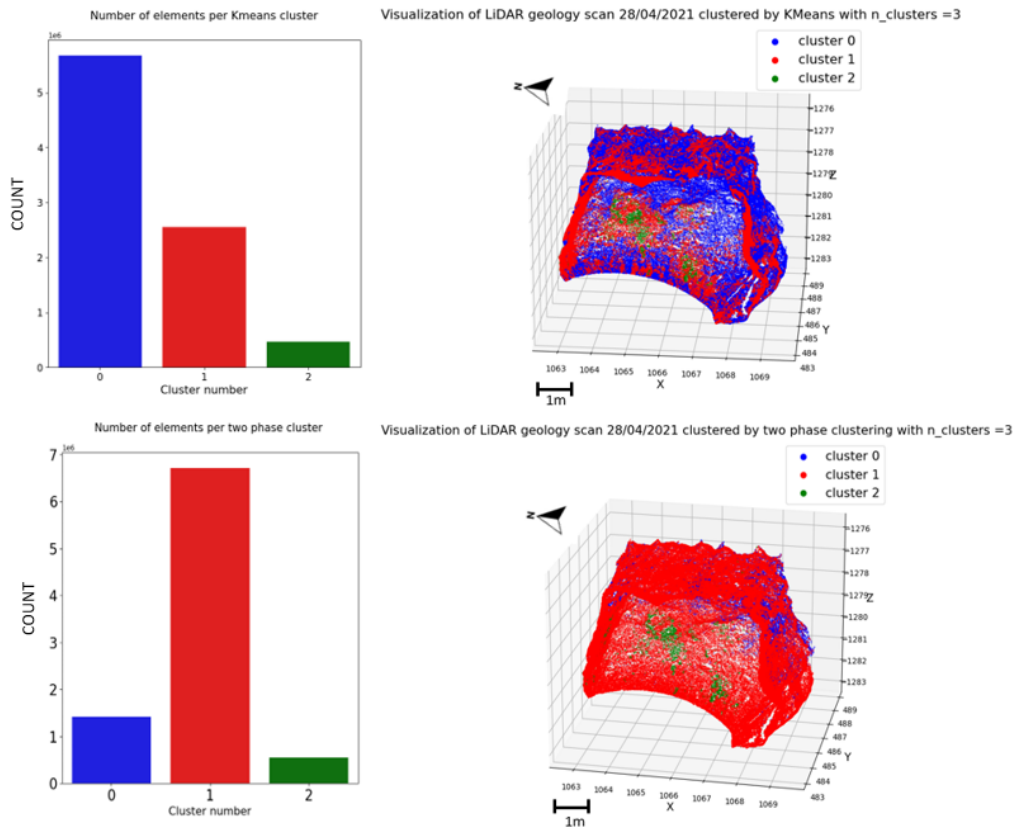


Figure 6.75: 3D intensity clustered data of LiDAR geology scan 28/04/2021 [2/3].

To analyze the differences in both clustering methods in more detail, Figure 6.76 shows the intensity ranges for the different clustering methods. As can be derived from the three figures, cluster 0 in blue and cluster 1 in red are very different in both clustering methods, while cluster 2 (almost) exactly the same. The two algorithms obtain a contrasting correlation in the first two clusters because of the different approach. K-means has typically shown to have a larger cluster 0 intensity range than the two-phased method. This has led to a larger cluster 0 in the K-means method in all of the geological LiDAR data. The characterization of the K-means clustering seems more realistic, after cross-referencing with the supervised SVM classification method.

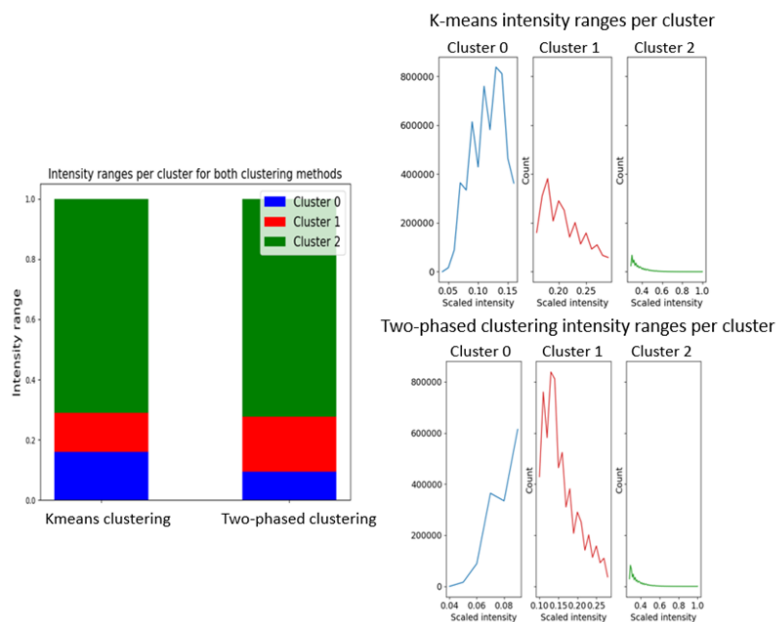


Figure 6.76: Intensity ranges per cluster for both clustering methods of LiDAR geology scan 28/04/2021 [3/3].

Finally, both clustering methods have been visualized not only on 3 separate, homogeneous cluster colors, but also on the 3 separate clusters with transitioning colors within the specified intensity range shown on the left in Figure 6.76. The resulting heatmaps can be found in Figure 6.77 and Figure 6.78. From these type of visualizations, it becomes much more clear where the transitions are between different lithologies and whether they are smooth or very abrupt. These heatmaps have then been used to analyze the relationship between lithologies and deformation structures.

Heatmap of scaled intensity per cluster of LiDAR geology scan 28/04/2021 clustered by KMeans with n_clusters = 3

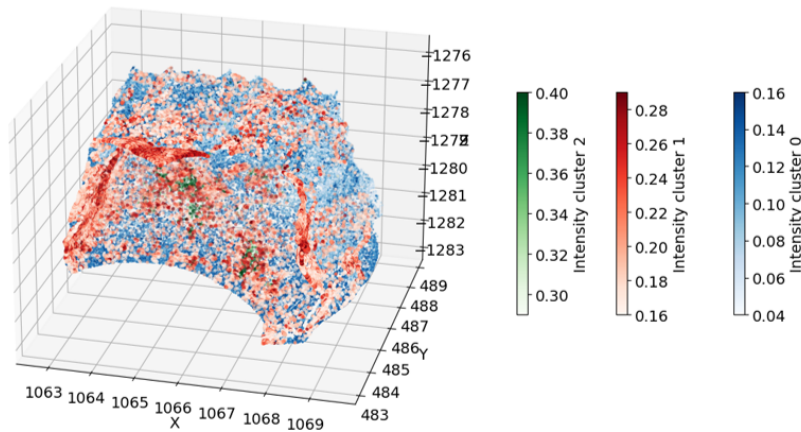


Figure 6.77: Result of k-means clustering with scaled intensity per cluster of LiDAR geology scan 28/04/2021.

From this image it seems that there is a zone with presumably copper ore in the center of the image, when comparing it to the RGB images, which is clustered as cluster 2 in this case. The remainder of the k-means clustering shows a sometimes smooth, sometimes very abrupt change from cluster 2 to cluster 1.

After comparison to the RGB image shown in Figure 6.79, it seems possible that the cluster 1 correlates closely to the zinc containing minerals in this classification.

Heatmap of scaled intensity per cluster of LiDAR geology scan 28/04/2021 clustered by two phase clustering with n_clusters = 3

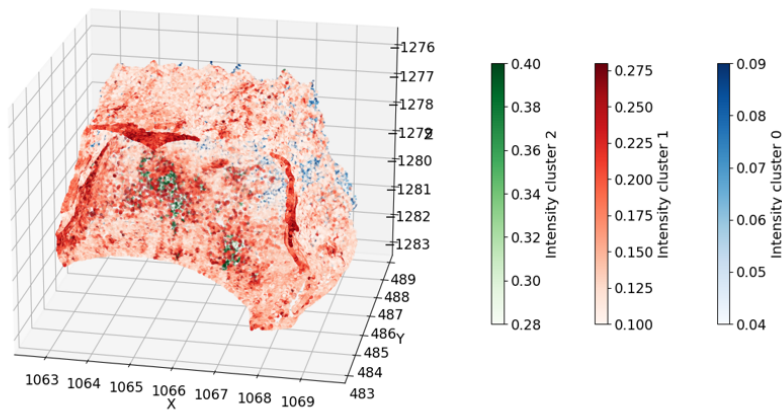


Figure 6.78: Result of two-phased clustering with scaled intensity per cluster of LiDAR geology scan 28/04/2021.

Figure 6.78 shows a different result than the k-means analysis. However, it does become clear that the copper containing minerals in the centre of the face are again properly distinguished from the other minerals. The two-phased algorithm does however seem to perform worse at distinguishing the waste rock from other material, as most of the image is colored red (cluster 1).

6.4.4 RGB geology data

The RGB images have then been analyzed and classified in ArcGIS. A result of the classification of the exposed rock surface on 28/04/2021 is shown in Figure 6.79. This figure illustrates that in the bottom centre, there is mainly copper ore. The rest of the image shows mainly shotcrete and waste rock, with some zinc ore found in between.

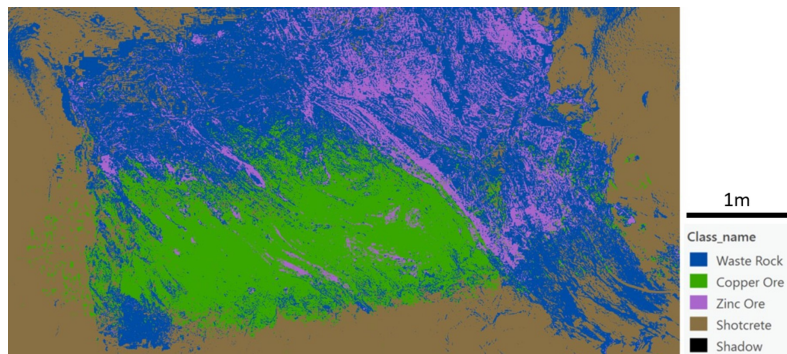


Figure 6.79: Classified RGB image of the exposed rock surface on 28/04/2021.

When comparing the ArcGIS results with the Python analysis, it is observed that the K-means algorithm shows the same distinction between waste rock and (copper) ore. The LiDAR data found in the centre of the face shows higher intensity levels than the surroundings and are found to be copper ore when analyzing the LiDAR geological data in combination with the RGB images.

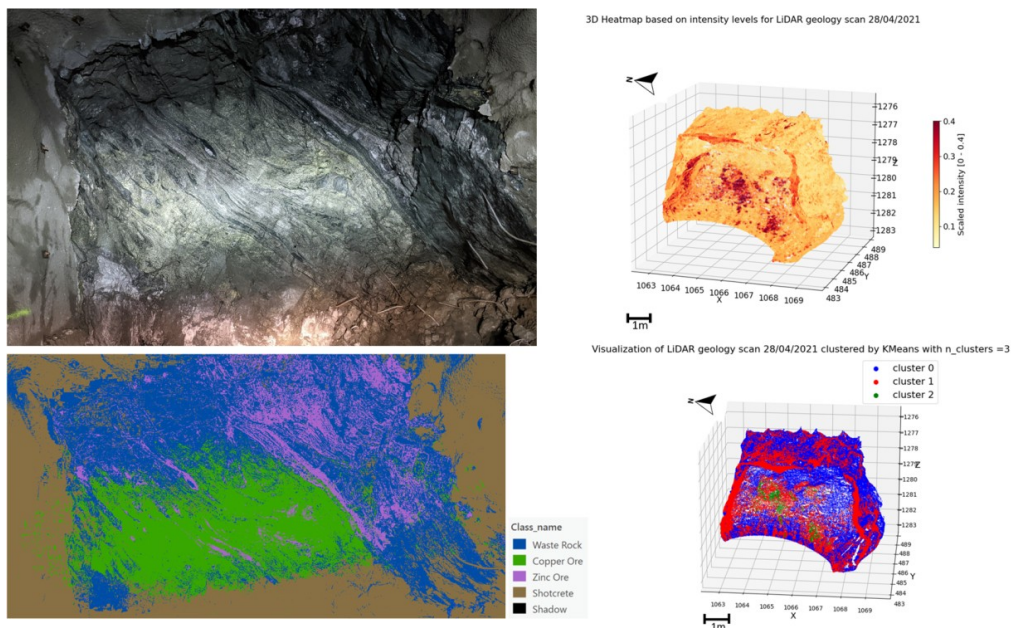


Figure 6.80: Comparison of RGB image analysis to the LiDAR data of the exposed rock surface on 28/04/2021.

When looking at the clustered geological LiDAR data versus the RGB classification, it becomes clear that for example the strong green cluster (cluster 2) is most likely the copper ore in the centre of the face that consists of similar light intensity levels. Then the other two clusters are likely to be mixtures of different waste rock minerals along with some shotcreted areas that seem to be grouped together with dusty regions of the rocks in the red cluster 1.

Upon analysis of all the blast-induced deformations along with the geological data, it becomes clear that the hanging wall generally deforms more than the foot wall or the roof. Additionally, it seems from the python and RGB analysis that the waste rock is more prone to deform than the ore rock, especially when the uniform structure is separated by (zinc) ore.

6.4.5 Strong deformation zones

Certain areas of the tunnel are seen as strong deformation zones. These are the areas in the hanging wall that are showing strong deformation, as explained in subsections 6.4.1 and 6.4.2. What the blast-induced deformation and the long-term deformation results suggest is that the blast-induced deformation and the long-term deformation results suggest is that the hanging (right) wall of the tunnel shows stronger deformations than the rest of the tunnel. It is therefore important to analyze that area in more detail to get an understanding of the root cause of this deformation.

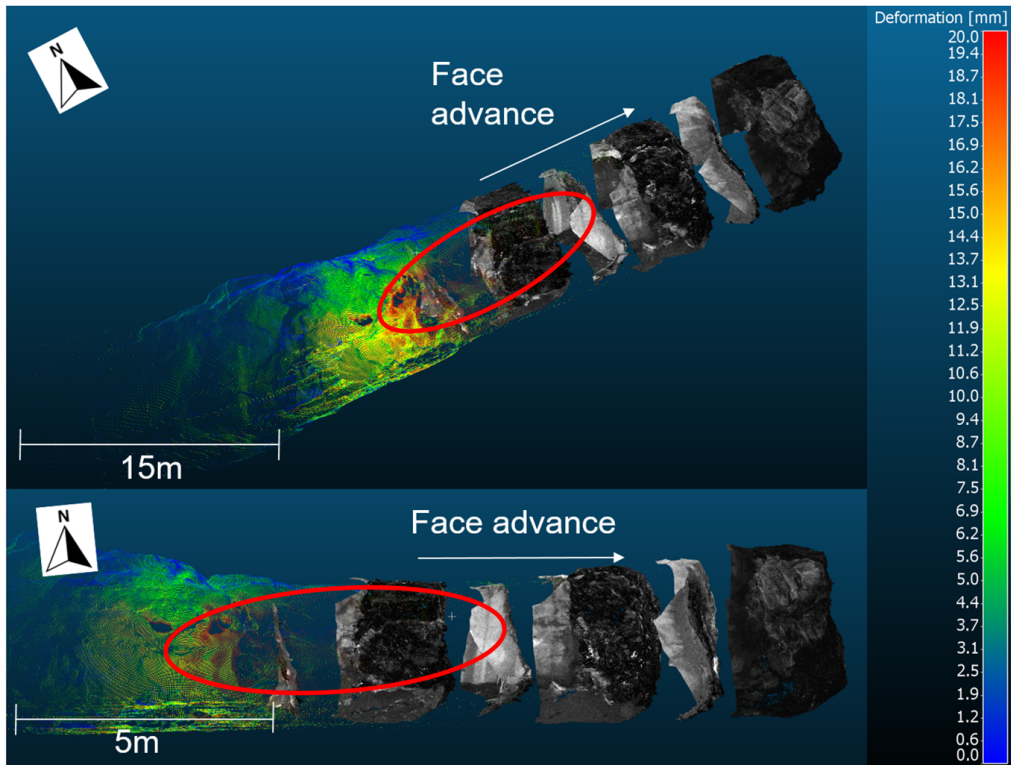


Figure 6.81: LiDAR blast-induced deformation data with red circle indicating strong deformation zone.

Figure 6.81 shows an example of such a strong deformation zone from one of the deformation images shown before. The red circle indicates the zone with relatively strong deformation compared to the rest of the tunnel. The deformation visualization contains zero readings from the exposed rock surfaces up until 05/05/2021, because it shows the blast-induced deformation between 11/05 and 18/05. This zone is analyzed in more detail.

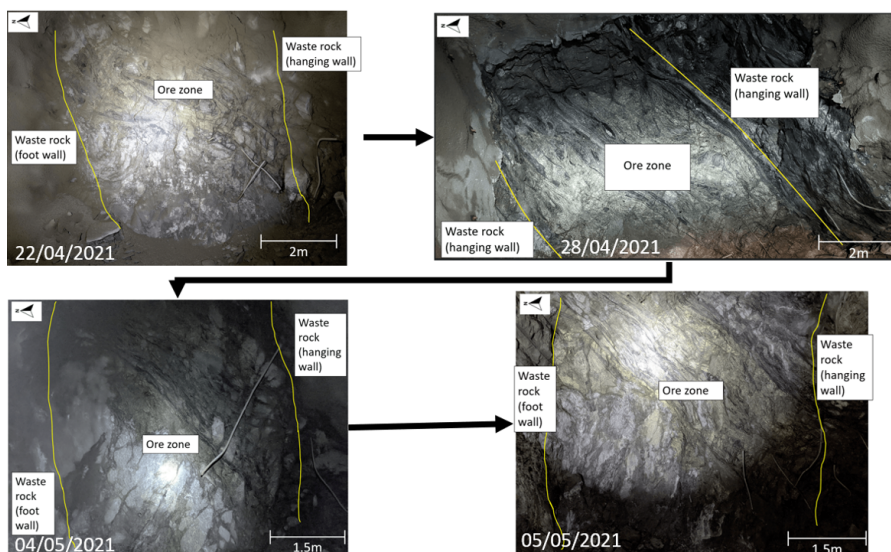


Figure 6.82: RGB images of exposed rock surfaces on set dates (edited to show geological setting).

From [Figure 6.82](#) becomes clear that the hanging wall was commonly covered in shotcrete, but it was always outside the ore zone and therefore consisting (almost) entirely of waste rock. These RGB images have then been classified and compared against the LiDAR geological data.

From that analysis can be concluded that the zone showing the most deformation in the right wall/top right wall consists of waste rock, but also generally the same type of waste rock throughout the deformation zone as it is classified as the same material based on light intensity. Due to very poor light quality and shotcrete, the image from 04/05/2021 is not used in this analysis.

An other result to consider is that the generally weaker waste rock contains traces of zinc ore in the strong deformation zones. These traces cause the uniform structure to be weakened and more easily deformed. The results are shown in [Figure 6.83](#).

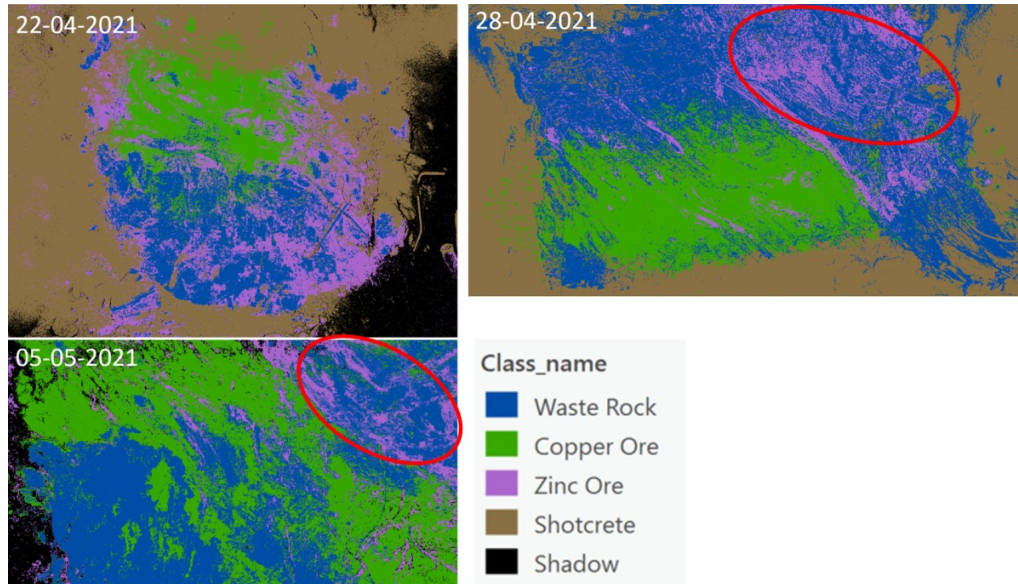


Figure 6.83: Classified RGB images of exposed rock surfaces on set dates.

The red circles in the figures indicate zones that have been classified as waste rock and typically consist of cerussite or schist rock, seem to contain zinc ore also based on the RGB classifications. This interruption of the uniform structure may be a cause for the hanging wall to show stronger deformation. Additionally, the hanging wall is in general pushing down on the foot wall and thus expected to show more convergence in a tunnel.

These same areas have been analyzed from the LiDAR data based on the scaled light intensity results along with the K-means clustering results are shown in [Figure 6.84](#) and [Figure 6.85](#).

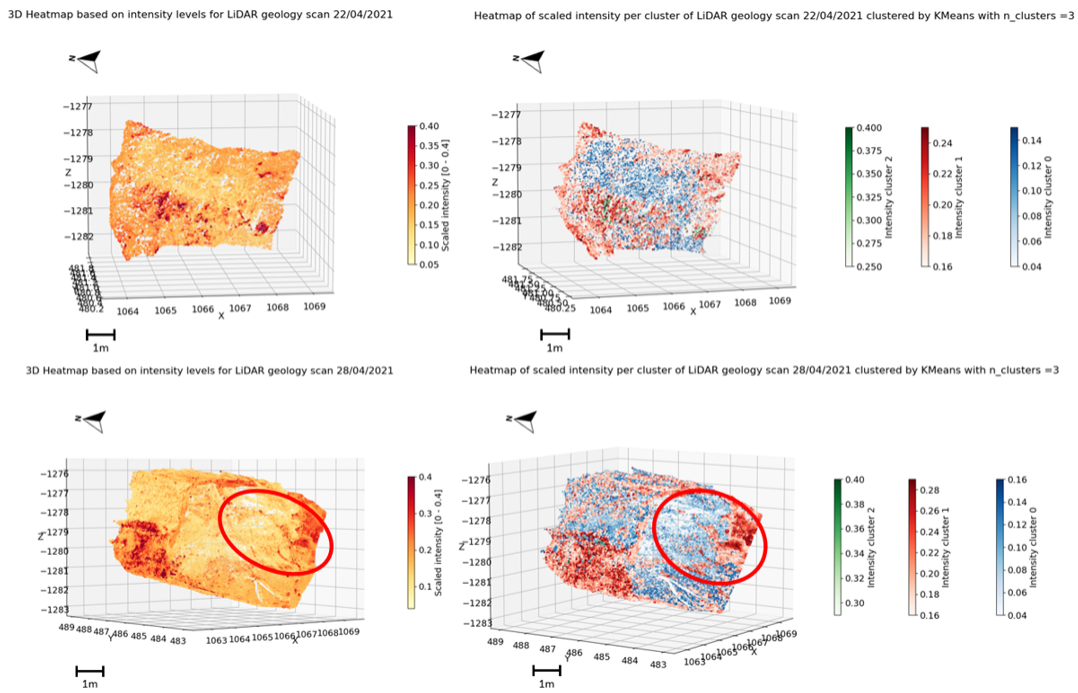


Figure 6.84: Geological LiDAR data of exposed rock surfaces on 22/04/2021 and 28/04/2021.

The strong deformation zones have been highlighted by red circles to illustrate the light intensity levels of those regions along with their clustered results. What can be derived from those images is that there is no strong uniform structure. The intensity shows strong variations which can also be seen in the clustered images. This gives reason to believe that it is a mixture of different minerals that have come together as a very heterogeneous mixture.

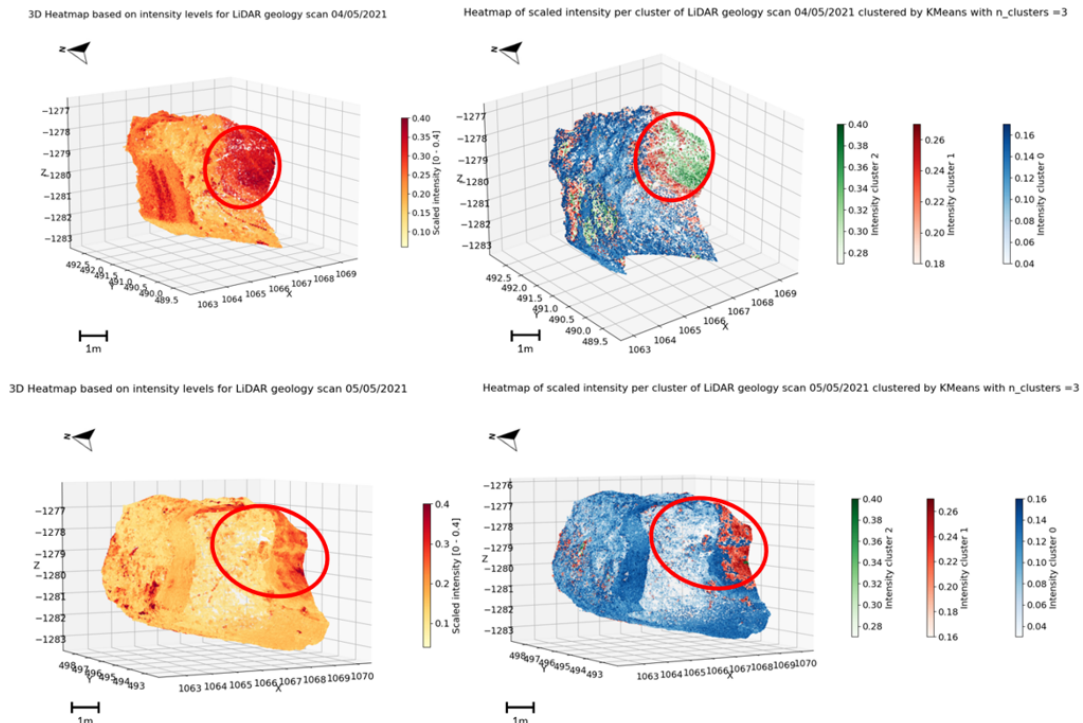


Figure 6.85: Geological LiDAR data of exposed rock surfaces on 04/05/2021 and 05/05/2021.

Figure 6.85 shows similar results as was seen in both the RGB images as well as in Figure 6.84. The right wall of the room is a very heterogeneous mixture of different minerals, which can lead to stability issues. There is no strong uniform structure to withstand the forces that act on the rock, therefore the convergence is strongest in these regions.

It is also clear that when comparing the **RGB** images to the geological **LiDAR** intensity images, that the shotcrete has a relatively high intensity compared to the rocks present. This was taken into account when analyzing the data and not included in the stability analysis. However, even when excluding the shotcrete from the intensity analysis, it is possible that the hanging wall shows a mixture of different minerals based on the varying light intensity levels. The other geological scans are shown in **D**.

Additionally, the differences in light intensity and even the exclusion of data (the white gaps in the intensity visualizations) due to i.e. occlusion or discontinuities can also be signs that the uniform structure of the rock is interrupted by for example a joint or a vein.

7

DISCUSSION

There remain a lot of unexplored areas in the field of LiDAR scanning for underground applications. This study has only shown a small portion of the potential of this new technique. More detailed analyses of the data can be conducted to get an even more thorough understanding.

7.1 LIMITATIONS

An important limitation of the LiDAR deformation scans in an active mining environment is the fact that a zero reading of a specific part of the tunnel can only be obtained as soon as the exposed rock surface is blasted. It is difficult to make this data overlap with previously scanned areas. Another limitation found in this study and also by Cabrejo et al. [2017] is the repeatability of periodic measurements. Even with the use of target sheets to georeference the subsequent scans, it remains difficult to properly align the scans. The software that comes with the GML scanning technology has to be optimized in order to achieve the desired precision. From this study, it has become clear that this can prove to be an issue if the scanning position is off, because it can lead to negative deformation in one wall and positive deformation in the other. If this is not interpreted correctly, the analysis of the movement of the tunnel may be very wrong.

Furthermore, at certain transition zones, where the rock extent of the previous blast session meets the newly exposed rock of the next blast session, it is very difficult to determine if the movement is induced by the blast or if the LiDAR data shows movement because rock has been removed. This leads to a matter of uncertainty at these boundaries or transition zones.

As suggested in subsection 6.1, the results between periodic scans can vary greatly (a total margin of ± 3.8 mm was found) even in a controlled environment. This means that when repositioning the scanner and conducting subsequent scans, the precision error can build up over time. As suggested in subsection 5.5.1, it is possible to apply either a manual correction or an automatic alignment. The manual correction is however very subjective and prone to how experienced the user is (thus human error as well). The automatic alignment function is not fully developed and this can lead to wrong interpretations as well. It must however be taken into account that the accuracy measurement experiment in this research only consisted of a total of 10 scans per set-up. A more detailed analysis in a controlled environment is required to obtain a true understanding of the precision of the GML scanner.

The results sometimes imply the movement of rock mass in certain areas that have undergone mining activities such as addition of shotcrete or scaling of rock material. As of now, it is difficult to 'mask' those areas, even if the area where this occurred is known to the author. This makes it hard to distinguish actual rock movement from the mining activities mentioned earlier. To achieve this, the software should make it possible to exclude certain regions of the tunnel, if the responsible person is aware of scaling/shotcreting activities. It would then be possible to set the zero-reading of that particular part of the tunnel at the date after the scaling or shotcreting.

7.2 SIGNIFICANCE OF THE RESULTS

The results from this study show that the LiDAR technology has great potential for mining applications, but still has some limitations to overcome. The most important limitation to overcome is the repositioning error of the scanner when conducting periodic measurements. In a mining environment such as the Kristineberg mine, there is often not the option to conduct continuous measurements due to bending of the tunnels, heavy machinery that needs to pass or simply the blasting of the face. Once such limitations are handled, the LiDAR technology is likely replacing conventional measurement techniques in the future.

Benefits for the analysis of the deformation of the rock mass have also been illustrated, i.e. the rapid acquisition of detailed 3D data. The LiDAR data provides a more detailed insight in the overall rock mass movement than with conventional techniques. This allows for increased understanding of the tunnel wall convergence and lead to enhanced tunnel stability and worker safety.

7.3 GEOLOGICAL ANALYSIS

As described in this study, the **LiDAR** scanners are useful tools when analyzing fresh rock. The lithological characterization of the outcrop can be done based on varying intensity levels. The subjectivity of the initial geological analysis is removed by using the scan data. There is still some subjectivity when it comes to interpreting the intensity differences, but it is less apparent. This research suggests that the heterogeneous hanging wall is more prone to deform than the rest of the tunnel. It is however not immediately clear whether the hanging wall geological structure is causing the main instability, or the heterogeneity of the rock mass. Further analysis is required to determine this in more detail.

Additionally, the discontinuity mapping can be analyzed more extensively to be able to obtain an idea if the discontinuities have a significant impact on the deformation of the tunnel walls. A more elaborate look at the geological features can lead to more insight in the impact of the geological setting on the movement of the rock mass. This was now done by visual inspection which means that the discontinuity analysis was still too subjective. This analysis should be almost entirely objective in order to give a proper overview of the circumstances.

For the **RGB** images taken during this research, it was sometimes difficult to have access to adequate lighting in the underground tunnel environment. This limitation of light can have a negative influence on the result, i.e. when a concentrated light source such as a flashlight leads to high contrasts in light intensity on the rock. This leads to potentially wrong classifications of the different litho-types present. On top of that, the **SVM** algorithm used in this study is also relatively subjective to a certain extent. The use of only this one supervised algorithm can lead to biased results, for example if the geological department already made an initial analysis and this is (more or less) copied in the **RGB** image classification.

8.1 CONCLUSION

The main objective of this study was to analyze the tunnel stability in the Kristineberg underground mine through deformational data acquired by means of LiDAR equipment in order to provide a quantitative estimation of the movement of rock mass. Additionally, a cross-correlation has been performed between LiDAR deformational data and LiDAR data combined with RGB imaging in order to estimate the influence of geological features on tunnel stability issues. The results of this report show promising potential for the use of a combination of LiDAR and RGB to get much better insight in the influence of geological structures and lithologies with respect to deformation patterns. If the geology of the tunnel is adequately mapped and analyzed, it becomes much easier to analyze and predict potential failure and prevent hazardous situations from occurring. It is also possible to guide the tunnel reinforcements in a more structured manner in order to ensure tunnel stability. This eventually leads to enhanced mine safety and reduced costs in tunnel reinforcements.

8.1.1 Research Questions

Can a LiDAR scanner provide a reliable quantitative estimation of the movement of rock in an underground environment?

The precision of the GML is not always as precise as one would hope. From this research becomes clear that while the scanner has potential to be precise if used continuously, there are some limitations when it comes to periodic scanning. From the repositioning experiment in the controlled above-ground environment becomes clear that the positioning of subsequent scans of the GML can vary up to ± 3.8 mm. The main limitation observed in this report is the alignment of subsequent scans in the software, leading to repositioning errors in between scans which can cause significant errors.

Is the LiDAR scanner used in this research accurate enough to replace conventional tunnel convergence measurement techniques?

When comparing the GML to conventional measurement techniques, it becomes apparent that the conventional techniques may be more accurate, but also much more labour intensive if the whole tunnel has to be measured. The problem with the conventional measurement techniques is that they only provide data for very specific areas of the tunnel, while the LiDAR scanner has potential to visualize and analyze the entire 360 degrees area of the tunnel. A periodic measurement with the LiDAR scanner takes approximately 25 – 30 minutes including setting up the scanner and the target sheets. The biggest trade-off is therefore time-consumption: it is possible to get more accurate results by measuring every single area of interest by conventional techniques, but it takes a very long time. With the GML it is possible to obtain slightly less accurate results in at most 30 minutes. This then includes data of the entire tunnel area and it is also possible to geo-reference the data and visualize it in already existing mine visualization software. Once the software is optimized and able to properly align subsequent scans, the LiDAR scanner may even be able to achieve similar accuracy and precision as conventional measurement techniques.

Is it possible to distinguish different rock types and geological features from the LiDAR data and how does that correlate to RGB image analysis?

The varying light intensity that is reflected from the LiDAR beams and returned to the sensor allows for a distinction between different rock types. However, without any preliminary knowledge about the geological setting, it can prove to be difficult to chose the reflectivity ranges per cluster or rock type. Additionally it is helpful to know beforehand how many rock types might be present, because a number of clusters has to be chosen for the analysis. Geological features can be recognized from the LiDAR data. It is possible to recognize for example joints, but mainly as a result of joints being filled with a different rock type. It is more difficult to distinguish geological features from the MapTek software, because it requires manual selection of a subset of rock material. Therefore, it is also considered (partially) subjective and will not always provide similar results when conducted by different users. The rock type analysis of the geological LiDAR data has shown to result in similar rock type distinction when compared to the RGB image analysis. Visual inspection for example shows that the areas where the LiDAR data classification distinguishes shotcrete from minerals, the SVM algorithm used for RGB image analysis also classifies that

region as shotcrete. Therefore, geological LiDAR data analysis has the potential to replace RGB image analysis in areas where lighting is limited or hard to install. Additionally, the RGB image analysis combined with the LiDAR analysis provide the means for a more thorough understanding of the geological setting of the underground environment.

Is there a correlation between the features observed in the geological mapping data (from both RGB and LiDAR) and the deformational analysis from the LiDAR data?

The geological mapping data has shown that the waste rock seems to be more prone to deformation than other material. In the areas where a lot of waste rock was observed, a stronger deformation has also been observed. Additionally, the deformation is stronger in the case of a non-uniform structure, for example when a joint is observed in a tunnel wall that causes the structure to be split into two sections. The blast-induced deformation provides an example for this, where the hanging wall that pushes down on the tunnel has a non-uniform structure. A similar observation was obtained through the analysis of the continuous measurements. Therefore, it can be concluded that the features that cause non-uniform structures, for example joints, have a negative impact on overall tunnel stability because they lead to additional deformation.

8.2 RECOMMENDATIONS

A recommendation for future study would be to perform more accuracy measurements in a controlled environment, especially focusing on the repositioning error of the scanning technology. If this is studied in more detail, it can be understood properly and dealt with by means of further software development or by adequate training of the user of the equipment.

It is also recommended to more thoroughly study the settings of the scanner and experiment with different settings. The idea of this study was to overlap different scan locations of the same tunnel, which has turned out to be difficult due to blocking of part of the tunnel by machinery or waste rock. With the 'close' setting on the scanner, there is only limited data. It is recommended to conduct an experiment where several different settings are tested.

Furthermore, it is recommended to make sure that the majority of the experiments and analyses are conducted in a most objective manner. This limits the potential for human errors and also makes sure that the analysis can be conducted without the requirement of an extensive training.

Finally, the geological setting has to be studied in more detail. The Kristineberg mine has a very complex geological setting, which was shown to have a significant impact on the convergence of the tunnel. It is important to get a more thorough understanding of the factor that contributes the most to the tunnel wall deformation. A good study to investigate the influence of the non-uniform heterogeneous rock mass on tunnel wall convergence would be a zone where the hanging wall is almost vertical, such that it does not push down on the rest of the tunnel as much. The recommendation for this future study would be to look further than just using MapTek and the Python script used in this research, and to compare the results numerically.

BIBLIOGRAPHY

- Arebäck, H., Barrett, T., Abrahamsson, S., and Fagerström, P. (2005). The Palaeoproterozoic Kristineberg VMS deposit, Skellefte District, Northern Sweden, Part I: Geology. *Mineralium Deposita*, 40:351–367.
- Assali, P., Grussenmeyer, P., Villemin, T., Pollet, N., and Viguier, F. (2016). Solid images for geostructural mapping and key block modeling of rock discontinuities. *Computers and Geosciences*, 89:21–31.
- Bergström, U., Billström, K., and Sträng, T. (1999). Age of the Kristineberg pluton - western Skellefte District, Northern Sweden. *Sveriges Geologiska Undersökning*, 4:7–19.
- Boliden (2019). L-zone west mineral resource estimate. *Boliden documentation*, pages 1–83.
- Boliden (2020). Boliden summary report 2020: Resources and Reserves - Kristineberg. *Boliden documentation*, pages 1–36.
- Cabrejo, A., Campbell, L., Chen, B., and P., S. (30-10-2017). A novel geotechnical monitoring technology for underground tunnels to assess ground support effectiveness [paper presentation]. *16th Australian Tunneling Conference 2017, Brisbane, Australia*.
- Chen, J., Huang, H., Zhou, M., and Chaiyasarn, K. (2021). Towards semi-automatic discontinuity characterization in rock tunnel faces using 3d point clouds. *Engineering Geology*, 291:1–14.
- Chen, S., Walske, M., and Davies, I. (2018). Rapid mapping and analysing rock mass discontinuities with 3d terrestrial laser scanning in the underground excavation. *International Journal of Rock Mechanics and Mining Sciences*, 110:28–35.
- Clayman, C., Srinivasan, S., and Sangwan, S. R. (2020). K-means Clustering and principal components analysis of microarray data of L1000 landmark genes. *Procedia Computer Science*, 168:97–104.
- Contogianni, V., Kornarou, S., and Stiros, S. (2007). Monitoring with electronic total stations: Performance and accuracy of prismatic and non-prismatic reflectors. *Geotechnical News*, 25.
- Desta, F. and Buxton, M. (1-10-2018). Automation in sensing and raw material characterization - a conceptual framework [paper presentation]. *International Conference on Intelligent Robots and Systems (IROS), Madrid, Spain*.
- Fard, M., Thonet, T., and Gaussier, E. (2020). Deep k-means: Jointly clustering with k-means and learning representations. *Pattern Recognition Letters*, 138:185–192.
- Fekete, S. and Diederichs, M. (2013). Integration of three-dimensional laser scanning with discontinuum modelling for stability analysis of tunnels in blocky rockmasses. *International Journal of Rock Mechanics and Mining Sciences*, 57:11–23.
- Fekete, S., Diederichs, M., and Lato, M. (2010). Geotechnical and operational applications for 3-dimensional laser scanning in drill and blast tunnels. *Tunnelling and Underground Space Technology*, 25:614–628.
- Fisher, J., Shakoor, A., and Watts, C. (2014). Comparing discontinuity orientation data collected by terrestrial LiDAR and transit compass methods. *Engineering Geology*, 181:78–92.
- GeoSystems, L. (2021). *Leica Disto D2 specifications*. <https://shop.leica-geosystems.com/buy/disto/d2> [Accessed: 02/09/2021].
- Gigliero, J. (2010). LiDAR basics for natural resource mapping applications. *Geological Society London: Special Publications(2010)*, 345:103–115.
- Goodman, R. (1989). *Introduction to Rock Mechanics* (2nd ed.). Wiley.
- Grebbi, S., Cunningham, D., Naden, J., and Tansey, K. (2010). Lithological mapping of the Troodos ophiolite, Cyprus, using airborne LiDAR topographic data. *Remote Sensing of Environment*, 114:713–724.
- GroundProbe (2021a). *GML Convergence Monitoring*. <https://www.groundprobe.com/product/gml-convergence-monitoring/> [Accessed: 19/08/2021].
- GroundProbe (2021b). *GML User Manual*. 1.4:1–221.

- Höfle, B., Griesbaum, L., and Forbriger, M. (2013). Gis-based detection of gullies in terrestrial LiDAR data of the Cerro Llamoca Peatland (Peru). *Remote Sensing*, 5:5851–5870.
- Jansson, F., Hermansson, T., Persson, M., Berglund, A., Kruuna, A., Skyttä, P., Weihed, P., Gutzmer, J., Bachmann, K., and Chmielowski, R. (12-08-2013). Recent advances in structural geology, lithogeochemistry and exploration for VHMS deposits, Kristineberg area, Skellefte District, Sweden. *Mineral Deposit Research for a High-Tech World : Proceedings of the 12th Biennial SGA Meeting, 12–15 August 2013, Uppsala, Sweden*, pages 545–548.
- Kavvadas, M. (2003). Monitoring and modelling ground deformations during tunnelling. *Proceedings of the 11th FIG symposium on deformation measurements, Santorini, Greece*, pages 371–390.
- Lato, M. and Diederichs, M. (2014). Mapping shotcrete thickness using LiDAR and photogrammetry data: Correcting for over-calculation due to rockmass convergence. *Tunneling and Underground Space Technology*, 41:234–240.
- Lato, M., Diederichs, M., and Hutchinson, D. (2010). Bias correction for lidar scanning of rock outcrops for structural characterization. *Rock Mechanics and Rock Engineering*, 43:615–628.
- Mah, J., Samson, C., and McKinnon, S. (2011). 3D Laser imaging for joint orientation analysis. *International Journal of Rock Mechanics and Mining Sciences*, 48:932–941.
- Mueller, J. and Massaron, L. (2019). *Python for Data Science*. John Wiley & Sons Inc., Leyde.
- Pradhan, A. (2012). Support vector machine-a survey. *International Journal of Emerging Technology and Advanced Engineering*, 2:2250–2459.
- Rarity, F., Van Lanen, X., Hodgetts, D., Gawthorpe, R., Wilson, P., Fabuel-Perez, I., and Redfern, J. (2014). LiDAR-based digital outcrops for sedimentological analysis: workflows and techniques. *Geological Society London: Special Publications(2014)*, 387:153–183.
- Riquelme, A., Abellán, A., Tomas, R., and Jaboyedoff, M. (2014). A new approach for semi-automatic rock mass joints recognition from 3d point clouds. *Computers and Geosciences*, 68:38–52.
- Satici, O. and Topal, T. (2021). Assessment of damage zone thickness and wall convergence for tunnels excavated in strain-softening rock masses. *Tunneling and Underground Space Technology*, 108.
- Schwarz, G., Kathol, B., Ripa, M., Thunholm, B., Lynch, E., and Jönberger, J. (2020). Report on pilots: The Kristineberg and Nautanen mining areas in Northern Sweden. *CHPM2030*, pages 1–72.
- SoilInstruments (2021). *Digital tape extensometer*. http://www.itmsoilssupport.com/datasheets/E3_Digital_Tape.Extensometer.pdf [Accessed: 01/10/2021].
- Thiele, S., Lorenz, S., Kirsch, M., Acosta, I., Tusa, L., Herrmann, E., Möckel, R., and Gloaguen, R. (2021). Multi-scale, multi-sensor data integration for automated 3-d geological mapping. *Ore Geology Reviews*, 136.
- Turner, R., MacLaughlin, M., and Iverson, S. (2020). Identifying and mapping potentially adverse discontinuities in underground excavations using thermal and multispectral UAV imagery. *Engineering Geology*, 266.
- Vestal, B., Carlson, N., and Ghosh, D. (2021). Filtering spatial point patterns using kernel densities. *Spatial Statistics*, 41:128–152.
- Walton, G., Diederichs, M., and Delaloye, D. (2014). Development of an elliptical fitting algorithm to improve change detection capabilities with applications for deformation monitoring in circular tunnels and shafts. *Tunnelling and Underground Space Technology*, 43:336–349.
- Walton, G., Diederichs, M., Weinhardt, K., Delaloye, D., Lato, M., and Punkkinen, A. (2018). Change detection in drill and blast tunnels from point cloud data. *International Journal of Rock Mechanics and Mining Sciences*, 105:172–181.
- Weihed, P., Skyttä, P., Hermansson, T., and Whitehouse, M. (2011). New zircon data supporting models of short-lived igneous activity at 1.89 ga in the western Skellefte District, Central Fennoscandian Shield. *Solid Earth*, 2:205–217.
- Yi, C., Lu, D., Xie, Q., Liu, S., Li, H., Wei, M., and Wang, J. (2019). Hierarchical tunnel modeling from 3d raw LiDAR point cloud. *Computer-Aided Design*, 114:143–154.

APPENDIX



RAW LIDAR DEFORMATION RESULTS

Table A.1: Accuracy Measurement I: prisms results of the absolute deformation of the box vs. the Leica Disto D2.

Scan #	Deformation Leica DistoMeter [mm]	Deformation prisms [mm]	Delta deformation prisms [mm]
1	137.0	136.9	0.1
2	136.5	136.6	-0.1
3	136.0	135.7	0.3
4	137.0	137.0	0.0
5	136.0	136.2	-0.2
6	136.0	136.2	-0.2
7	136.5	136.7	-0.2
8	136.0	135.8	0.2
9	136.0	136.1	-0.1
10	136.0	136.1	-0.1

Table A.2: Accuracy Measurement I: prisms results of the absolute deformation of the box vs. the Leica Disto D2.

Scan #	Deformation Leica DistoMeter [mm]	Deformation reflectors [mm]	Delta deformation reflectors [mm]
1	137.0	133.6	3.4
2	136.5	133.4	3.1
3	136.0	132.5	3.5
4	137.0	134.9	2.1
5	136.0	132.7	3.3
6	136.0	135.9	0.1
7	136.5	136.5	0.0
8	136.0	136.4	-0.4
9	136.0	136.4	-0.4
10	136.0	134.5	1.5

Table A.3: KK2 Measurement Point 0 (MP0) deformation results.

KK2 - MP0	01/05/2021	04/05/2021	07/05/2021	11/05/2021	18/05/2021	21/05/2021	01/06/2021	04/06/2021	16/06/2021
Deformation right wall [mm]	-12.0	-14.3	-13.5	-13.2	-13.1	-10.7	-9.4	-16.8	-14.3
Deformation left wall [mm]	12.2	11.9	13.8	13.2	13.0	12.1	11.8	18.3	18.8
Total deformation wrt 01/05/2021 [mm]	-	-2.6	0.1	-0.1	-0.2	1.2	2.3	1.3	4.4

Table A.4: KK2 Measurement Point 1 (MP1) deformation results.

KK2 - MP1	01/05/2021	04/05/2021	07/05/2021	11/05/2021	18/05/2021	21/05/2021	01/06/2021	04/06/2021	16/06/2021
Deformation right wall [mm]	1.3	4.6	3.9	9.8	12.9	13.0	10.1	18.1	21.2
Deformation left wall [mm]	12.0	10.3	14.3	11.9	14.1	15.1	16.3	14.1	25.2
Total deformation wrt 01/05/2021 [mm]	-	1.5	4.9	8.4	13.7	14.7	13.1	18.9	33.1

Table A.5: KK2 Measurement Point 2 (MP2) deformation results.

KK2 - MP2	01/05/2021	04/05/2021	07/05/2021	11/05/2021	18/05/2021	21/05/2021
Deformation right wall [mm]	17.4	26.2	29.3	44.4	51.6	51.5
Deformation left wall [mm]	22.9	21.8	27.6	21.5	22.8	24.7
Total deformation wrt 01/05/2021 [mm]	-	7.8	16.6	25.7	34.2	35.9

B | KK2 LONG-TERM DEFORMATION

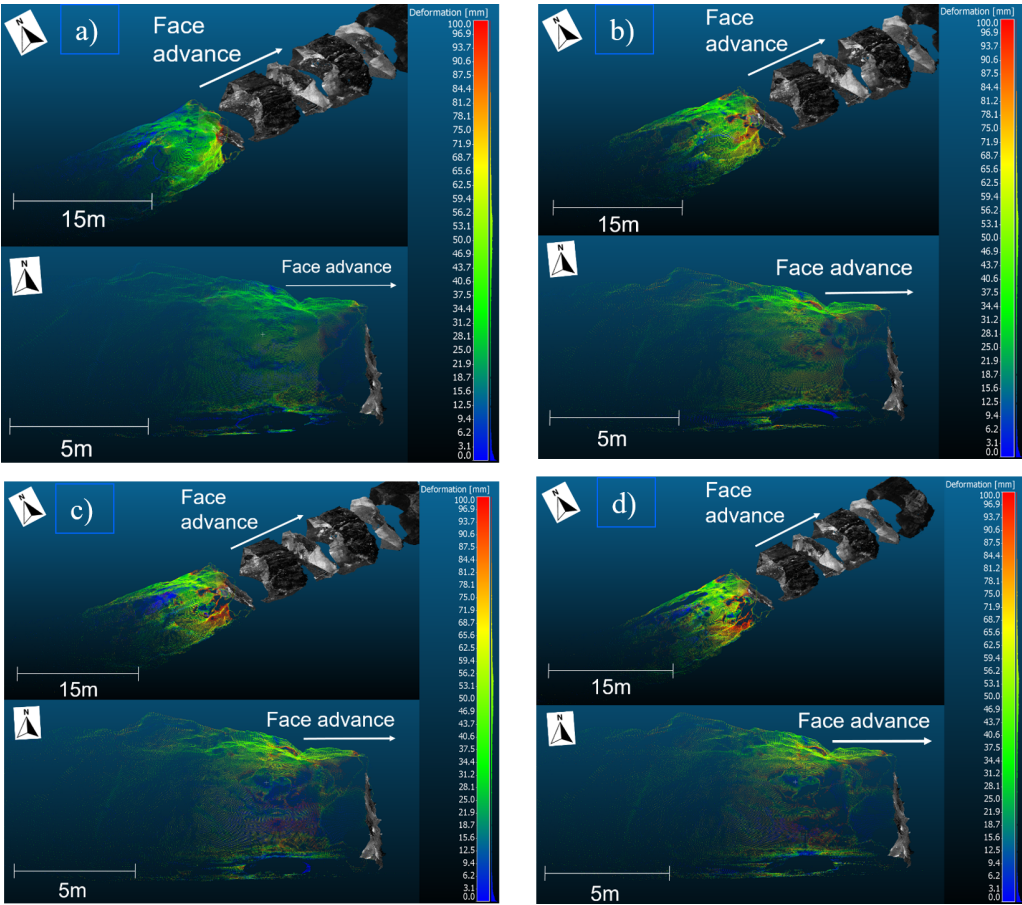


Figure B.1: KK2-1 long-term deformation from 23/04 until 18/05.

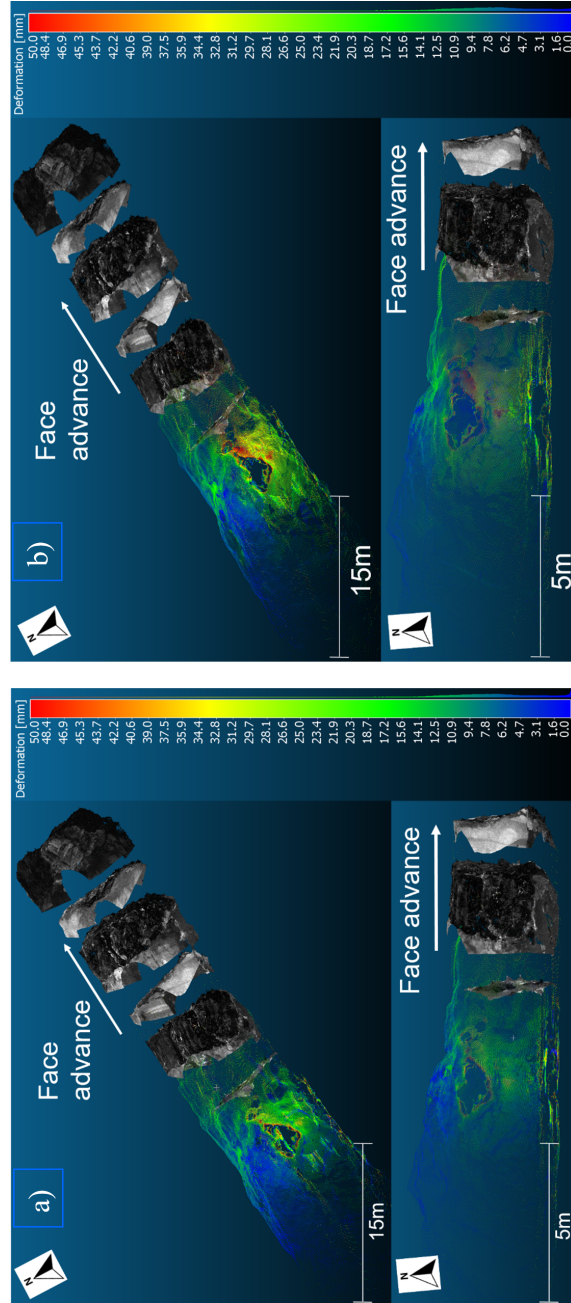


Figure B.2: KK2-1 long-term deformation from 04/05 until 18/05.

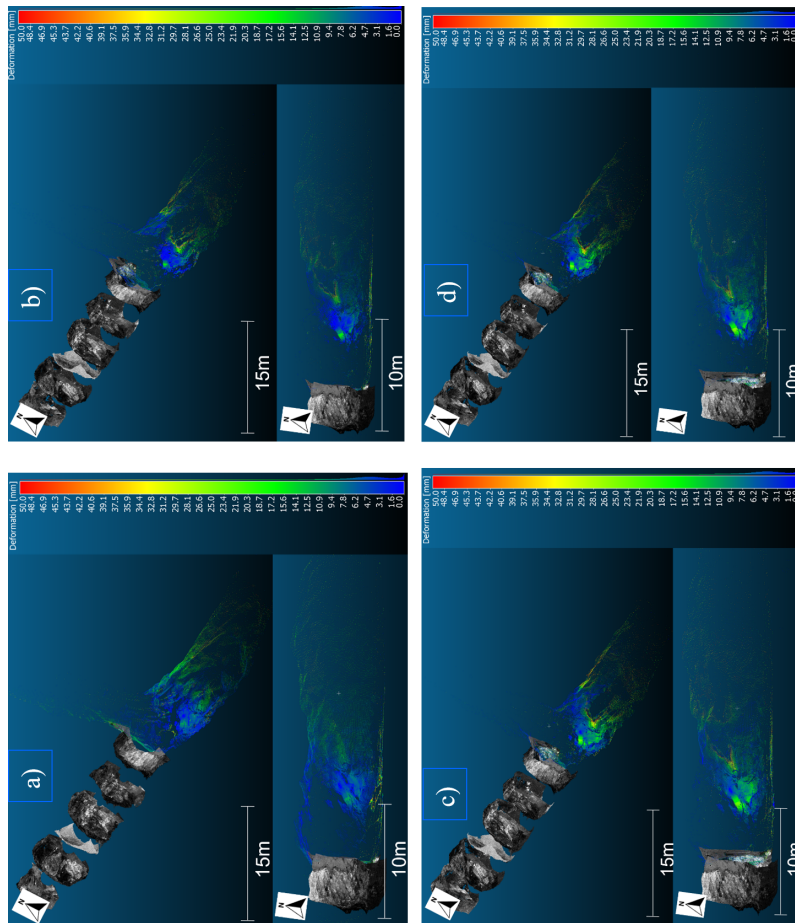


Figure B.3: KK2-2 long-term deformation from 22/04 until 11/05.

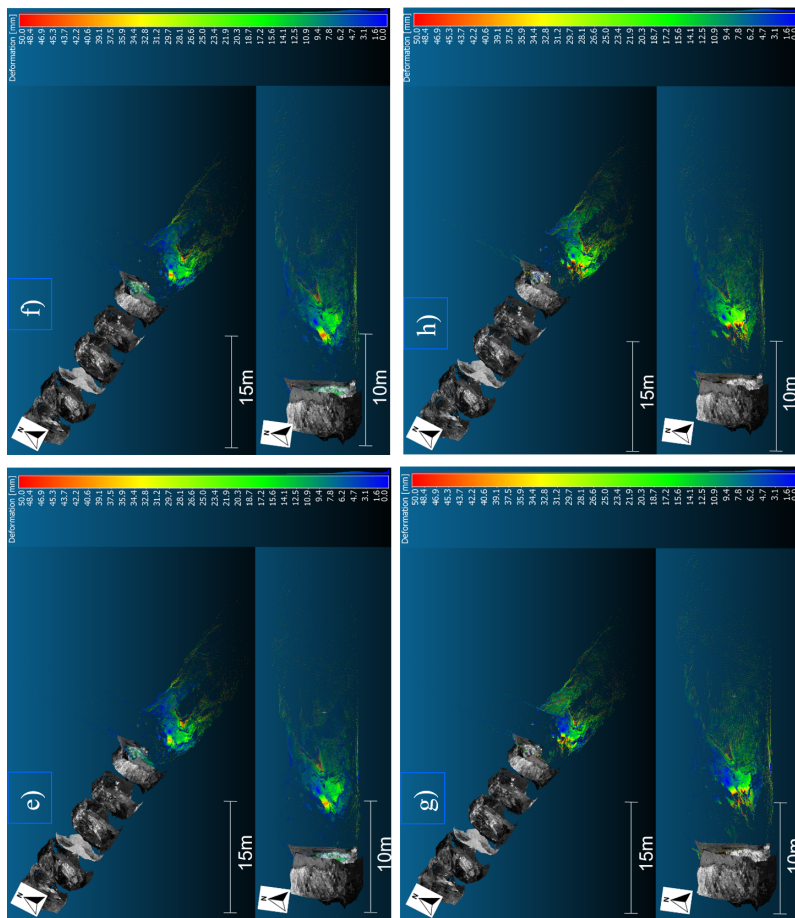


Figure B.4: KK2-2 long-term deformation from 22/04 until 05/06.

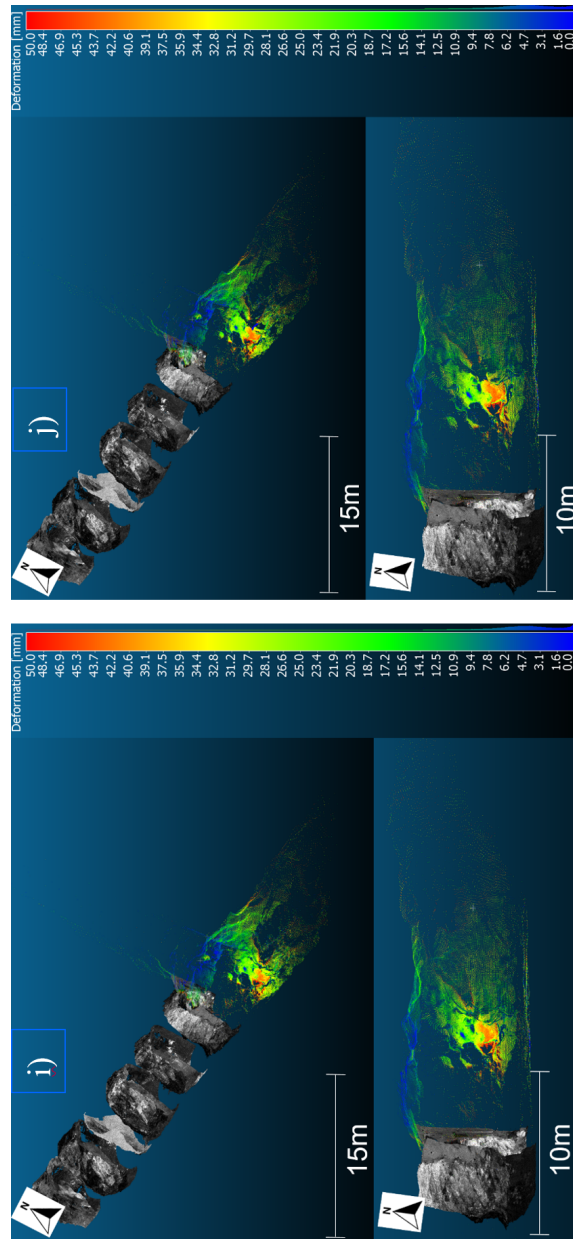


Figure B.5: KK2-2 long-term deformation from 22/04 until 18/06.

C | RGB GEOLOGY IMAGES CLASSIFIED

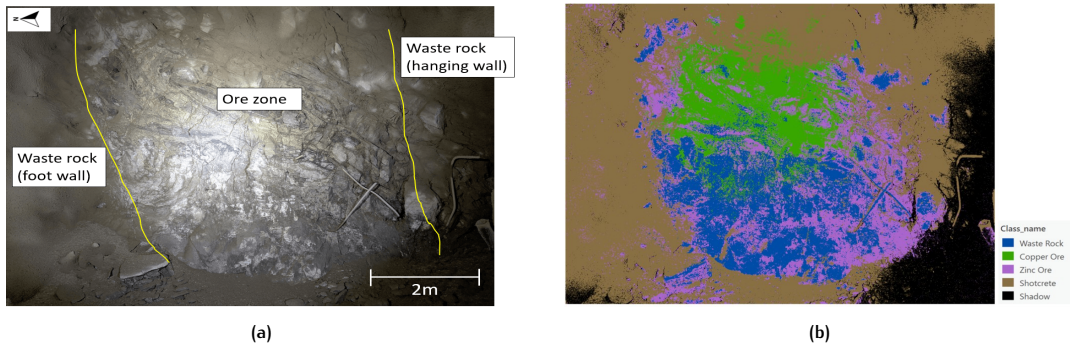


Figure C.1: Geological interpretation of the exposed rock surface on an RGB image of KK2 22/04/2021. (a) Structural geology of exposed rock surface. (b) Classified KK2 RGB image.

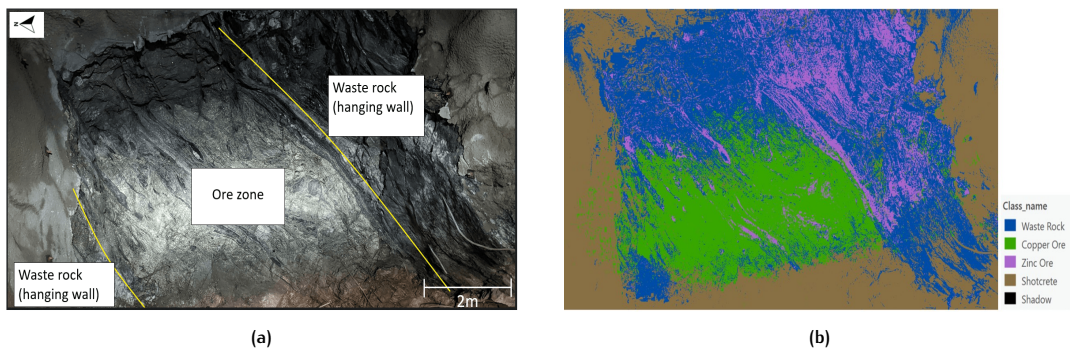


Figure C.2: Geological interpretation of the exposed rock surface on an RGB image of KK2 28/04/2021. (a) Structural geology of exposed rock surface. (b) Classified RGB image.

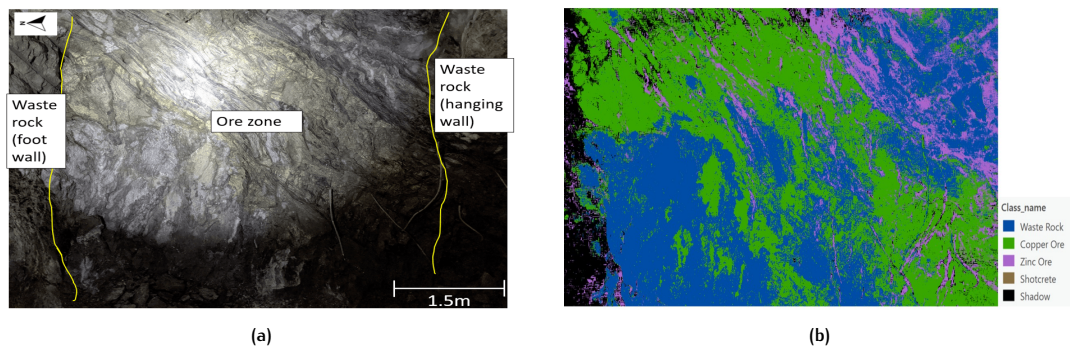


Figure C.3: Geological interpretation of the exposed rock surface on an RGB image of KK2 05/05/2021. (a) Structural geology of exposed rock surface. (b) Classified RGB image.

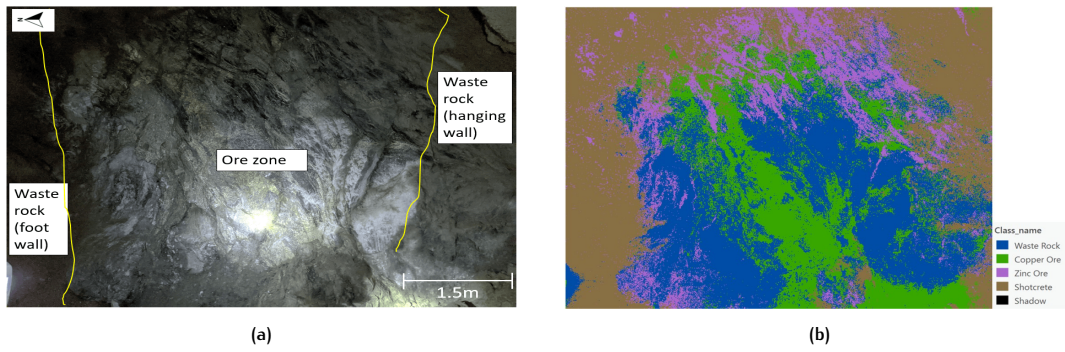


Figure C.4: Geological interpretation of the exposed rock surface on an RGB image of KK2 11/05/2021. (a) Structural geology of exposed rock surface. (b) Classified RGB image.

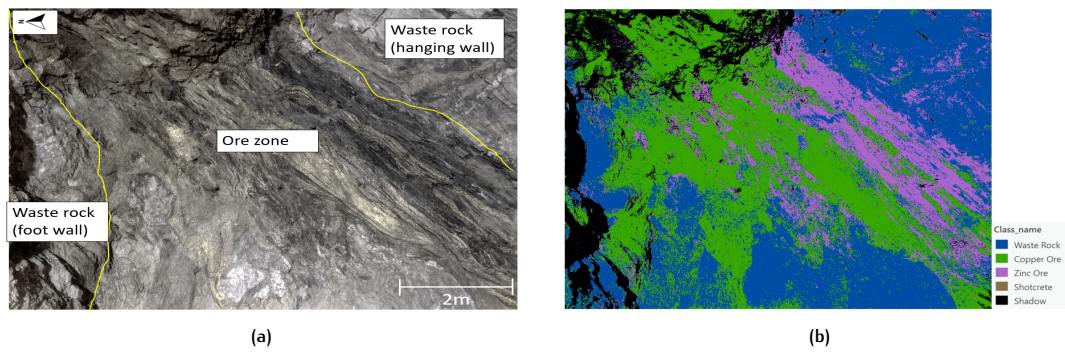


Figure C.5: Geological interpretation of the exposed rock surface on an RGB image of KK2 13/05/2021. (a) Structural geology of exposed rock surface. (b) Classified RGB image.

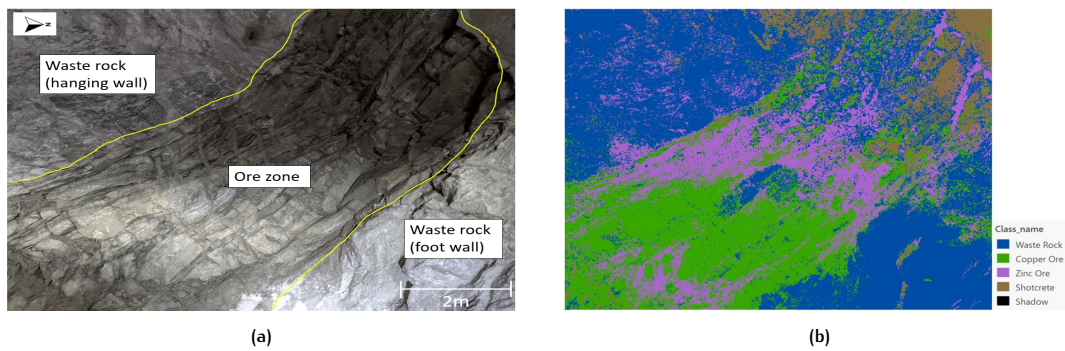


Figure C.6: Geological interpretation of the exposed rock surface on an RGB image of KK2 22/05/2021. (a) Structural geology of exposed rock surface. (b) Classified RGB image.

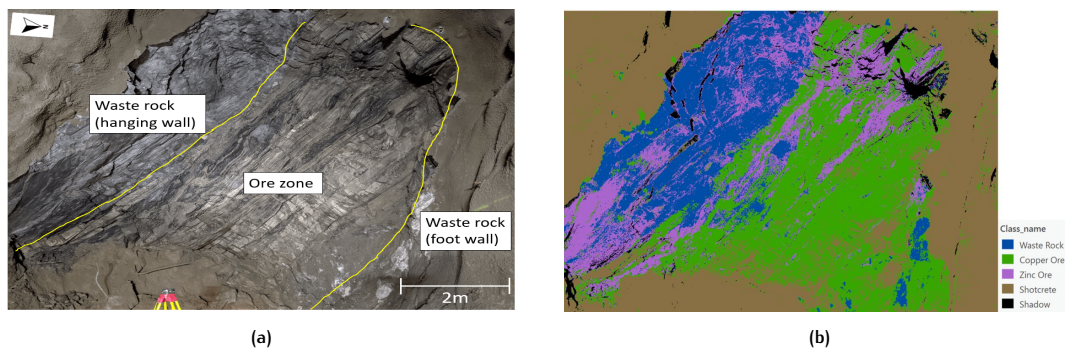


Figure C.7: Geological interpretation of the exposed rock surface on an RGB image of KK2 26/05/2021. (a) Structural geology of exposed rock surface. (b) Classified RGB image.

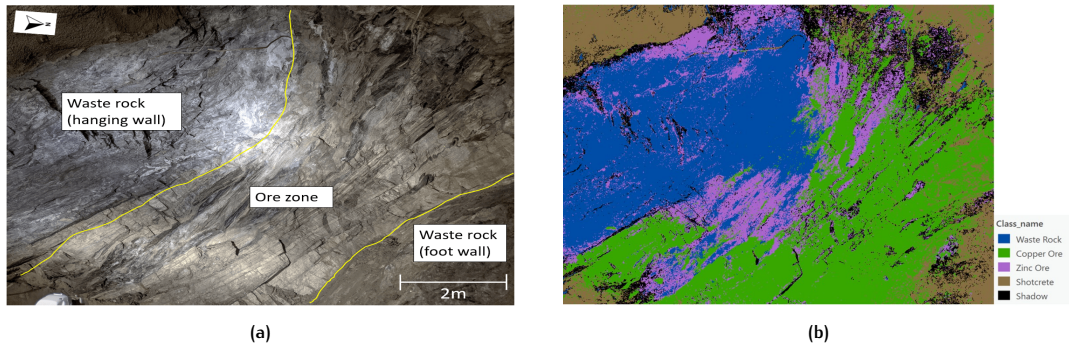


Figure C.8: Geological interpretation of the exposed rock surface on an RGB image of KK2 29/05/2021. (a) Structural geology of exposed rock surface. (b) Classified RGB image.

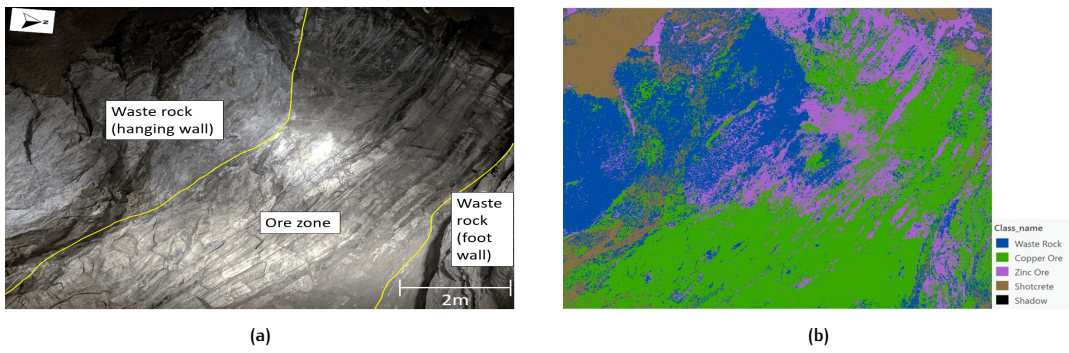


Figure C.9: Geological interpretation of the exposed rock surface on an RGB image of KK2 04/06/2021. (a) Structural geology of exposed rock surface. (b) Classified RGB image.

D

LIDAR GEOLOGY SCANS

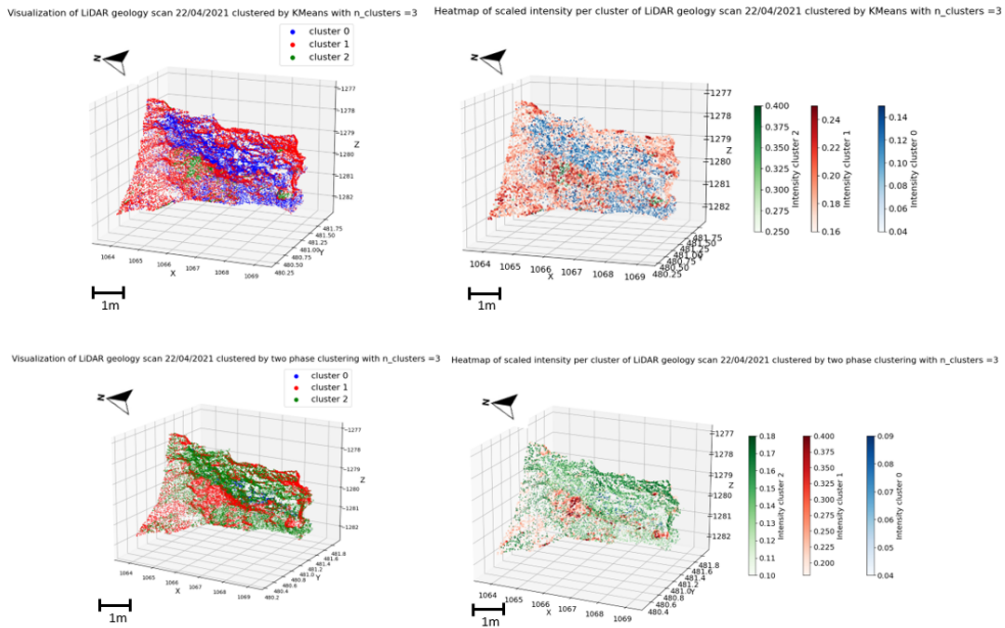


Figure D.1: LiDAR geology scan analysis 22/04/2021 [4/4].

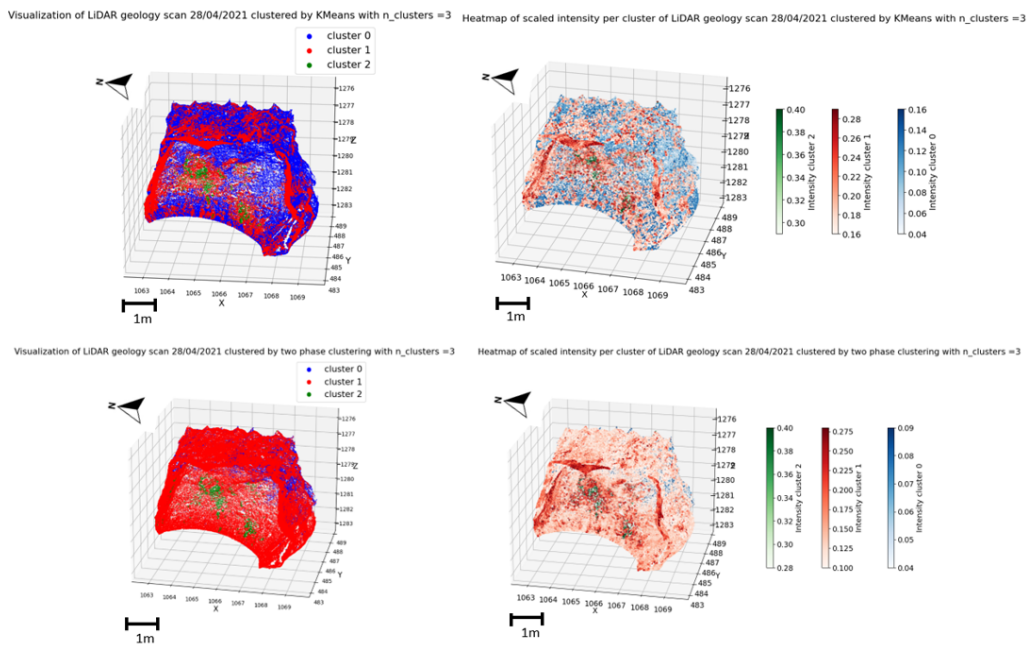


Figure D.2: LiDAR geology scan analysis 28/04/2021 [4/4].

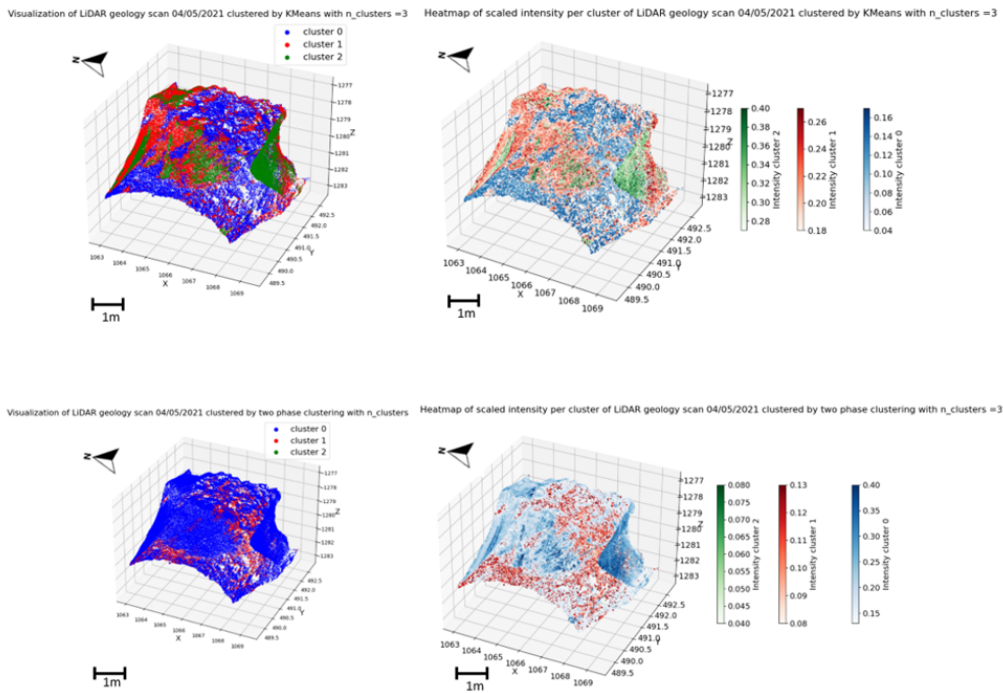


Figure D.3: LiDAR geology scan analysis 04/05/2021 [4/4].

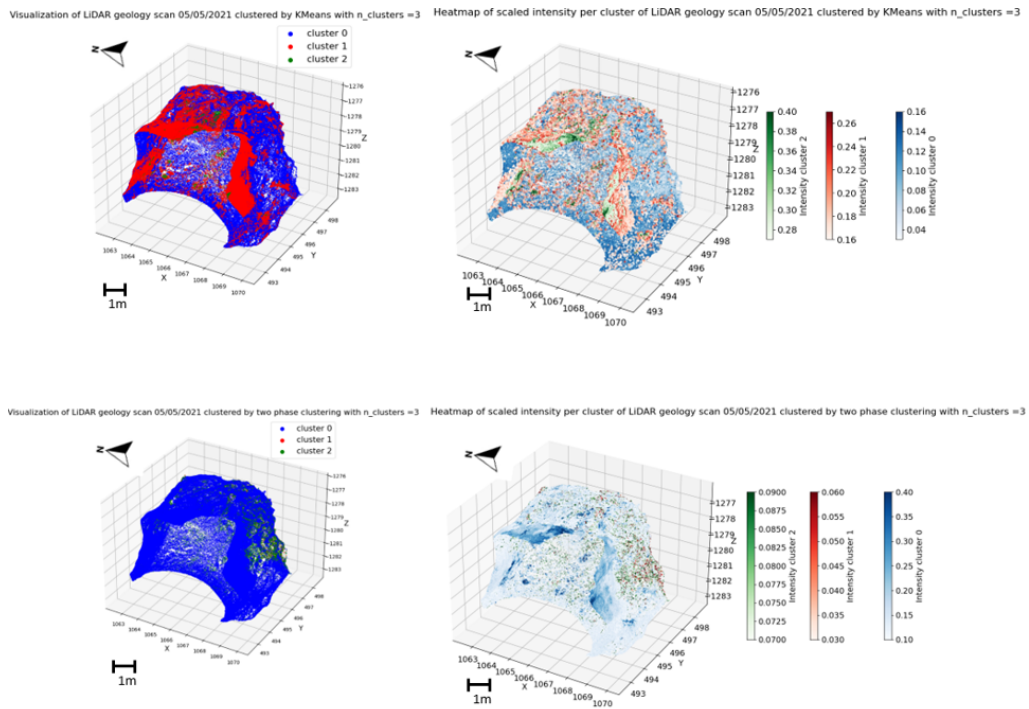


Figure D.4: LiDAR geology scan analysis 05/05/2021 [4/4].

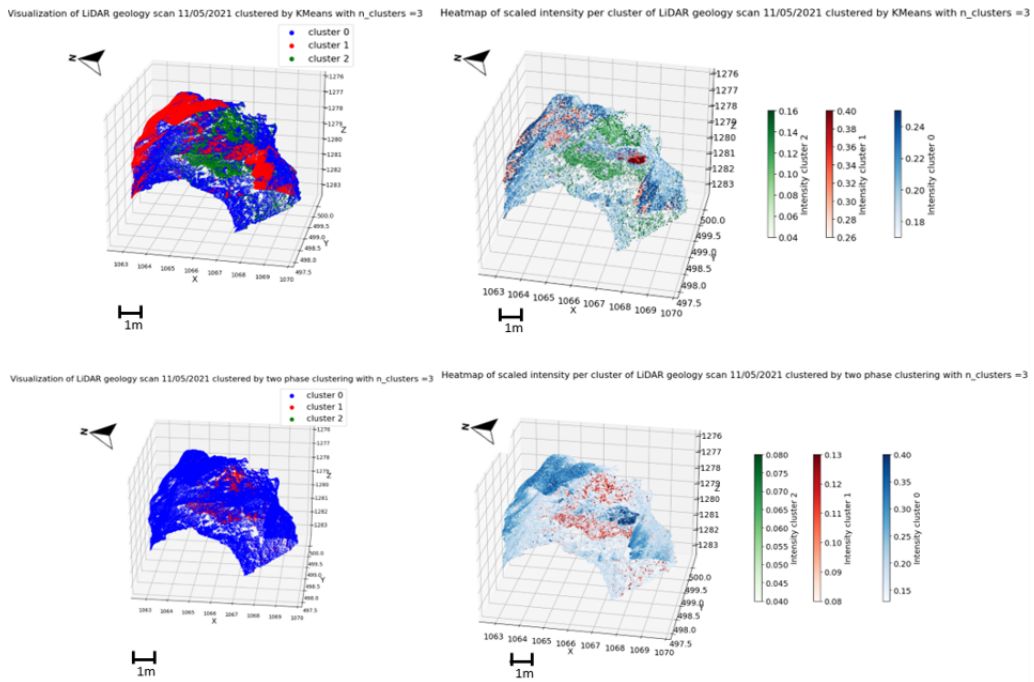


Figure D.5: LiDAR geology scan analysis 11/05/2021 [4/4].

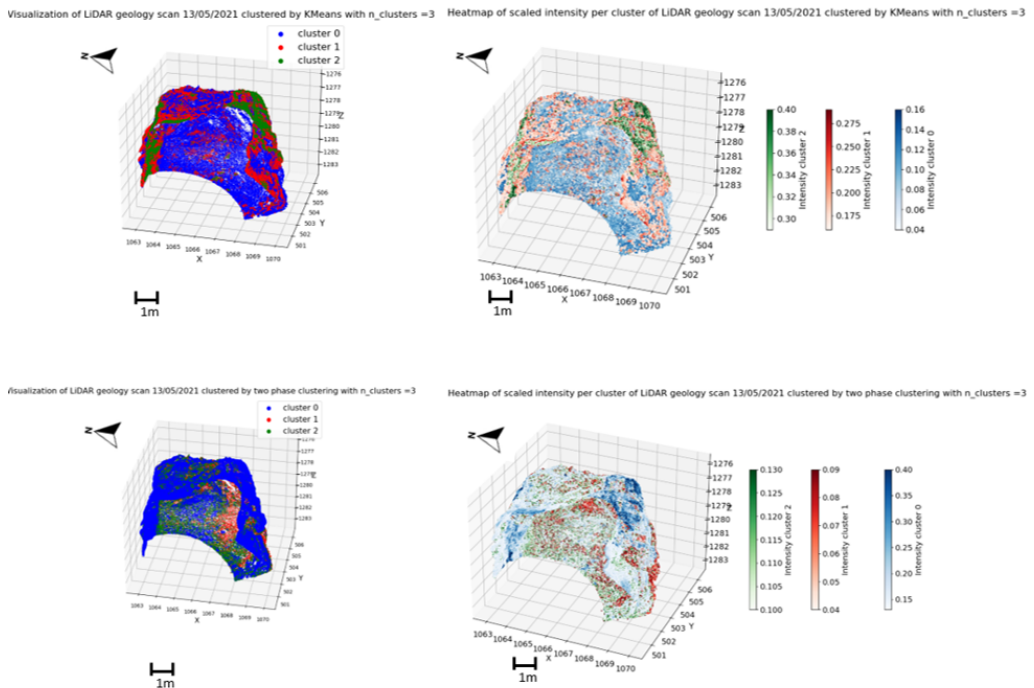


Figure D.6: LiDAR geology scan analysis 13/05/2021 [4/4].

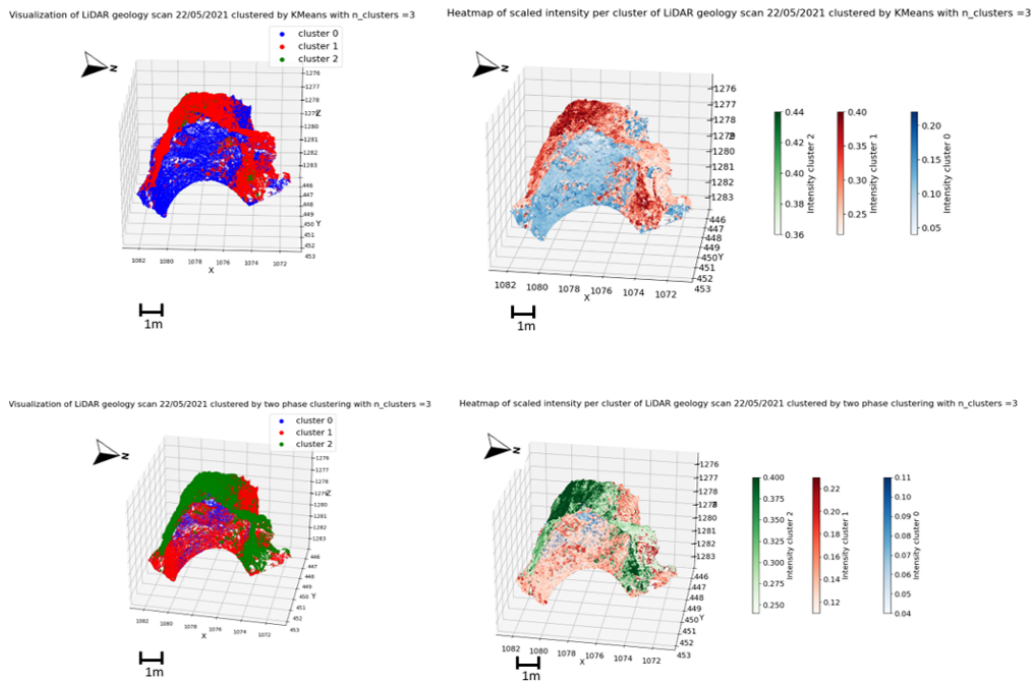


Figure D.7: LiDAR geology scan analysis 22/05/2021 [4/4].

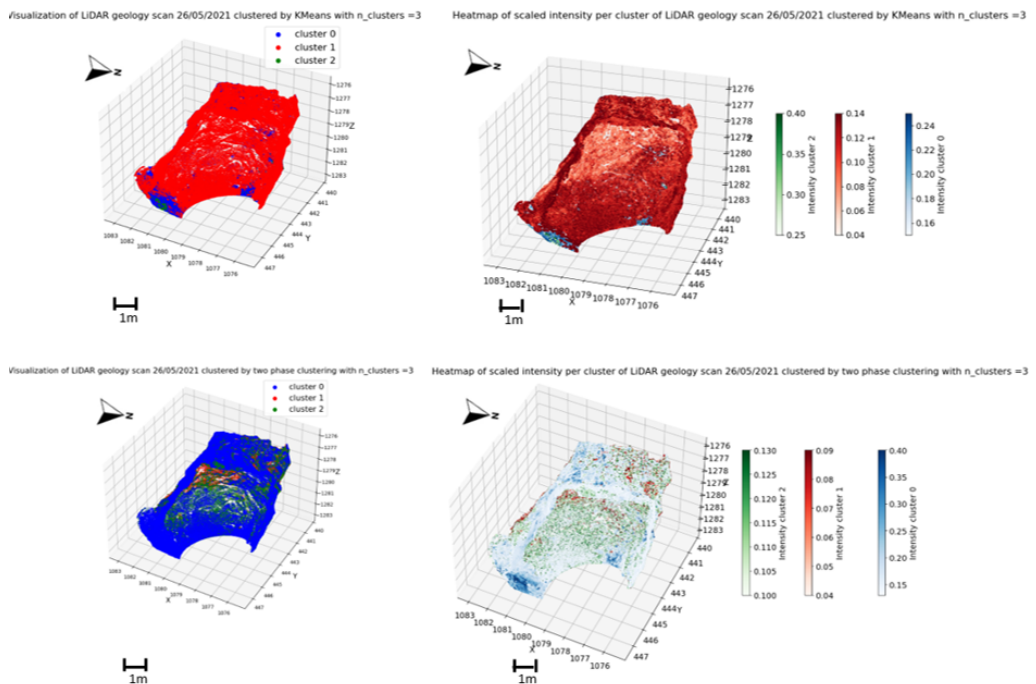


Figure D.8: LiDAR geology scan analysis 26/05/2021 [4/4].

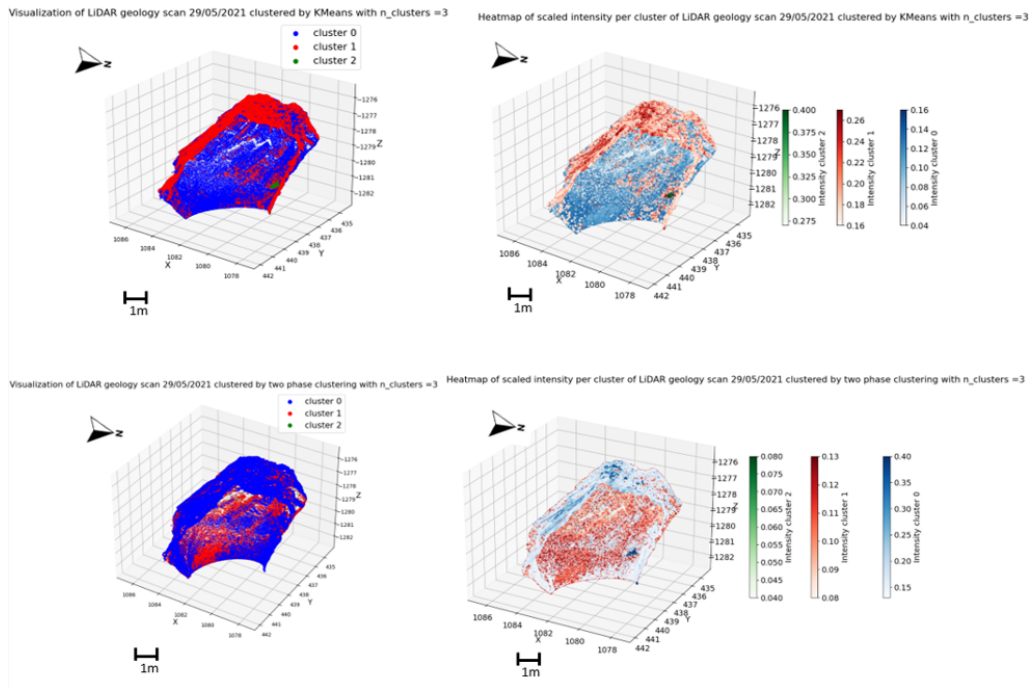


Figure D.9: LiDAR geology scan analysis 29/05/2021 [4/4].

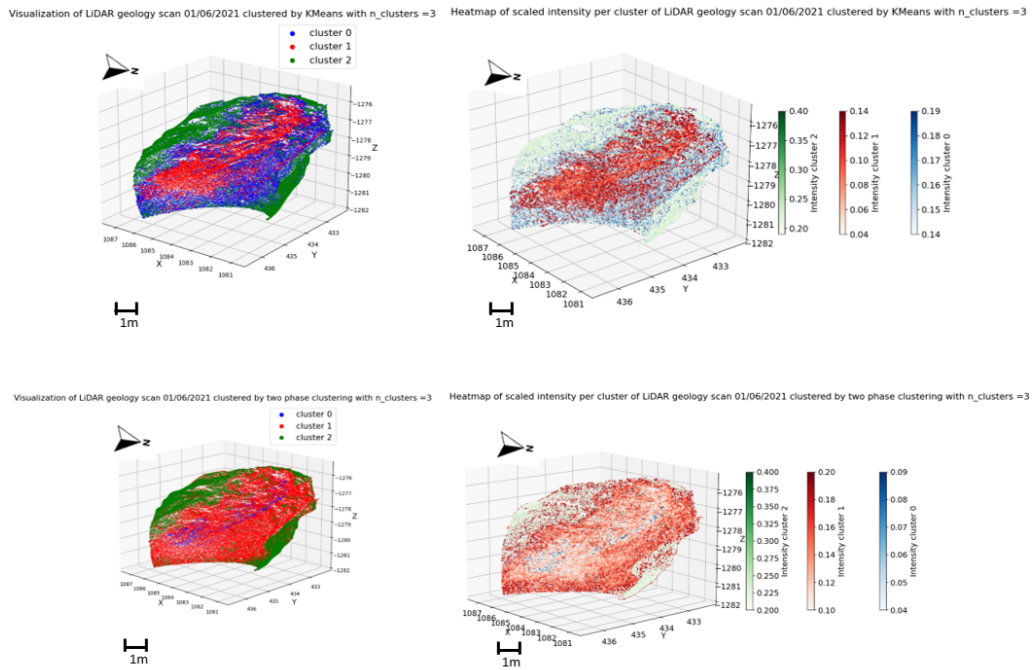


Figure D.10: LiDAR geology scan analysis 01/06/2021 [4/4].

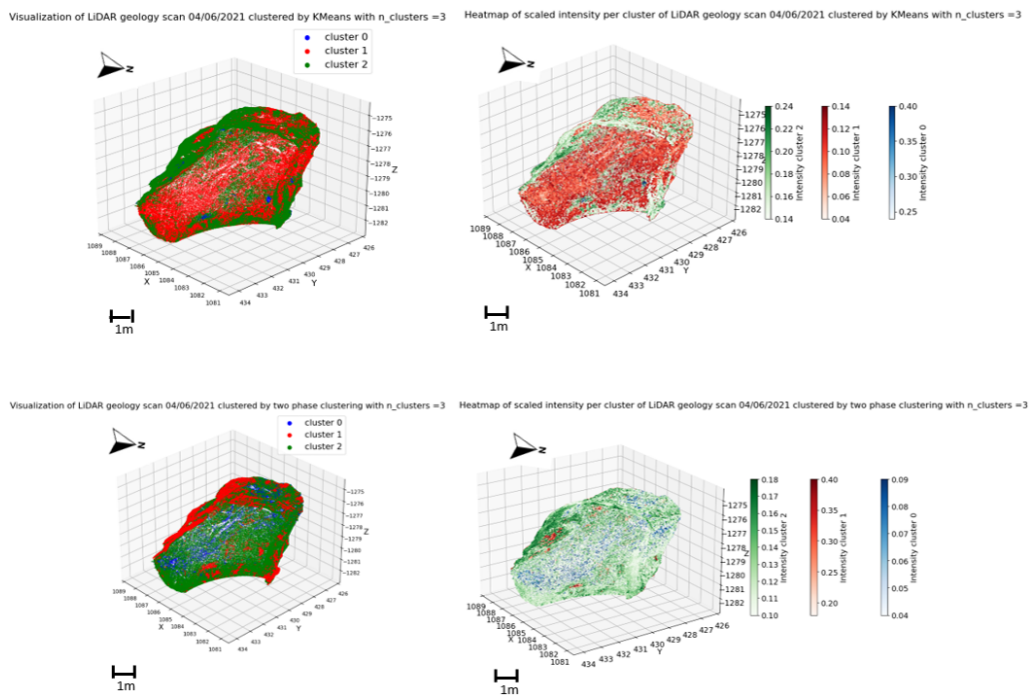


Figure D.11: LiDAR geology scan analysis 04/06/2021 [4/4].

COLOPHON

This document was typeset using \LaTeX . The document layout was generated using the `arsclassica` package by Lorenzo Pantieri, which is an adaption of the original `classicthesis` package from André Miede.

